Spring 2019

Modifying Inhibited Primer Performance via Control of Epoxy-Amine Matrix Structure and Composition

Steven Wand
University of Southern Mississippi

MODIFYING INHIBITED PRIMER PERFORMANCE VIA CONTROL OF EPOXY-AMINE MATRIX STRUCTURE AND COMPOSITION

by

Steven Michael Wand

A Dissertation
Submitted to the Graduate School,
the College of Arts and Sciences
and the School of Polymer Science and Engineering
at The University of Southern Mississippi
in Partial Fulfillment of the Requirements
for the Degree of Doctor of Philosophy

Approved by:

Dr. James W. Rawlins, Committee Chair
Dr. Sergei Nazarenko
Dr. Sarah Morgan
Dr. Gopinath Subramanian
Dr. Robson Storey

Dr. James Rawlins Committee Chair	Dr. Jeffrey Wiggins Director of School	Dr. Karen S. Coats Dean of the Graduate School

May 2019

Published by the Graduate School

ABSTRACT

This research represents an effort to deliver a new fundamental understanding of how polymer matrix characteristics influence corrosion protection of organic coatings, in particular the performance of corrosion inhibitor-containing primers. By modifying the structural and compositional features of an epoxy-amine matrix which commonly serves as the binder for protective coatings, the thermal/mechanical, adhesion, and transport properties which govern coating performance and inhibitor release were altered in such ways that directly influenced protection efficacy. The projects discussed herein detail three distinct approaches towards systematically varying the resulting thermoset network characteristics and observing the impact of those characteristics on transport behaviors and corrosion prevention, with an ultimate goal of understanding what optimal characteristics provide improved protection from chromate replacement inhibitor pigments (CRIs). In the first network series, free volume properties and water sorption values served as the primary polymeric characteristics monitored with respect to differing relative humidity environments and trends in moisture transport were observed and quantified. Experimental observations which indicated that the thermomechanical properties and oxygen permeation values shift following water sorption were related to polymer void size and varied between environmental severity conditions with clear distinctions relative to swelling processes. The second section of research was focused on a matrix series with incremental shifts in crosslink densities, dry glass transition temperatures, and hydrophilic monomer concentration while the degree to which these characteristics influenced water sorption and hydroplasticization were monitored and, in turn, modified the matrix swelling characteristics and corrosion protection efficiency with

either chromate or chromate-free corrosion inhibitors. The third and final research section revolved around a network series formulated to drive varying compositional features while maintaining a minimal variance in raw materials and a static structural motif. Moisture transport properties were related with corrosion protection while quantifying inhibitor depletion under accelerated corrosion tests using Raman microscopy to quantify these differences versus time. The findings of these varied approaches were combined and compared to produce a more comprehensive description of water and inhibitor transport in epoxy-amine matrices and to directly interrogate the performance criteria that increase CRI performance in organic protective coatings.

ACKNOWLEDGMENTS

There is no doubt that a large group of individuals contributed to my progress throughout this process and I am deeply indebted to each person who supported me during this experience. My graduate advisor and committee chair, Dr. James Rawlins, has for the last eight years been an employer, a mentor, an instructor, and an advisor to me in my various roles within the department and group. I consider myself lucky to have been continuously guided and challenged by him during that time to reach for something more than I at one time thought I was capable of achieving. My research committee members, Dr. Sergei Nazarenko, Dr. Robert Lochhead, Dr. Sarah Morgan, and Dr. Gopinath Subramanian all contributed to my development as a scientist, both in and outside the classroom, and for that I am very grateful. In the latter stages of this research a collaboration with Dr. Nazarenko and his graduate student, Ramesh Ramakrishnan, provided valuable teamwork and assistance in developing insight and understanding into not only the work we carried out together, but all of my research as a whole.

A number of talented and dedicated individuals within the Thames-Rawlins Research Group (TRRRG) have contributed not only to my progress as researcher but to my appreciation for polymer science and ability to think critically. Post-doctorate scientists Dr. Monoj Pramanik, Dr. Dwaine Braasch, Dr. Eric Williams, and Dr. Ethem Kaya have all assisted in both the collection and interpretation of data within this work and have always been willing to aid in developing an understanding for the research I have carried out. Additionally, David Delatte, Richard Ferguson, Michael Blanton, and Sharathkumar Mendon were likewise invaluable in making progress within the work

presented here and during my earlier stages within the group while working on various other projects.

I would also like to acknowledge a number of special graduate and undergraduate students that have helped me throughout my graduate career: Diana Gottschalk, who has always tried to include me in various activities around the department and made time to listen to me, Austin Maples, who has proven to be invaluable time and again in discussing and planning research and any other topic, and quite of few others: Bob Peterson, Mark Early, Christina Konecki, Greg Curtzwiler, Chris Scanlon, and Jessica Davison, all of whom served as appreciated brothers- and sisters-in-arms as fellow graduate students in TRRG. Additionally, many undergraduate research assistants aided in producing the work presented within this document, including Josh Breault, Gavin D'Ambrino, Delaney Clouse, and numerous others, all of whom are greatly appreciated.

I dedicate this work to my family who supported and encouraged my progress throughout the entire graduate process. In particular my parents, Mike and Kim Wand, are responsible for helping to keep me on track, motivating me when it was needed, and inspiring me to always reach for more. This work is inspired and made possible by your support and love – I will always be grateful for you and everything you've done.

TABLE OF CONTENTS

LIST OF TABLES

LIST OF ILLUSTRATIONS

CHAPTER I - INTRODUCTION

1.1 Overview

Chromate inhibitors have served as the dominate corrosion prevention approach in protective organic coatings for much of the last half-century despite the recognition of hexavalent chromium as a carcinogen and toxic pollutant.[1] A major issue resulting from the attempt to rapidly replace chromate chemistries with alternative chromate-replacement inhibitors (CRIs) in corrosion prevention of aluminum and steel substrates is the potential for performance or processing deficiencies which may occur upon substitution of any coatings system component, e.g. porous matrix development due to CRI-network interaction during cure. Replacement of hexavalent chromium-based inhibitors with CRIs has been successfully implemented to some extent in organic coatings, but there are no commercially viable alternatives that match the protection efficacy or duration of chromates. Part of the challenge lies in the poor understanding of how inhibitor pigments impart corrosion prevention and what the factors are that affect performance. It is believed that the availability of inhibitor ions at the substrate may be the determining factor in corrosion prevention performance outside of given electrochemical aspects: dissolution of the pigment particle followed by diffusion of ions to the substrate interface must occur for inhibition to take place.[2] If solubility is too high and diffusion of the inhibitor ions through the coating matrix occurs at exceedingly high rates, the ability to impede corrosion over long time spans will be lowered and blistering will likely occur. Alternatively, below a low solubility and diffusion threshold, adequate inhibitor ions are unlikely to reach the substrate. Other factors that influence the efficiency with which inhibitors prevent corrosion include presence of vapor/liquid phase

water, oxygen concentration within the coating, temperature or pH-dependency of specific inhibitor ions, and galvanic potential of the substrate. Of particular interest to this work is how polymer matrix properties affect inhibitor transport/efficiency and how network characteristics can be tailored to improve inhibition efficiency of chromate-replacement chemistries.

To understand how inhibitors can be better implemented as corrosion prevention technologies, the role of polymer matrices in inhibitor transport and delivery to the substrate will be investigated. This research is designed to study the polymer compositional and architectural features and gain understanding of the proper retention, release, and transport of alternative corrosion inhibitor technology in cross-linked coatings. A well-planned compositional series of epoxy-amine networks are anticipated to provide a systematic means of adjusting network parameters for practical but tunable differences in corrosion inhibitor diffusion rates, and delivery of solubilized ions for spatial and temporal inhibitor distribution. Specifically, the network composition and architecture will be adjusted by the amount and type of matrix building blocks, i.e., epoxy pre-polymers, chain extenders, and distinct cross-linker building blocks, to achieve distinct levels of cross-link density, glass transition temperatures (T_gs, with regard to rubber, glass, and leather physical states), and solubility parameters. The resulting high to mildly heterogeneous networks are expected to display a wide range of water affinity and transmission behaviors. For the thorough investigation of the role of matrix-inhibitor interaction and transport properties in corrosion prevention, three objectives are targeted: (1) investigate the ability to tune bulk water permeation behaviors of epoxy-amine matrices by varying network characteristics, (2) understand how local water transport

behavior in combination with network properties affects inhibitor transport through epoxy-amine networks, and (3) develop an inhibitor network balance which yields improved corrosion resistance for a given chromate-replacement corrosion inhibitor system.

These objectives stem from three hypotheses: (1) water permeation rates and saturation levels in epoxy-amine networks can be adjusted by modifying T_g, network architecture and composition, (2) inhibitor release and diffusion rates through a coating to the substrate can be manipulated through tuning of network characteristics (inhibitor-matrix interaction, T_g, cross-link density, and (3) improvement in CRI performance can be achieved by altering network properties to allow transport of active species to the substrate under timelines ideal for the inhibition process.

1.2 Background

1.2.1 Use of Chromates and CRIs in Primers

For decades, hexavalent chromium has provided one of the most effective means of preventing the corrosion of metal substrates via dispersion of chromate pigments (e.g., zinc chromate, strontium chromate, lead chromate) in organic coatings.[3] The mixed anodic/cathodic protection provided by these chromates is very effective in reducing the corrosion activity of metal surfaces, and is still widely used in commercial applications. However, the carcinogenicity and toxicity of hexavalent chromium necessitates that it be replaced with less harmful inhibitors and pigments.[2,3] Alternative pigments and methodologies that have been investigated include both organic and inorganic compounds and may provide anodic passivation, deposit insoluble salts at cathodic areas, or act as ion-exchange reservoirs.[2,4-6] However, none of these possess the efficiency of

chromates over an array of environmental conditions or for extended periods of time, hence the continued use of hexavalent chromium-based inhibition in critical applications such as the aerospace industry and military.[6] To develop a sufficient replacement for toxic chromates for inhibited primers, the mechanisms of inhibitor leaching and transport must be understood in addition to the electrochemical activity responsible for corrosion inhibition. Sinko posited that any inhibitor pigment incorporated into organic coatings requires in situ solubilization, dissociation, and hydrolysis to mobilize the inhibitive capacity of pigments, but that it is ion transport via diffusion through the polymer that facilitates the protective mechanism.[2] Organic coatings require that the inhibitor possess a number of physical properties (in addition to electrochemical activity) to function successfully as a corrosion inhibitor pigment: very low solubility in the polymer medium with relatively higher solubility in water (but less than 2 g/100 mL), low vapor pressure, and high melting point.[2] Chromates provide an ideal solubility range for use as inhibitors in organic coatings such that at least the minimum concentration of ions are released (> 10^{-4} mol/L) and diffuse readily to the substrate.[7]

A number of researchers have attempted to elucidate the mechanism of chromate inhibitor transport. Sellaiyan and co-workers utilized positron annihilation lifetime spectroscopy (PALS), radiotracers, and scanning electron microscopy (SEM) to observe chromate release and transport in a strontium chromate-inhibited epoxy-amine coating immersed in a 5 wt% sodium chloride solution. It was suggested that although some inhibitor diffused into the matrix regions surrounding the dispersed particles, a majority of the ion transport took place via a combination of small voids separated by very short distances and by micro-channels left behind by dissolved $SrCrO_4$ particles.[8] Similarly,

Scholes et al. proposed that swelling in epoxy-polyamide primers containing strontium and barium chromate upon immersion in 5 wt% NaCl solution developed a network of pores and channels as evidenced by PALS and Raman spectroscopy mapping. Although the differences in network properties, chromate transport, and swelling behaviors of the two coatings were not investigated, the authors opined that this porous network development was critical to inhibitor release in both films.[9] Prosek and Thierry proposed that diffusion of solubilized chromate through the polymer was central to corrosion inhibition during early stages of corrosion but dissolution of the particle was likely to be the rate-limiting step in long-term chromate leaching.[10] Several works noted pH-dependency of chromate leaching in organic coatings: the lower the pH of the solution in which the primer was immersed, the greater was the inhibitor release and transport rates. However, in highly acidic environments and at extended immersion times, this may be due to the development of porous networks following localized matrix degradation.[9,11-13]

Some strides have been made in the utilization of CRIs in organic coatings. Frankel and co-workers investigated a number of CRIs including molybdates, silicates, praseodymium salts, and an array of cationic species.[14] Through a range of electrochemical analyses and polymer morphology studies, the availability of the inhibitor at the substrate interface and the resulting corrosion performance was studied. It was determined that the water and inhibitor transport properties were influenced by the fine structure of the polymer matrix and variability of porosity in the different coating interfacial regions (Figure 1.1) as observed via PALS and Doppler Broadening of Energy Spectra (DBES) methods, although the extent to which these characteristics affect transport was not examined. In the films that did not exhibit satisfactory corrosion

prevention, it was suggested that inhibitor transport to the substrate was sub-optimal, and that the tractability of the transport network within the polymer matrix may allow for engineering of controlled transport properties.[14]

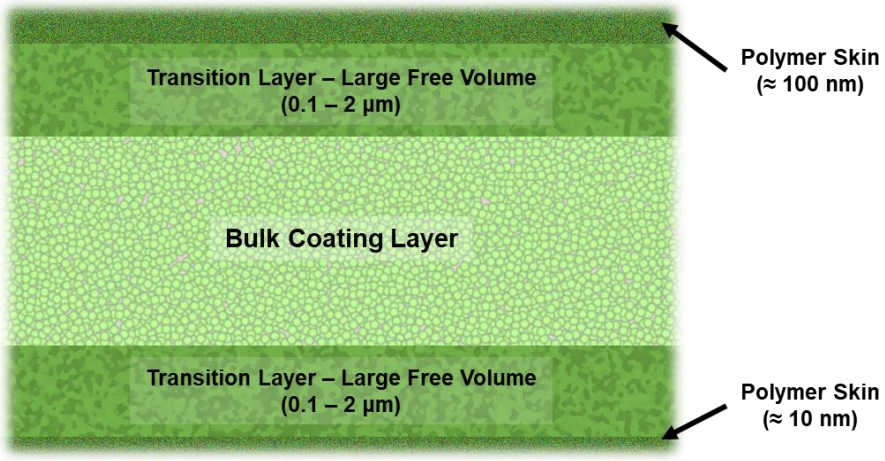

Figure 1.1 Cross-sectional depiction of free volume domains within an epoxy-amine primer following cure.

Demonstration of free volume void domains within a coating detected using positron beam analysis as described by Frankel and co-workers.[14]

Markley and co-workers investigated cerium diphenylphosphate, $Ce(dpp)_3$, in epoxy coatings applied to aluminum substrates and observed that although the rare earth metal complex impeded filiform corrosion growth, network formation was interrupted by the cerium allowing for a porous network to form. This porosity influenced a higher rate of water uptake and lead to an increased amount of solubilized cerium in the leachant, but the resulting impact on overall coating integrity was not reported.[15] Similarly, van Soesterbergen and co-workers dispersed $Ce(dpp)_3$ in an epoxy primer, and reported that inhibitor leaching rates reached high levels only at high pigment loading levels. In low pH ranges, the development of a highly porous network compromised coating barrier

efficiency.[16] Although these and other studies were conducted to understand how inhibitor transport takes place, no attempts were made to manipulate the polymer network to improve inhibitor delivery while maintaining the high coatings standards necessary for corrosion prevention (wet and dry adhesion along with suitable barrier properties).

1.2.2 Permeation, T_g, and Swelling in Polymer Coatings

Given the disparate reporting in the literature relating to moisture uptake and diffusion behaviors in thermoset polymers, a solid understanding of the commonly used terminology is necessary. Permeation is the transport of liquids or vapors through solids and is defined by three events: sorption (liquid/vapor uptake), diffusion (movement of one or more molecules across a concentration gradient), and desorption (liquid/vapor loss).[17] The permeability coefficient is characterized as the product of a solubility-related thermodynamic term and diffusivity kinetic term.[18] The polymer physical state has substantial influence over permeability – diffusion behaviors are known to vary substantially between glassy and rubbery states. Crank first purported that diffusion through rubbery polymers is expected to be Fickian while diffusion through glasses should follow non-Fickian behavior.[19] Fickian diffusion is typically specified as transport kinetics that can be described by Fick's law. A number of other diffusion behaviors have been noted in polymers: "two-stage," "sigmoidal," and "Case II" are among some of the specific types of non-Fickian transport forms (classified by their appearance in kinetic plots) that may occur due to varying degrees of interaction between the water and polymer or structural relaxation events (Figure 1.2).[17] It has been reported that increases in cross-linking generally have the effect of decreasing diffusivity in both rubbers[20] and glasses[21] although other polymer characteristics (polarity, polymer

backbone flexibility, etc.) have substantial influence over permeation behaviors as well.[20] External factors may influence water permeability in coatings, for instance, salt has been found to increase swelling by enhancing the solubility of water in polymers, and different additives (pigments, fillers, etc.) meant to influence coatings processing and performance will also impact moisture solubility.[22] Water acts as a plasticizer in polymer networks, lowering the T_g and increasing permeability up to a saturation point that is dependent upon both free volume and chemical composition.[23] In particular, thermoset chemistries may exhibit variable permeation/diffusion behavior depending on the experimental conditions (temperature, salinity, etc.) or network characteristics in addition to T_g.[24,25]

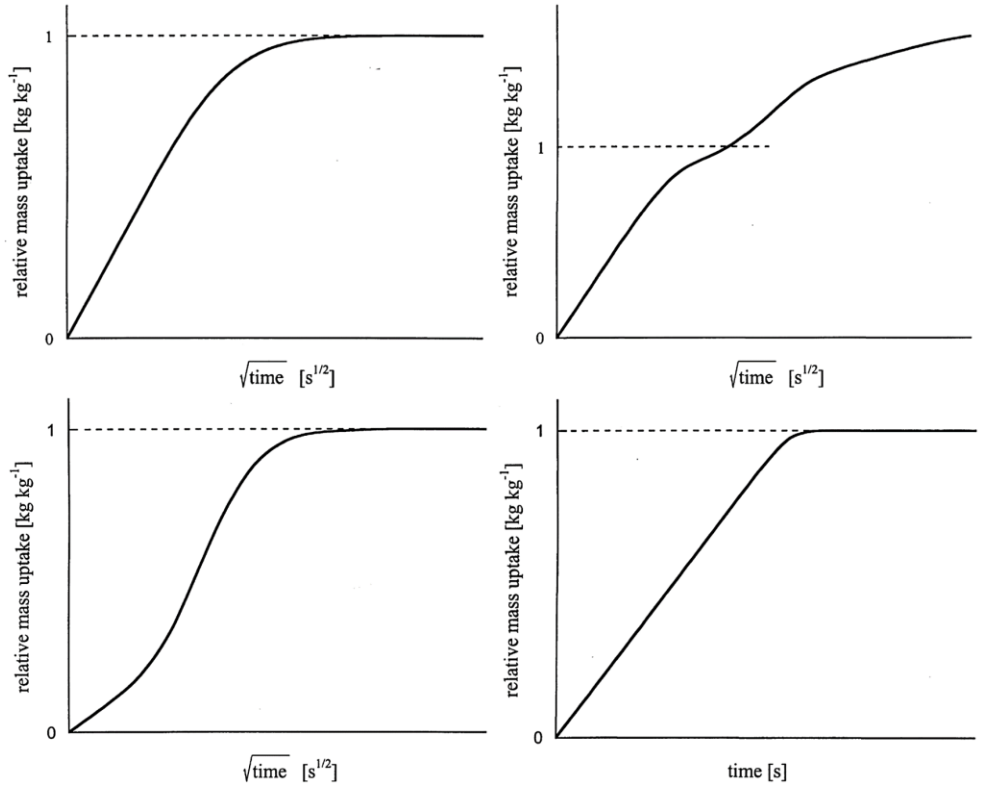

Figure 1.2 Example sorption kinetic plots exhibited by different diffusion cases.

Fickian, two-stage, Case II, and sigmoidal (clockwise from top left) sorption profiles noted in various organic coatings.[17]

1.2.3 Moisture Transport in Cross-linked Epoxy Networks

Epoxy-amine polymer networks are produced from the reaction of primary and secondary amines with epoxide rings and depending on the monomer molecular mass, stoichiometry, and functionality this can form matrices with a wide range of crosslink densities. The high concentration of secondary hydroxyls and tertiary amine functional groups that form upon polymerization, as shown in Figure 1.3, result in materials that are moderately hydrophilic due to the propensity for hydrogen bonding and polar interactions. As such, epoxy resin-based polymers exhibit an array of moisture diffusion kinetics and saturation levels (1-7 wt%) depending on experimental conditions and network properties.[19,22,24,29-32]

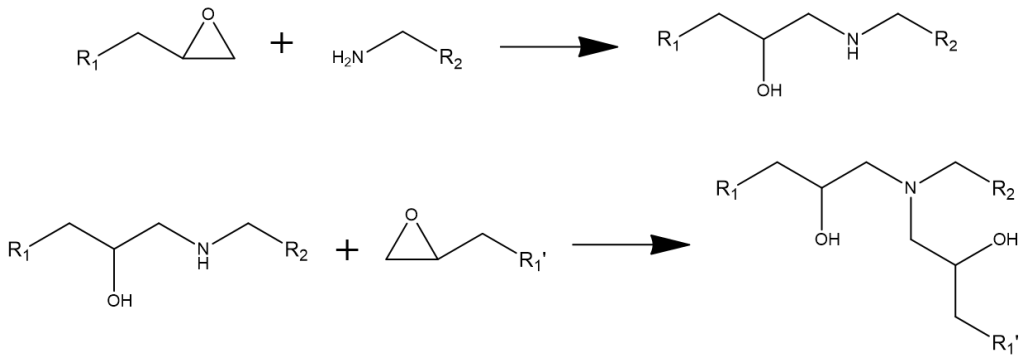

Figure 1.3 Demonstration of the epoxy-amine reaction leading to a crosslinked network containing secondary hydroxyl and tertiary amine functional groups.

Additionally, it has been suggested that different types of water populations may exist following permeation into a polymer depending on degree of molecular interaction.[33,34] Li and co-workers examined water diffusion mechanisms in diglycidyl ether of Bisphenol-A (DGEBA), triglycidyl *p*-amino phenol (TGAP), and tetraglycidyl ether of 4,4′ diaminodiphenyl methane (TDGGM)-based epoxy-amine networks using

attenuated total reflectance (ATR) – Fourier transform infrared reflectance (FTIR) and near infrared (NIR) spectroscopy with 2D correlation analysis, and determined that most diffusion into these networks is accomplished by water molecules in a loosely-bound doubly hydrogen-bonded state.[35] Often, a dual mode sorption is reported (in highly cross-linked epoxy systems below their T_g) wherein one population of water occupies free volume first, then additional water forms a hydrogen-bonded cluster within the network[29] with polymer-water interactions (polar and hydrogen-bonding) slowing the rate of diffusion.[31] However, some authors have witnessed Fickian-type diffusion of moisture and suggested that chemical adsorption of water onto polar interaction sites occurs first followed by permeation through free volume voids.[24,30] In addition to free volume and polarity characteristics, local chain rearrangement (segmental dynamics/swelling) and network architecture/cross-link density influence epoxy-amine water permeation properties.[32,35,36]

Phillipe and co-workers studied epoxy resin coatings at temperatures well below the T_g using ATR-FTIR and noted non-Fickian water diffusion behavior, which was attributed to a two-stage sorption process associated with different populations of hydrogen-bonding water distributions that progressed to single-stage Fickian behavior as the temperature increased to near the T_g. This is in agreement with the assumption that rubbery polymers exhibit Fickian diffusion while glassy polymers are thought to yield non-Fickian behaviors,[19] which is attributed to the higher mobility of water in cross-linked polymers in their rubbery form.[37] Soles and co-workers examined the water uptake behavior of a number of different epoxy-amine chemistries and found that matrix polarity, glassy dynamics, and free volume contributions acted in concert to control

diffusion properties with local scale motion related to the β-relaxation acting as the limiting factor in transport kinetics.[32,36] MacQueen and co-workers used PALS to examine changes in polyamide cross-linked DGEBA networks following immersion in water at 23 °C, and suggested that although a linear relationship between dry free volume fraction and water saturation level was found with 3-4% decrease in free volume cavity size, solvent interactions and swelling also have a significant impact on permeation behavior in epoxy films.[38] Patil and co-workers varied the chain length of polyetheramines used as cross-linkers in DGEBA-based networks and found that average free volume cavity size, as measured via PALS, increased with chain length and the water uptake behavior was influenced by the chemical composition, free volume characteristics, and segmental relaxations.[39] Van Landingham and co-workers witnessed Fickian diffusion in epoxy-amine networks only when they contained excess amine content (off-stoichiometric mixtures of components), suggesting that variability in diffusion activation energies resulted from regions of low or high phase density. While some deviation from Fickian behavior in epoxy samples has been attributed to temperature dependencies (affecting relaxation phenomena) or stoichiometric considerations (variation in phase domain diffusion),[25] others have indicated incomplete cure or oxidation upon water uptake may be responsible.[40]

1.2.4 Hydrogels and Network Heterogeneity

Another field of polymer research that may prove advantageous in understanding network properties in relation to inhibitor release and transport in polymer matrices is that of hydrogels as drug delivery vehicles. Much like inhibited primers, the use of hydrogels in drug delivery is often dependent upon sorption and diffusion of an aqueous

solution into a polymer network followed by release, transport, and desorption of small molecules contained within the gel. Hydrogels composed of cross-linked networks have been modified in a number of ways to provide distinct water permeation and drug transport behaviors.[41] A number of studies have yielded insight into the relationship between network properties and water uptake/small molecule release and transport in hydrogels. Wu and co-workers examined via molecular dynamics the effect of cross-linking density on water, ion, and small molecule diffusion in polyethylene glycol hydrogels by varying the M_c from 572 – 3,400 g/mol, and found that diffusion slowed with increasing cross-link density primarily due to heightened water hydrogen bonding dynamics with the greatest decrease in diffusion at the polymer-water interface.[42] Khandai and co-workers investigated the use of heterogeneous hydrogel networks as drug delivery vehicles for the highly water-soluble propranolol hydrochloride. Matrices consisting of equal weight fractions of hydrophilic hydroxypropyl methylcellulose and hydrophobic ethyl cellulose exhibited drug release profiles with heightened sustainability following swelling and erosion in phosphate buffer (pH 6.8) solution than matrices consisting of only one polymer type.[43] Hydrophilic polymer networks may also prove beneficial to organic coatings meant for corrosion resistance. Weber and co-workers found that hydrophilic polymer layers provided corrosion resistance as coatings for biodegradable metallic implants despite significantly high water content and ion permeability of the films following immersion in salt solutions due to the reduced chemical activity of water while bound to polyelectrolyte ion pairs.[44] It could be expected that increasing the content of hydrophilic groups within the polymer would also have the effect of increasing solubility of inhibitor pigments or drugs.

Heterogeneous network structure or development of separate hydrophobic/hydrophilic phases in mixed polymer networks may result in regions of variable solubility and influence complex diffusion behaviors. Kasargod and co-workers investigated dual-mode sorption solubility isotherms for glassy polymers, and determined that their heterogeneous nature resulted in inhomogeneous distribution of solute, identifying their diffusion type as pseudo-Fickian.[45] Zhang and co-workers enhanced the drug release profiles of poly(N-isopropylacrylamide) hydrogels through the introduction of heterogeneous network structure, which enabled the development of diffusion channels that expressed higher water release rates than a homogeneous network control.[46] Although epoxy-amine networks were once considered strictly homogeneous structures, some findings indicate that processing conditions or reactive component selection may result in inhomogeneity. Krakovsky and co-workers developed hydrophilic epoxy networks based on a α,ω-diamino terminated poly(oxypropylene)-b-poly(oxyethylene)-b-poly(oxypropylene) (Jeffamine® ED-600) cross-linking agents, and noted nanophase separated structures via small-angle neutron scattering (SANS). It was suggested the length scale of separation was controlled by network topology and cross-link density.[47]

1.2.5 Inhibitor-Matrix Interactions and Corrosion Performance

Following uptake and diffusion of water through a coating, inhibitor solubilized from inhibitor particles dispersed within the coating must traverse the polymer matrix to the substrate. In addition to water uptake and diffusion behavior, polymer-inhibitor interactions will influence the rate and mode of inhibitor transport through the coating to the substrate. To this effect, Tabor and co-workers sought to predict inhibitor release behavior by varying a number of theoretical matrix and inhibitor characteristics

(interaction between matrix and inhibitor, coating porosity, partition coefficients).[48] Modeling of the leaching-induced mass change (M_1) due to solubilization and diffusion of inhibitor as accomplished using the exponential equation:

$$M_1 \approx t^{\alpha}$$

to describe the amount of inhibitor released at time t where α is the release/transport exponent ($\alpha = 0.5$ represents Fickian diffusion, $0.5 < \alpha < 1$ represents anomalous diffusion, and $\alpha > 1$ represents pseudo-Fickian diffusion). By assuming constant small or large local release of inhibitor and varying the partition coefficients of the inhibitor and matrix, the model revealed values for α between 0.5 and 1.5, signifying that transport of inhibitor following dissolution and release could follow a wide range of different diffusion profiles simply by altering the matrix properties and matrix-inhibitor interactions. Yasakau and co-workers identified the potential for chemical interaction between inhibitor and a sol-gel matrix as a means of influencing the coating barrier integrity and corrosion efficiency.[49] It has been demonstrated that high intensities of interaction or bonding between coatings components and some chromate-replacement inhibitors may result in porous barriers (from network development disruption) or insufficient inhibitor release.[15,49] Transport of active species is highly dependent upon inhibitor solubility; very low water solubility will result in insufficient amounts of inhibitor reaching the substrate corrosion sites while excessive solubility will only provide protection for a short time and may result in blistering and delamination due to osmotic pressure build-up following rapid transport to the substrate.[50] A combination of highly soluble organic pigments and significantly less soluble inorganic pigments has been reported to improve the corrosion resistance of primers over variable time periods.[51]

Recently, a variety of "smart" or stimuli-responsive coatings technologies have been investigated to improve corrosion resistance of chromate-free inhibited primers.[52-54] Particle encapsulation and carrier loading methods for the purpose of triggered release of immobilized inhibitors have been suggested as approaches to improving efficiency; both the enhancement of inhibitor delivery efficiency following a localized trigger event, and the prevention of detrimental inhibitor-matrix interactions that might interfere with coating barrier integrity or inhibitor activity were sought in this approach.[50] Carriers composed of porous polymeric or inorganic media, hollow particles, and nanotubes loaded with inhibitors have been dispersed in primers for directed delivery following pH, ion-exchange, or mechanical rupture-related triggers.[54] A number of these studies have reported improved corrosion resistance in organic coating systems in comparison to freely dispersed CRI particles; however, chromate-level inhibition remains unattained in practical form. To our knowledge, no attempts have been made to systematically modify the polymer composition and matrix to understand how to control chromate-free corrosion inhibitor retention, delivery, and performance.

1.2.6 Rationale of Research

Considering the widespread need to sufficiently protect metal substrates from corrosion and the necessity for current chromate-replacement technologies to perform similarly or superior to the corrosion control efficiency of hexavalent chromium, a measure how the inhibitor free and inhibitor containing matrix affects the protection and environmental contamination and transport to the substrate is both desirable and necessary to understand the current and future process(es) of metal asset protection. Material properties in terms of mechanical, barrier and adhesion properties each impact

the performance aspects for corrosion control surface coatings. Combined with corrosion inhibitors the polymer properties are needed in different ways, e.g., water sorption and diffusion into and through the polymer coating is pivotal for inhibitor to be dissolved and electrically activated and ultimately delivered to the appropriate region of the substrate for passivation. The matrix characteristics, e.g., transport and permeability properties are clearly tethered to inhibitor release concentration and rates. Additionally, the ease with which the solubilized inhibitor traverses through the polymer directly influences the rate of corrosion inhibition efficiency, and matrix-inhibitor interactions may also influence transport rates. A number of studies have indicated that epoxy-amine networks exhibit a range of sorption and diffusion behaviors with solvents and small molecules stemming directly from a number of varying network characteristics.[32,36,55] This research was designed to systematically quantify the polymer matrix compositional and architectural properties direct control and indirect influence of inhibitor release and transport in corrosion-resistant coatings, and investigate the polymer/surface coating characteristics that are tunable to improve CRI performance.

1.3 References

1. CDC Health Hazards Evaluations. http://www.cdc.gov/niosh/topics/hexchrom/.
2. Sinko, J., Challenges of chromate inhibitor pigments replacement in organic coatings. *Prog. Org. Coat.* **2001,** *42*, 267-282.
3. Forsgren, A., Corrosion control through organic coatings. *Corrosion (Houston, TX, U. S.)* **2007,** *63*, 296.

4. Bethencourt, M.; Botana, F. J.; Calvino, J. J.; Marcos, M.; Rodriguez-Chacon, M. A., Lanthanide compounds as environmentally friendly corrosion inhibitors for aluminum alloys: a review. *Corros. Sci.* **1998,** *40*, 1803-1819.

5. Kalendova, A.; Vesely, D.; Stejskal, J., Organic coatings containing polyaniline and inorganic pigments as corrosion inhibitors. *Prog. Org. Coat.* **2008,** *62*, 105-116.

6. Twite, R. L.; Bierwagen, G. P., Review of alternatives to chromate for corrosion protection of aluminum aerospace alloys. *Prog. Org. Coat.* **1998,** *33*, 91-100.

7. Revie, R. W.; Uhlig, H. H.; Editors, *Corrosion and Corrosion Control: An Introduction to Corrosion Science and Engineering, 4th Ed*., John Wiley & Sons, Inc.: **2008**; p 490 pp.

8. Sellaiyan, S.; Hughes, A. E.; Smith, S. V.; Uedono, A.; Sullivan, J.; Buckman, S., Leaching properties of chromate-containing epoxy films using radiotracers, PALS and SEM. *Prog. Org. Coat.* **2014,** *77*, 257-267.

9. Scholes, F. H.; Furman, S. A.; Hughes, A. E.; Nikpour, T.; Wright, N.; Curtis, P. R.; Macrae, C. M.; Intem, S.; Hill, A. J., Chromate leaching from inhibited primers. Part I. Characterization of leaching. *Prog. Org. Coat.* **2006,** *56*, 23-32.

10. Prosek, T.; Thierry, D., A model for the release of chromate from organic coatings. *Prog. Org. Coat.* **2004,** *49*, 209-217.

11. Wang, H.; Presuel, F.; Kelly, R. G., Computational modeling of inhibitor release and transport from multifunctional organic coatings. *Electrochim. Acta* **2004,** *49*, 239-255.

12. Zin, I. M.; Howard, R. L.; Badger, S. J.; Scantlebury, J. D.; Lyon, S. B., The mode of action of chromate inhibitor in epoxy primer on galvanized steel. *Prog. Org. Coat.* **1998,** *33*, 203-210.

13. Furman, S. A.; Scholes, F. H.; Hughes, A. E.; Lau, D., Chromate leaching from inhibited primers. Part II: Modelling of leaching. *Prog. Org. Coat.* **2006,** *56*, 33-38.

14. Frankel, G. S., Buchheit, R. G., Jaworowski, M., G. Swain, *Final Report: Scientific Understanding of Non-Chromated Corrosion Inhibitors Function.* Strategic Environmental Research and Development Program: Alexandria, VA, January 2013, 2013; pp 256-370.

15. Markley, T. A.; Mardel, J. I.; Hughes, A. E.; Hinton, B. R. W.; Glenn, A. M.; Forsyth, M., Chromate replacement in coatings for corrosion protection of aerospace aluminium alloys. *Mater. Corros.* **2011,** *62*, 836-840.

16. van Soestbergen, M.; Baukh, V.; Erich, S. J. F.; Huinink, H. P.; Adan, O. C. G., Release of cerium dibutylphosphate corrosion inhibitors from highly filled epoxy coating systems. *Prog. Org. Coat.* **2014,** *77*, 1562-1568.

17. van der Wel, G. K.; Adan, O. C. G., Moisture in organic coatings - a review. *Prog. Org. Coat.* **1999,** *37*, 1-14.

18. Klopffer, M. H.; Flaconneche, B., Transport properties of gases in polymers: Bibliographic review. *Oil Gas Sci. Technol* **2001,** *56*, 223-244.

19. Crank, J., *The Mathematics of Diffusion*. Clarendon Press: **1956**; p 347 pp.

20. George, S. C.; Thomas, S., Transport phenomena through polymeric systems. *Prog. Polym. Sci.* **2001,** *26*, 985-1017.

21. Frank, K.; Childers, C.; Dutta, D.; Gidley, D.; Jackson, M.; Ward, S.; Maskell, R.; Wiggins, J., Fluid uptake behavior of multifunctional epoxy blends. *Polymer* **2013,** *54*, 403-410.

22. Wicks, Z. W., Jr.; Jones, F. N.; Pappas, S. P., *Organic Coatings: Science and Technology, 2nd Ed*. Federation of Societies for Coatings Technology: **1999**; Vol. 71, p 67-73.

23. Pascault, J.-P.; Sautereau, H.; Verdu, J.; Williams, R. J. J.; Editors, *Thermosetting Polymers*. Marcel Dekker, Inc.: **2002**; p 496 pp.

24. Philippe, L.; Sammon, C.; Lyon, S. B.; Yarwood, J., An FTIR/ATR in situ study of sorption and transport in corrosion protective organic coatings. 2. The effects of temperature and isotopic dilution. *Prog. Org. Coat.* **2004,** *49*, 315-323.

25. Vanlandingham, M. R.; Eduljee, R. F.; Gillespie, J. W., Jr., Moisture diffusion in epoxy systems. *J. Appl. Polym. Sci.* **1999,** *71*, 787-798.

26. Foyet, A.; Wu, T. H.; van der Ven, L.; Kodentsov, A.; de With, G.; van Benthem, R., Influence of mixing ratio on the permeability of water and the corrosion performance of epoxy/amine coated un-pretreated Al-2024 evaluated by impedance spectroscopy. *Prog. Org. Coat.* **2009,** *64*, 138-141.

27. Aufray, M.; Roche, A. A., Is gold always chemically passive? *Appl. Surf. Sci.* **2008,** *254*, 1936-1941.

28. Zhang, J.-T.; Hu, J.-M.; Zhang, J.-Q.; Cao, C.-N., Studies of water transport behavior and impedance models of epoxy-coated metals in NaCl solution by EIS. *Prog. Org. Coat.* **2004,** *51*, 145-151.

29. Chiang, M. Y. M.; Fernandez-Garcia, M., Relation of swelling and T_g depression to the apparent free volume of a particle-filled, epoxy-based adhesive. *J. Appl. Polym. Sci.* **2003,** *87*, 1436-1444.

30. Philippe, L.; Sammon, C.; Lyon, S. B.; Yarwood, J., An FTIR/ATR in situ study of sorption and transport in corrosion protective organic coatings. 1. Water sorption and the role of inhibitor anions. *Prog. Org. Coat.* **2004,** *49*, 302-314.

31. Thominette, F.; Gaudichet-Maurin, E.; Verdu, J., Effect of structure on water diffusion in hydrophilic polymers. *Diffus. Defect Data, Pt. A* **2006,** *258-260*, 442-446.

32. Soles, C. L.; Yee, A. F., A discussion of the molecular mechanisms of moisture transport in epoxy resins. *J. Polym. Sci., Part B: Polym. Phys.* **2000,** *38*, 792-802.

33. Cotugno, S.; Larobina, D.; Mensitieri, G.; Musto, P.; Ragosta, G., A novel spectroscopic approach to investigate transport processes in polymers: the case of water-epoxy system. *Polymer* **2001,** *42*, 6431-6438.

34. Musto, P.; Mascia, L.; Ragosta, G.; Scarinzi, G.; Villano, P., The transport of water in a tetrafunctional epoxy resin by near-infrared fourier transform spectroscopy. *Polymer* **1999,** *41*, 565-574.

35. Li, L.; Yu, Y.; Su, H.; Zhan, G.; Li, S.; Wu, P., The diffusion mechanism of water transport in amine-cured epoxy networks. *Appl. Spectrosc.* **2010,** *64*, 458-465.

36. Soles, C. L.; Chang, F. T.; Gidley, D. W.; Yee, A. F., Contributions of the nanovoid structure to the kinetics of moisture transport in epoxy resins. *J. Polym. Sci., Part B: Polym. Phys.* **2000,** *38*, 776-791.

37. Luo, S.; Leisen, J.; Wong, C. P., Study on mobility of water and polymer chain in epoxy for microelectronic applications. *Proc. - Electron. Compon. Technol. Conf.* **2001,** *51st*, 149-154.

38. MacQueen, R. C.; Granata, R. D., A positron annihilation lifetime spectroscopic study of the corrosion protective properties of epoxy coatings. *Prog. Org. Coat.* **1996,** *28*, 97-112.

39. Patil, P. N.; Rath, S. K.; Sudarshan, K.; Dutta, D.; Patri, M.; Pujari, P. K., Effect of cross-link density on the free volume and segmental relaxation in epoxy resin studied by positron annihilation apectroscopy. *AIP Conf. Proc.* **2010,** *1313*, 298-300.

40. Wong, T. C.; Broutman, L. J., Moisture diffusion in epoxy resins. Part I. Non-fickian sorption processes. *Polym. Eng. Sci.* **1985,** *25*, 521-8.

41. Zarzycki, R.; Modrzejewska, Z.; Nawrotek, K., Drug release from hydrogel matrices. *Ecol. Chem. Eng. S* **2010,** *17*, 117-136.

42. Wu, Y.; Joseph, S.; Aluru, N. R., Effect of cross-linking on the diffusion of water, ions, and small molecules in hydrogels. *J. Phys. Chem. B* **2009,** *113*, 3512-3520.

43. Khandai, M.; Chakraborty, S.; Sharma, A.; Panda, D.; Khanam, N.; Panda, S. K., Development of propranolol hydrochloride matrix tablets: an investigation on effects of combination of hydrophilic and hydrophobic matrix formers using multiple comparison analysis. *Int. J. Pharm. Sci. Rev. Res.* **2010,** *1*, 1-7.

44. Weber, J.; Atanasoska, L.; Eidenschink, T. Polymeric corrosion-resistant coatings for biodegradable metallic implants. US20070224244A1, **2007**.

45. Kasargod, S. S.; Adib, F.; Neogi, P., Diffusion in inhomogeneous polymer membranes. *J. Chem. Phys.* **1995,** *103*, 7114-19.

46. Zhang, J.-T.; Keller, T. F.; Bhat, R.; Garipcan, B.; Jandt, K. D., A novel two-level microstructured poly(N-isopropylacrylamide) hydrogel for controlled release. *Acta Biomater.* **2010,** *6*, 3890-3898.

47. Krakovsky, I.; Szekely, N., Small-angle neutron scattering study of nanophase separated epoxy hydrogels. *J. Non-Cryst. Solids* **2010,** *356*, 368-373.

48. Tabor, Z.; Warszynski, P., Modeling dissolution controlled release of inhibitor from a damaged coating. *Corros. Sci.* **2014,** *82*, 290-296.

49. Yasakau, K. A.; Tedim, J.; Zheludkevich, M. L.; Ferreira, M. G. S., Smart self-healing coatings for corrosin protection of aluminium alloys. *Woodhead Publ. Ser. Met. Surf. Eng.* **2014,** *64*, 224-274.

50. Ghosh, S. K. In *Self-healing materials: fundamentals, design strategies, and applications*, Wiley-VCH Verlag GmbH & Co. KGaA: **2009**; pp 1-28.

51. Mahdavian Ahadi, M.; Mohammadzadeh Attar, M. Chromate-free corrosion-resistant coatings containing hybrid organic-inorganic corrosion inhibitors. EP2241591A1, **2010**.

52. Montemor, M. F., Functional and smart coatings for corrosion protection: A review of recent advances. *Surf. Coat. Technol.* **2014**, Ahead of Print.

53. Makhlouf, A. S. H.; Editor, *Handbook Of Smart Coatings For Materials Protection*. Woodhead Publishing Ltd.: **2014**; p 628 pp.

54. Zheludkevich, M. L.; Tedim, J.; Ferreira, M. G. S., "Smart" coatings for active corrosion protection based on multi-functional micro and nanocontainers. *Electrochim. Acta* **2012,** *82*, 314-323.

55. Li, L.; Yu, Y.; Wu, Q.; Zhan, G.; Li, S., Effect of chemical structure on the water sorption of amine-cured epoxy resins. *Corros. Sci.* **2009,** *51*, 3000-3006.

56. Pramanik, M.; Fowler, E. W.; Rawlins, J. W., Another look at epoxy thermosets correlating structure with mechanical properties. *Polym. Eng. Sci.* **2014,** *54*, 1990-2004.

57. van Krevelen, D. W., *Properties of Polymers, 4th ed.*; Elsevier: Amsterdam, **2009**.

58. Patil, P. N.; Rath, S. K.; Sharma, S. K.; Sudarshan, K.; Maheshwari, P.; Patri, M.; Praveen, S.; Khandelwal, P.; Pujari, P. K., Free volumes and structural relaxations in diglycidyl ether of bisphenol-A based epoxy-polyether amine networks. *Soft Matter* **2013,** *9*, 3589-3599.

59. Mezzenga, R.; Boogh, L.; Manson, J.-A. E., Evaluation of solubility parameters during polymerisation of amine-cured epoxy resins. *J. Polym. Sci., Part B: Polym. Phys.* **2000,** *38*, 1883-1892.

60. Hansen, C. M.; Editor, *Hansen Solubility Parameters: A User's Handbook*. CRC Press LLC: **2007**; p 519 pp.

61. Rezaei, F.; Sharif, F.; Sarabi, A. A.; Kasiriha, S. M.; Rahmanian, M.; Akbarinezhad, E., Evaluating water transport through high solid polyurethane coating using the EIS method. *J. Coat. Technol. Res.* **2010,** *7*, 209-217.

62. Nakka, J. S. Tailoring of epoxy material properties. Defense, Delft University of Technology, Delft, Netherlands, 2010.

63. Nguyen, T.; Byrd, E.; Bentz, D.; Lin, C., In situ measurement of water at the organic coating/substrate interface. *Prog. Org. Coat.* **1996,** *27*, 181-193.

64. Jansson, A.; Boissier, C.; Marucci, M.; Nicholas, M.; Gustafsson, S.; Hermansson, A.-M.; Olsson, E., Novel method for visualizing water transport through phase-separated polymer films. *Microsc. Microanal.* **2014,** *20*, 394-406.

CHAPTER II - METHODS

This research is divided into three separate sections, each of which involves a separate series of epoxy-amine networks. These systems utilize a number of unique monomer components which afford the ability to modify matrix structural and compositional features including crosslink density, T_g, and hydrophilicity. An explanation of each series formulation and sample preparation techniques are given below.

2.1 Materials

2.1.1 Chapter III Network Series

A series of five different epoxy-amine networks were formulated using either a diglycidyl ether of Bisphenol A (DGEBA) epoxy resin, Epon™ 825 (E825, reported Epoxy Equivalent Weight of 175-180 g/eq), or a cyclohexyl (hydrogenated) derivative, Eponex™ 1510 (E1510, EEW of 205-215 g/eq), both supplied by Hexion (Momentive Specialty Chemicals). Figure 2.1 exhibits the chemical structures of the epoxy resins along with the five diamine crosslinking agents: 4,4'-diaminodiphenyl sulfone (DDS, Amine-Hydrogen Equivalent Weight = 62.075 g/eq, supplied by TCI America), 4,4'-diaminodiphenyl methane (DDM, AHEW = 49.57 g/eq, supplied by Acros Organics), Jeffamine EDR148 (AHEW = 74 g/eq), Jeffamine ED900 (AHEW = 250 g/eq), and Jeffamine THF100 (AHEW = 260 g/eq), supplied by Huntsman Corporation. All the chemicals were used as received unless mentioned otherwise. In addition to model epoxy-amine networks, a fully formulated coating was selected for comparison in select analyses. Deft® 02GN084, supplied by PPG Aerospace Products, is a two-component solvent-borne non-chrome

epoxy polyamide primer (classified as a MIL-PRF-23377K Type I Class N primer) containing a praseodymium oxide-type corrosion inhibitor.

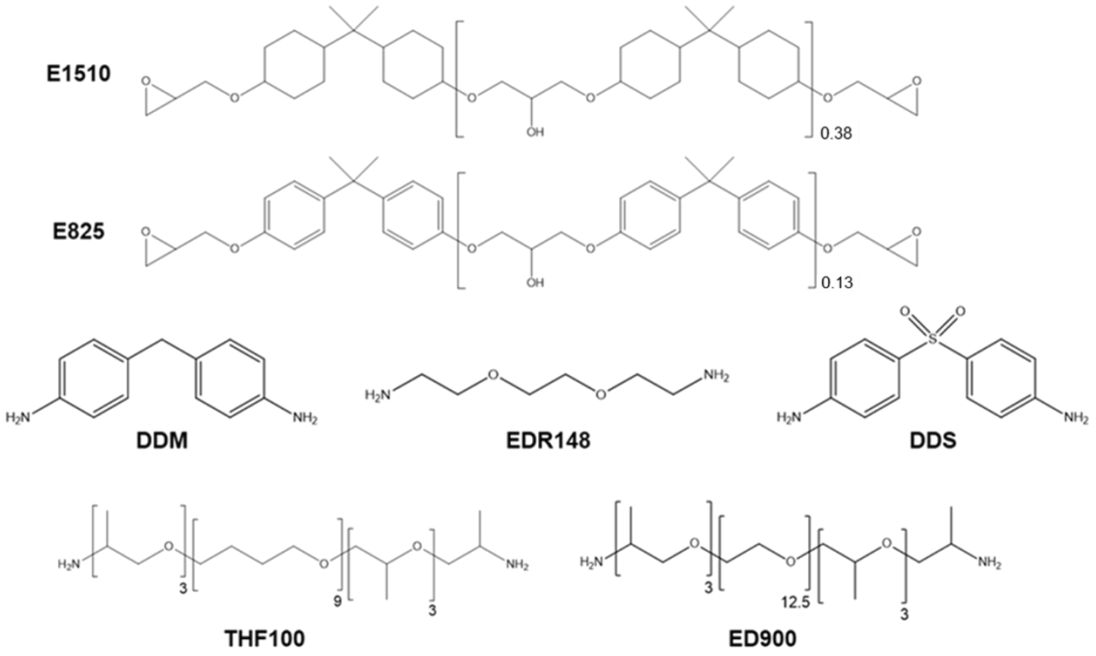

Figure 2.1 Chemical structures of Chapter III epoxy-amine network monomers.

2.1.2 Epoxy-Amine Network Formulation and Sample Preparation – Chapter III

All epoxy networks were formulated to 1:1 stoichiometry (epoxy to amine-hydrogen) with their corresponding amine curing agents. Four of the networks were composed of E1510 crosslinked by either EDR148, DDM, THF100, or ED900 while the fifth network consisted of E825 crosslinked with DDS. Polymer samples were prepared by first combining the appropriate quantities of epoxy resin with liquid diamine curing agent (EDR148, THF100, or ED900) and stirring by hand prior to mixing at high speeds using a FlackTek SpeedMixer. These were then placed in a vacuum oven at low pressure for approximately five minutes to remove any air bubbles. Both DDM and DDS are solids (powders) at room temperature and required high temperatures following mixing to

melt and fully combine with the epoxy resins. The E1510-DDM and E825-DDS stoichiometric quantities were combined in a scintillation vial and mixed by hand then placed in an oven at 150 °C with occasional stirring until completely homogeneous before removing any remaining air bubbles via vacuum oven. Sheets of crosslinked epoxy-amine network films were prepared by curing the liquid mixtures while sandwiched between two glass plates with small PTFE spacers of approximately 0.30 mm placed at the corners between the plates to ensure uniform thickness between samples. Prior to addition of the monomer mixture the plates were sprayed with a thin layer of silicone-free release agent then placed in an oven pre-heated to the temperature corresponding with the first cure profile temperature for the appropriate resin-curing agent combination. The degassed epoxy-amine mixture was then poured onto the bottom glass plate before slowly applying the top plate to avoid inclusions of air bubbles.

Crosslinking proceeded according to the cure profiles shown in Table 2.1, which were determined from analysis of reaction exothermic peak data provided by heat/cool/heat cycles of differential scanning calorimetry (DSC) carried out on epoxy-amine monomer mixture samples to ensure each polymer reached its ultimate glass transition temperature ($T_{g\infty}$) through complete conversion. Following the cure process the polymer and glass was allowed to cool slowly to room temperature before separating the plates and removing the solid epoxy-amine films. Films were stored in plastic bags and samples for various analyses were removed using blades or hollow punches. Larger bulk samples of E1510-EDR148 were produced by curing bars in silicone molds with wells of approximate dimensions of 76 x 15 x 12.7 mm (L x W x T) using the same cure profile then cut to smaller proportions using a band saw. Free films of the aircraft primer

Deft 02GN084 were obtained by combining the coating base and catalyst components in quantities specified by the manufacturer then mixed thoroughly. Coatings were prepared by applying the mixture to a polypropylene slab using a drawdown bar (6 wet mils) and allowed to dry overnight before curing at 75 °C for 4 hours then cooled to room temperature slowly at which point films were removed using a razor blade.

Table 2.1

Epoxy-Amine Network Cure Profiles

Epoxy-Amine Combination	Primary Cure (°C/hours)	Secondary Cure (°C/hours)
E1510-THF100	35 / 5	75 / 24
E1510-ED900	35 / 5	75 / 24
E1510-EDR148	60 / 2	120 / 2
E1510-DDM	90 / 2	150 / 1
E825-DDS	150 / 2	250 / 1

2.1.3 Chapter IV Network Series

A series of nine different epoxy-amine networks were formulated using diglycidyl ether of Bisphenol A (DGEBA) liquid epoxy resin, Epon™ 825 (E825, reported Epoxy Equivalent Weight of 175-180 g/eq) supplied by Hexion (Momentive Specialty Chemicals) and a mixture of amine-type reactants including the primary monoamine chain extender benzylamine (BA, AHEW = 53.575 g/eq, supplied by Acros Organics) or di-secondary amine PolyLink™ 4200 (PL4200, AHEW = 155.24 g/eq, supplied by The Hanson Group, LLC) along with tetrafunctional amine crosslinking agents Jeffamine ED600 (ED600, AHEW = 132 g/eq, supplied by Huntsman Corporation) and 2-methyl-1,5-pentamethylene diamine (MPMD, AHEW = 29.05 g/eq, supplied by Sigma Aldrich) or 1,3-bisaminocyclohexane (1,3-BAC, AHEW = 35.56 g/eq, supplied by Acros Organics). Figure 2.2 exhibits the chemical structures of the epoxy resin along in

addition to the chain extenders and crosslinkers. All the chemicals were used as received unless mentioned otherwise.

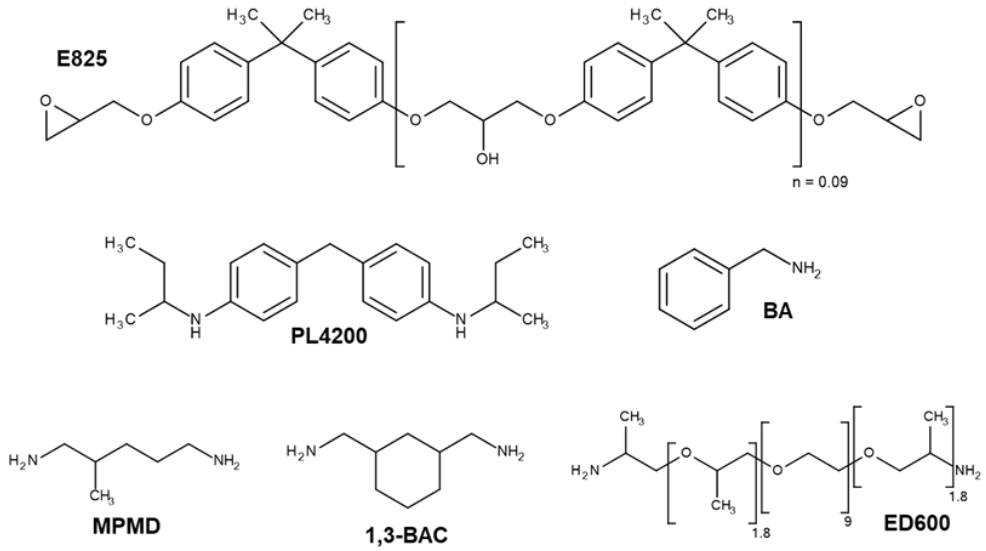

Figure 2.2 Chemical structures of Chapter IV epoxy-amine network monomers.

Epoxy resin (top), di-secondary amine and primary monoamine chain extenders (middle), and tetrafunctional amine crosslinking network reactants (bottom).

2.1.4 Epoxy-Amine Network Formulation and Sample Preparation – Chapter IV

Formulating the network series was carried out using a crosslinking density estimation method described elsewhere[1] that estimates the molecular weight between crosslinks, M_c, of a fully converted epoxy-amine network containing a bifunctional chain extender and multifunctional crosslinking agent as:

$$M_c = \frac{2M_E + M_A}{n_c}$$

where M_E and M_A are the molecular mass of the epoxy and amine components, respectively, and n_c is the number of covalent crosslinks per constitutional crosslinking unit (CCU). Within a network consisting of bifunctional epoxy resin (or chain extended

epoxy-functional oligomer) and tetrafunctional amine crosslinking agent the CCU is given as an epoxy-amine-epoxy trimer and n_c is reduced to:

$$n_c = 1 + (4x + 3)$$

where x is the degree of conversion. For the purpose of network series formulation all thermosets were assumed to reach 100% conversion and each CCU consisted of either an epoxy-amine-epoxy trimer or extended epoxy-amine-extended epoxy trimer whereby the amine was given by either ED600 or 1,3-BAC (NS1)/MPMD (NS2) and under these premises the number of covalent crosslinks within each CCU, n_c, is 2. Using a specific target amine content (for example, 50% ED600 and 50% 1,3-BAC by amine-hydrogen equivalents) and chain extension aim (for example, 50% of all epoxide groups available for reaction with amine arise from E825-BA-E825 trimers) the weighted proportions of each CCU can be adjusted until the estimated M_c matches the intended goal. This is repeated until nine separate networks are produced which represent of the three crosslink density and amine content ranges. An example of the actual formulated masses of a set of networks is given in Table 2.2.

Table 2.2

Epoxy-Amine Network Formulations of Network Series 2

α-I		**mass**	**β-I**		**mass**	**γ-I**		**mass**
High T_g	E825	70.33	**Mid T_g**	E825	73.08	**Low T_g**	E825	75.22
High M_c	PL4200	29.66	**High M_c**	PL4200	26.91	**High M_c**	PL4200	24.77
76 eq%	MPMD	4.59	*47 eq%*	MPMD	3.29	*25 eq%*	MPMD	1.94
24 eq%	ED600	6.59	*53 eq%*	ED600	16.89	*75 eq%*	ED600	26.47
	M_c	*1102.74*		**M_c**	*1102.9*		**M_c**	*1101.88*
α-II		**mass**	**β-II**		**mass**	**γ-II**		**Mass**
High T_g	E825	82.87	**Mid T_g**	E825	85.01	**Low T_g**	E825	87.15
Mid M_c	PL4200	17.12	**Mid M_c**	PL4200	14.98	**Mid M_c**	PL4200	12.84
72 eq%	MPMD	7.52	*50 eq%*	MPMD	5.60	*28 eq%*	MPMD	3.34
28 eq%	ED600	13.30	*50 eq%*	ED600	25.48	*72 eq%*	ED600	39.15
	M_c	*839.64*		**M_c**	*838.62*		**M_c**	*837.61*
α-III		**Mass**	**β-III**		**Mass**	**γ-III**		**Mass**
High T_g	E825	93.88	**Mid T_g**	E825	98.16	**Low T_g**	E825	99.69
Low M_c	PL4200	6.11	**Low M_c**	PL4200	1.83	**Low M_c**	PL4200	0.30
90 eq%	MPMD	12.89	*46 eq%*	MPMD	7.28	*30 eq%*	MPMD	4.91
10 eq%	ED600	6.51	*54 eq%*	ED600	38.87	*70 eq%*	ED600	52.11
	M_c	*564.33*		**M_c**	*562.3*		**M_c**	*562.16*

Note: Masses are given in grams. Average molecular mass between crosslinks (M_c) is given in g/mol.

Bulk polymer samples were prepared by first combining the appropriate quantities of epoxy resin with PL4200 or BA chain extender (EDR148, THF100, or ED900) in a container and stirring by hand prior to mixing at high speeds using a FlackTek SpeedMixer. These were then placed on a rolling mill for approximately 1 hour and allowed to pre-react before adding the crosslinking agents (ED600 and MPMD or 1,3-BAC). Once all reactants were combined and mixed the containers were agitated via rolling mill for 2-3 hours before casting or applying. Larger bar samples were produced by casting mixtures into silicone molds with wells 60 x 10 x 1 mm (L x W x T) while films were prepared by applying the liquid mixtures over polypropylene slabs (for free films) or 6” x 3” S-36 SAE CRS 1008/1010 steel Q-panels from Q-Lab (for substrate-

bound coatings) which were degreased with acetone prior to application. Films were applied using a drawdown bar applicator at 6 wet mils and all samples were allowed to dry and vitrify under ambient conditions overnight prior to subjecting to the curing process. The cure profile was determined by examination of the reaction mixture exothermic activity via differential scanning calorimetry and was applied to all networks regardless of preparation method or sample type. The cure schedule consisted of 2 hours at 60 °C followed by 1 hour at 120 °C then a slow cool-down to room temperature.

2.1.5 Chapters V & VI Network Series

A diglycidyl ether of Bisphenol-A (DGEBA)-based liquid epoxy, EPON™ Resin 825, (E825, epoxy equivalent weight (EEW) 176.16 g/equivalent) was donated by Momentive (Hexion). Diamine modifiers, Jeffamine® THF100, (amine hydrogen equivalent weight (AHEW) 260 g/eq) and Jeffamine® ED900 (AHEW 250 g/eq), were donated by Huntsman Corporation. A commercial polyamidoamine, Ancamide® 2445, (AHEW 133 g/eq), was donated by Air Products. TiPure™ R-902+ (DuPont) was used as the primary pigment with strontium chromate ($SrCrO_4$, Alfa Aesar) as the chromate-based pigment corrosion inhibitor while Halox® 650 (H650, a benzothiazolylthiosuccinic acid derivative, Israel Chemicals Limited\Advanced Additives) was used as the CRI additive. Chemical structures of the various network components and CRI are given in Figure 2.3.

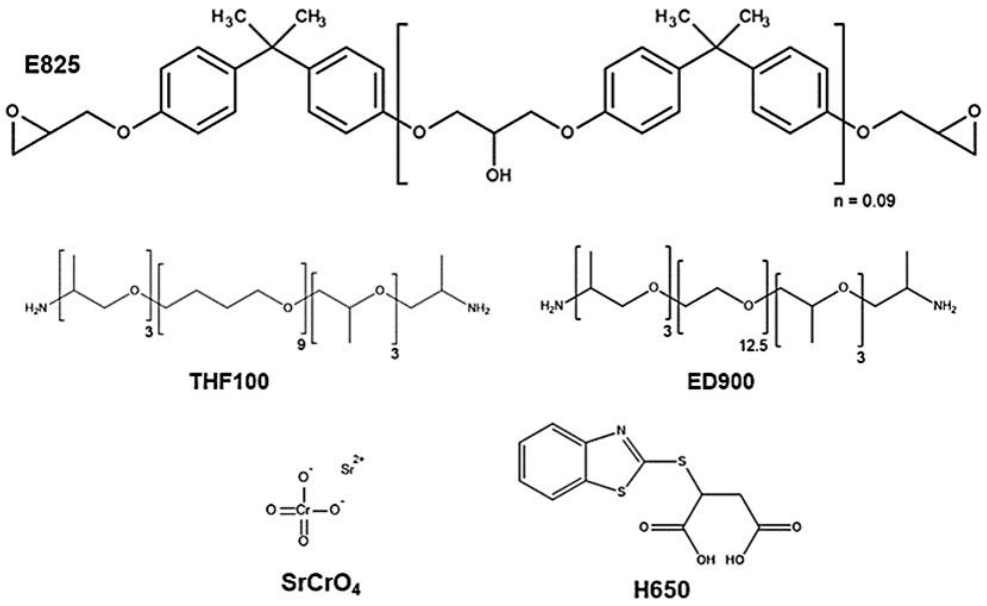

Figure 2.3 Chemical structures of epoxy resin, amine-functional polyethers, chromate-based inhibitor, and organic-type CRI pigment described in Chapters V and VI.

The dispersant, Disperbyk®-161, was donated by BYK Additives and Instruments (ALTANA Group). Tripropylene glycol n-butyl ether (TPnB) (Dowanol™ TPnB, Dow Chemical Company), parachlorobenzotrifluoride (PCBTF, Sigma Aldrich), and sec-butyl alcohol (Fisher Chemical) were the solvents of choice. The coatings were applied to untreated 5" x 3" 2024T3 aluminum and 6" x 3" S-36 CRS SAE 1008/1010 steel Q-panels from Q-Lab which were degreased with acetone prior to application.

2.1.6 Bulk Polymer Sample and Film Formation – Chapters V & VI

Contained in five scintillation vials, varying ratios of THF100 and ED900 (10:90, 25:75, 50:50, 75:25, and 90:10 by equivalent) were blended with the polyamidoamine hardener while maintaining 85% equivalent of polyamide in the blend. Each mixture was added to the epoxy resin at 1:1 epoxy:amine stoichiometry, stirred by hand for two minutes, blended three times for 90 seconds at 1200 rpm in a centrifugal FlackTek SpeedMixer and

de-aerated via ultrasonication for 3 minutes. Free films were prepared via drawdown bar (6 wet mils) on polypropylene sheets while sample bars (50 x 5 x 1.3 mm) were prepared by casting the blends into silicone molds containing 50 x 5 x 1.3 mm wells. Samples were allowed to vitrify overnight under ambient conditions before a pre-cure stage at 60 °C for one hour followed by a post-cure stage at 120 °C for two hours, and 75 °C overnight.

2.1.7 Pigmented Coatings Formulation and Preparation – Chapters V & VI

Two different control inhibitor packages and hence two main types of coating systems were prepared: one which included a chromate-based corrosion inhibitor pigment ($SrCrO_4$), while the other implemented an organic CRI additive (Halox 650), both included in quantities recommended by the manufacturers. Part A of the coatings was formulated with epoxy resin, TiO_2 (TiPure R-902+), and the corrosion inhibitors using a solvent blend of equal parts of TPnB, PCBTF, and 2-butanol by weight (Table 2.3), using ceramic beads to disperse the pigments on a roller mill for 48 hours. Approximately 0.1 wt% Disperbyk-161 was added to aid in the organic corrosion inhibitor dispersion.

Table 2.3

Coating Part A Quantities

Coating	Epoxy Resin	TiO_2	Inhibitor	Solvent
Chromate ($SrCrO_4$)	143.53	71.75	7.46	64.58
CRI (H650)	143.53	71.75	6.65	76.61

Note: Masses are given in grams.

Part B of the coatings was prepared by blending the polyamide (85% by equivalents) with various ratios (all at 15% by equivalents) of ED900 and THF100 mixtures (10:90, 25:75, 50:50, 75:25, and 90:10 by equivalent), comprising the remaining 15% by equivalents. The overall coating formulations (for chromate-containing systems)

are shown in Table 2.4. Chromate-containing coatings were formulated to a solids content of 79.8% while CRI systems were formulated to 77.4% solids and both systems with a 7.11% pigment-volume concentration (PVC). Parts A and B were blended and applied on S-36 steel and 2024T3 aluminum panels using a 6 wet mil drawdown bar and automatic drawdown instrument. The films were dried overnight under ambient conditions before curing at 60 °C for 1 hour, followed by 120 °C for 2 hours. Free films were obtained by applying 6 wet mil drawdowns on polypropylene slabs that were dried overnight prior to curing at 80 °C for 48 hours. Coated and scribed panels were placed in a salt-fog chamber (Q-FOG CCT-600) for 440 hours and evaluated as per ASTM B117. Direct weathering (natural outdoor exposure) was carried out on coated and scribed panels secured to open-back metal racks facing south at an angle of 120° to the horizon positioned on the roof of the Polymer Science Research Center in Hattiesburg, MS (18.91 °C average annual temperature, 156.49 cm average annual rainfall). Digital images were taken occasionally to monitor corrosion progress and after 440 hours, the relative corrosion areas were approximated using Adobe Acrobat software. The coated panels were evaluated via gloss at 60° (BYK micro-TRI-gloss 4446), Koenig hardness (TQC SP0500 Pendulum Hardness Tester), scratch adhesion, impact resistance at 60 lb., conical mandrel bend, and methyl ethyl ketone (MEK) double rubs.

Table 2.4

Coating Part B (Chromated) Quantities

Formulation	Polyamide	THF100	ED900	Solvent	Part A
THF10-ED90	12.85	0.50	3.87	39.54	7.12
THF25-ED75	12.85	1.24	3.29	39.70	7.11
THF50-ED50	12.85	2.36	2.11	39.59	7.11
THF75-ED25	12.85	3.34	1.13	39.59	7.11
THF90-ED10	12.85	3.99	0.45	39.71	7.12

Note: Masses are given in grams.

Pull-off adhesion tests were performed using a 10 kN Mechanical Testing System load frame and a 2.5 kN load cell, at a strain rate of 0.5 mm/min. The adaptors for the load frame used in pull-off testing were custom made to hold a coated panel on the bottom and fit an Elcometer 20 mm diameter stud on the top. Studs applied to the coating are prepared by abrading the surface first with 80 grit sand paper and then with Scotch Brite pads and rinsing with acetone. Likewise, the stud attachment face was abraded with Scotch Brite prior to adhering. Studs were adhered to the coating surface with Scotch Weld DP460 and were applied by hand. The adhesive was allowed to cure for 24 hours under ambient conditions before testing.

2.2 Experimental Techniques

2.2.1 Dynamic Mechanical Analysis (DMA) and Relative Humidity-Controlled Dynamic Mechanical Analysis (RH-DMA).

Dynamic mechanical analysis was carried out on free films with approximate dimensions of 12 x 5 x 0.3 mm on a Q800 DMA from TA Instruments, Inc. Single frequency temperature ramp testing was conducted in tensile mode with a heating rate of 2 °C per minute, a strain rate of 0.1%, a pre-load force of 0.01 N, and frequency of 1 Hz.

Storage Modulus (E′), Loss Modulus (E″), and Tan Delta (tan δ) signals were monitored over the entire temperature range, the limits of which varied depending on the polymer being analyzed. Relative humidity-controlled analysis was carried out on a Q800 instrument outfitted with a RH controller in tensile mode between 15 and 115 °C using a heating rate of 1 °C per minute, strain rate of 0.1%, 0.01 N pre-load force, and strain frequency of 1 Hz.

2.2.2 Differential Scanning Calorimetry (DSC).

Differential scanning calorimetry (DSC) was carried out on both free film and bulk polymer (bar) samples weighing between 5-20 mg on a Q2000 Differential Scanning Calorimeter from TA Instruments, Inc. Once prepared, polymer samples were placed in aluminum pans and sealed with crimped lids before placing within the instrument along with an empty reference aluminum pan. Heat flow and heat capacity signals were monitored during heat/cool/heat cycles between -150 and 150 °C with heating rates of 10 °C and cooling rates of 5 °C.

2.2.3 Dynamic Vapor Sorption (DVS).

Dynamic vapor sorption was conducted using a Q5000 Sorption Analyzer from TA Instruments, Inc. Circular discs with diameters of 6.3 mm and approximately 0.3 mm thickness were placed in quartz pans and subjected to 5, 22, 44, 57, 75, 86, or 95% RH environments at 25 °C following a drying step at 60 °C and 0% RH. Samples were exposed to the various moisture levels while the weight change (%) was monitored via microbalance until a saturation or near-equilibrium stage was achieved, the time of which varied between the different epoxy-amine formulations.

2.2.4 Gravimetric and Volumetric Analysis of Bulk Polymers.

Rectangular samples of cured E1510-EDR148 with dimensions of approximately 15 x 12.7 x 6 mm were prepared and their dimensions were measured with a digital caliper measuring tool while their masses were measured on a Mettler Toledo XS104 analytical balance while dry and following immersion in DI water or exposed to a number of different relative humidity levels. Additionally, the densities (ρ) of samples were determined via the water displacement method using a density kit in conjunction with the XS104 balance and measured at room temperature. Essentially, if ρ_0 is the density of water, the density of any solid can be written as:

$$\rho = \frac{A}{A - B}(\rho_0 - \rho_L) + \rho_L$$

wherein A is the weight of the sample in air, B is the weight of the sample in water, and ρ_L is the density of air (0.0012 g/cm^3).[1]

2.2.5 Water Vapor Transmission Rate Analysis (WVTR).

Water vapor transmission rate analysis was carried out using a dry cup method on a VTI-SA sorption analyzer from TA Instruments, Inc. Samples of approximately 10 mm diameter and 0.3 mm thickness were placed over a small aluminum cup that was loaded with a few milligrams of desiccant then sealed and held in place with a thin ring of double sided tape. The assembled film and cup were then placed within the microbalance gravimetric sorption analysis instrument and the sample was subjected to a 95% RH environment at 25 °C following an initial drying step at 0% RH and 60 °C for 2 hours. Single sorption experiments were held for up to 600 minutes while cyclic testing

implemented alternating steps of 250 minutes. The water vapor transmission rate is calculated via the following equation:

$$WVTR = \frac{permeant\ amount \times sample\ thickness}{sample\ area \times test\ time}$$

Alternatively, for some samples water permeation testing was carried out using a permeability cup test method (ASTM E-96). A PTFE cup with matching lid was applied over a sample film with diameter of 30 mm and thickness of 0.30 mm. The cap film is secured to the cup with a threaded lid and sealed with an appropriately sized flexible O-ring to prevent loss of water. Films were dried in a vacuum oven overnight prior to the test start and once assembled (with cup, film, lid, and water) the cups were placed inside humidity chambers with occasional weighing before and during RH exposure for a period of one week with five distinct RH levels were chosen for analysis (43, 57, 75, 83, and 95%). The permeability was calculated according to:

$$P = \frac{m \cdot l}{t \cdot A \cdot \Delta P_v} = I \cdot \frac{l}{A \cdot \Delta P_v}$$

where m is the mass of the cup at time t, l is sample thickness, A is the exposed film area, ΔP_v is the vapor pressure differential between the interior and exterior of the sealed cup, and I is the slope of the graph obtained from plotting the measured cup mass as a function of elapsed test time.

2.2.6 Relative Humidity-Controlled Oxygen Permeability Analysis.

Oxygen barrier of the LNC films and neat polymer were measured at 25 °C and 1 atm partial oxygen pressure difference using a commercially manufactured diffusion apparatus, OX-TRAN 2/21 ML (MOCON, Inc.) which employs a continuous-flow

method (ASTM D3985-81) with nitrogen as a carrier gas to measure oxygen flux through polymeric films under varying relative humidity conditions. Film samples with a surface area of 50 cm^2 and 0.3 mm thickness were used for testing. The specimens were conditioned in a vacuum oven or humidity chamber at a specified RH until an equilibrium water content was reached (as determined by DVS measurements for each formulation and RH). Oxygen flux, $J_{(t)}$, was measured and a solution to Fick's second law was employed, as shown in the following equation, to fit the experimental oxygen flux data, where Δp is the oxygen partial pressure difference across the film (1 atm here), l is the thickness of the film, and t is the time (in seconds).

$$J_{(t)} = \frac{P\Delta p}{l}\left[1 + 2\sum_{n=1}^{\infty}(-1)^n \, exp\left(-\frac{D\pi^2 n^2 t}{l^2}\right)\right]$$

From this two parametric fit, the permeability P and diffusivity D were calculated as described elsewhere.[2] The solubility (S) was calculated from the relationship $P = D \times S$. Values of permeability coefficients in this study are given in Barrer (1 Barrer = 10^{-10} $(cm^3\,O_2) \cdot cm \cdot cm^{-2} \cdot s^{-1} \cdot cmHg^{-1}$ = 3.35 x 10^{-16} $mol \cdot m \cdot m^{-2} \cdot s^{-1} \cdot Pa^{-1}$). The permeability coefficient P can also be calculated directly from the steady-state flux J_∞ value as follows $P = J_\infty \cdot l / \Delta p$.

2.2.7 Attenuated Total Reflectance Infrared Spectroscopy (ATR-IR).

Attenuated total reflected Fourier transform infrared spectroscopy (ATR-FTIR) was conducted on pigmented substrate-bound coatings using a Mettler Toledo ReactIR™ iCIR10 along with a K-conduit attached to a Durasampler™ temperature controlled stainless steel surface ATR accessory as shown in Figure 2.4. Epoxy primer coating mixtures were applied using a drawdown bar at 6 wet mils and cured onto the

Durasampler™ stainless steel substrate that incorporates a 3-bounce ATR crystal diamond interface with a 45° angle of reflectance. The coatings were cured onto the accessory but because the stage could not be exposed to high temperatures (> 100 °C) the curing schedule was modified to 6-8 hours at 80 °C after overnight drying. The coating was measured from the substrate interface for the diffusion of either DI H_2O or 5-15 wt% NaCl solution through a dried/unexposed film. In some experiments the films were uncovered and dried for subsequent exposure to liquid. In most instances the appearance of water was indicated at 30-40 minutes and saturation or equilibrium conditions were met within 24 hours. Using ATR-FTIR allowed for a discrete volume of observation to calculate concentrations of solvent in the presence of a polymer film.[4] The depth of penetration, d_p, for the coating system was less than the total thickness of the coating, which is given by:

$$d_p = \frac{\lambda}{2\pi[n_1^2\, sin^2\, \theta\, -\, n_2^2]^{1/2}}$$

where n_1 is the rarer medium, n_2 is the refractive index of the propagating medium, and the equation is wavelength-dependent as given by λ in μm. Because the depth of penetration of the coating was limited to the region of the polymer and the polymer was always in range of the IR depth of penetration, the water fraction was the limiting factor for calculating the volume of the observation space. The calculated volume of observation was based on the d_p of 1.5 μm at 3300 cm^{-1} which resulted in 4.71 x106 μm^3.

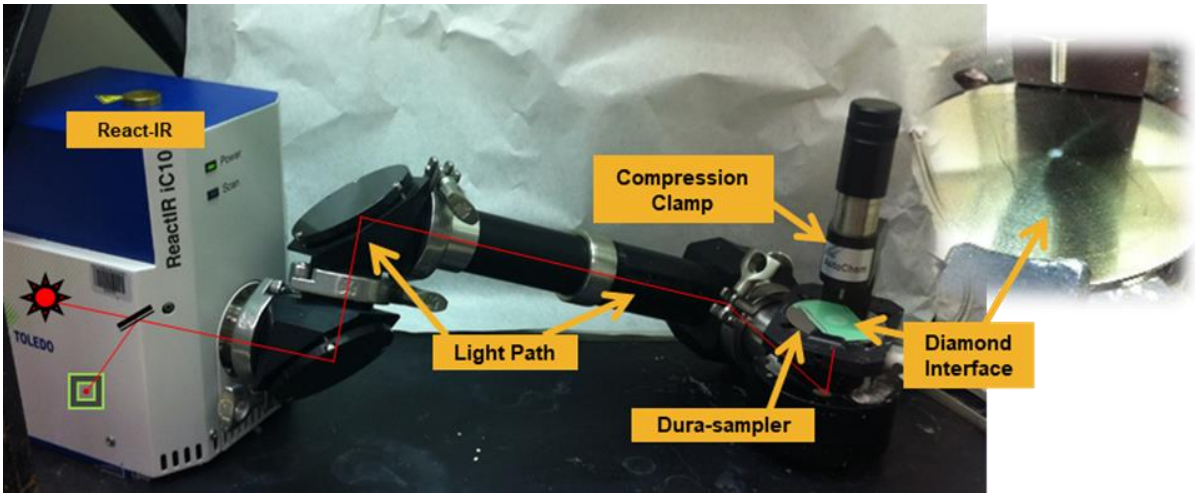

Figure 2.4 Demonstration of ATR-IR setup for evaluation of substrate-bound coating.

Calculating the rate of diffusion in the polymer coating by ATR-FTIR was accomplished by using established methods which take into account the limit of penetration for the IR wave into the sample.[4] The general relationship between IR signal and diffusion is given by:

$$\frac{A_t}{A_\infty} = 1 - \frac{8\gamma}{\pi[1-\exp(-2\gamma L)]} \cdot \left[\frac{exp\left(-\frac{D\pi^2 t}{4L^2}\right)\left(\frac{\pi}{2L}\exp(-2\gamma L) + (2\gamma)\right)}{\left(4\gamma^2 + \frac{\pi^2}{4L^2}\right)}\right]$$

where γ is the penetration depth, L is the coating thickness, and D is the diffusion coefficient. Wavelengths of interest included the H–O–H stretch (1650 cm^{-1}) and –OH asymmetric bend (3700-3000 cm^{-1}), which was resolved into separate components according to polymer-water interaction and lead to the ratio of different types of hydrogen bonded water in the network, i.e., S_2'' (~3320 cm^{-1}), S_2' (~3224 cm^{-1}), S_1 (~ 3433 cm^{-1}), and S_0 (~ 3555 cm^{-1}), according to the work of Musto and co-workers.[5]

2.2.8 Relative Humidity-Controlled Positron Annihilation Lifetime Spectroscopy (RH-PALS).

Relative humidity-controlled positron annihilation lifetime spectroscopy (RH-PALS) measurements were carried out using an in-house custom instrument employing a ^{22}Na positron source. Two specimens of approximately 0.30 mm and 1 cm diameter were sandwiched between the positron source and a custom built apparatus consisting of Hamamatsu H3378-50 photomultiplier tubes with attached BaF_2 scintillation crystals was used to detect positron birth and death signals. A fast-fast coincidence system based on commercial EC&G Ortec NIM modules (model 583 constant fraction discriminators), and a model 566 time-to-amplitude converter was used. Because only the longest life-time signal was used for analysis, no source corrections were carried out. The time resolution was determined using the fitting program "Resolution" of the PATFIT-88 software, which decomposed spectra into three discrete lifetime components, the longest of which was attributed to *o*-Ps pick-off annihilation.

For the calculation of free volume hole sizes, a simple quantum mechanical model proposed by Tao-Eldrup was used, which assumes the Ps to be confined to a spherical potential well with infinitely high walls.[5] In the model the electron density of the surrounding molecules is approximated by an electron layer of constant thickness. In polymers, Ps is trapped by local free volumes (holes) of the disordered structure, the size of which determines the *o*-Ps τ_3 lifetime typically in the nanosecond (ns) range. From τ_3 the mean radius R of the local free volume, $<V_h>$, is calculated according to the semi-empirical equation:

$$\tau_3 = 0.5\left[1 - \frac{R}{R_0} + \frac{1}{2\pi}\sin\left(\frac{2\pi R}{R_0}\right)\right]^{-1}$$

where $\Delta R = R_0 - R = 0.1656$ nm. The pre-factor represents the Ps annihilation rate at 0.5 ns. The quantities R and ΔR are the radius of the hole and an empirical parameter that describes the thickness of the electron layer, respectively. The value of ΔR has been previously determined to be 1.656 Å by fitting the equation to positron lifetime values measured in systems of known hole sizes. Because the *o*-Ps lifetime is expected to show a distribution of values in polymers, the discrete *o*-Ps lifetime obtained using the PATFIT88 processing system actually represents a mean value. Assuming that the free volume holes are spherical, average free volume hole size of the networks can be calculated as $< V_h >= (\frac{4}{3})\pi R^3$.

Prior to PALS experiment, the sample was equilibrated for 24-72 hours in the corresponding water vapor environment by placing the sample discs in appropriate RH chambers. The equilibrated sample (along with the source) was then placed in the PALS humidity chamber. An automated technique was devised to accurately maintain the required RH in the chamber via a constant influx of nitrogen gas bubbled through DI H_2O (wet N_2) into the chamber, as shown in Figure 2.5. Relative humidity is monitored at the gas outflux from the chamber by a humidity sensor. If the RH value goes beyond the set value, the humidity controller (which is connected to the humidity sensor) activates the solenoid valve, which then lets dry nitrogen into the chamber. The dry nitrogen then lowers the RH% within the chamber and once the RH% goes below the set value the humidity controller turns off the solenoid valve thereby stopping the influx of dry nitrogen, and the cycle continues. This automated dynamic technique accurately

maintained any RH% value between 0-80% range. For tests at RH greater than 80%, a sponge containing saturated salt solution or DI water was placed inside completely enclosed and sealed PALS sample chamber. For RH values of 85% and 99%, sponge contained saturated potassium chloride solution and DI water respectively.

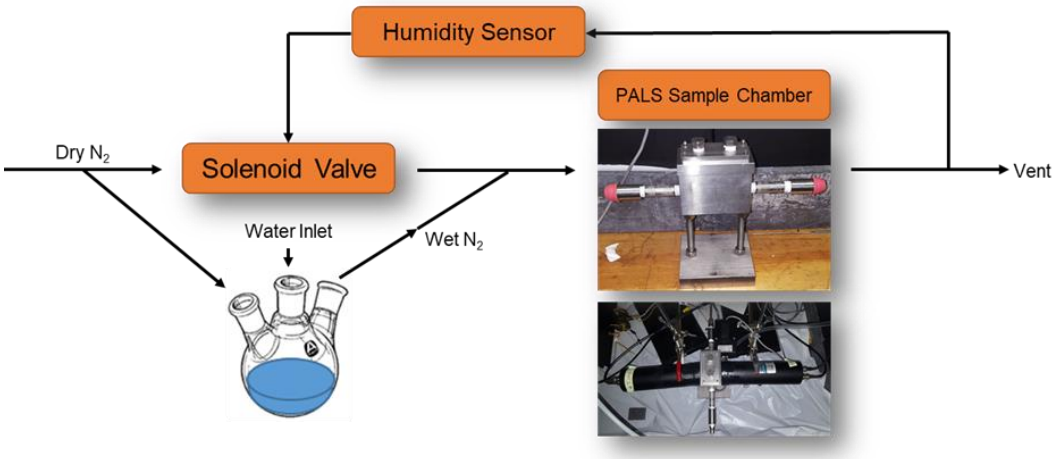

Figure 2.5 Schematic illustrating the RH-PALS apparatus setup.

2.2.9 Raman Microscopy of Pigmented Coatings.

Raman spectroscopy was carried out using a Thermo Scientific™ DXR Raman Microscope system. Specimens were illuminated through either a 50x/0.75 or 50x/0.5 objective with a 633 nm excitation from a He-Ne laser source. The incident power source ranged from 5-7 mW and resulted in a spot size of 0.8 µm with 3-4 µm spacing intervals between each map point. Single point spectra were collected between 3350-50 cm^{-1} while mapping studies were collected between 3200-100 cm^{-1} and averaged over 64 or 32 scans, respectively, with a spectral wavelength resolution of 1 cm^{-1}. Collection times for mapping studies were approximately 30 seconds per spectrum/point and for all samples an auto-fluorescence correction factor (5th order polynomial) was applied to

collected data. Maps of both scribed and non-scribed regions of coatings were collected over an area of approximately 1.0 x 10^4 μm^2, an example of which can be seen in Figure 6.4.

2.3 References

1. Pramanik, M.; Fowler, E. W.; Rawlins, J. W., Another look at epoxy thermosets correlating structure with mechanical properties. *Polym. Eng. Sci.* **2014**, 54, 1990-2004.
2. Nazarenko, S.; Meneghetti, P.; Julmon, P.; Olson, B. G.; Qutubuddin, S., Gas barrier of polystyrene montmorillonite clay nanocomposites: effect of mineral layer aggregation. *J. Polym. Sci., Part B: Polym. Phys.* **2007**, 45, 1733-1753.
3. Fieldson, G. T.; Barbari, T. A., The use of attenuated total reflection FTIR spectroscopy to characterize penetrant diffusion in polymers. *Polymer* **1993**, 34, 1146-53.
4. Cotugno, S.; Larobina, D.; Mensitieri, G.; Musto, P.; Ragosta, G., A novel spectroscopic approach to investigate transport processes in polymers: the case of water-epoxy system. *Polymer* **2001**, 42, 6431-6438.
5. Tao, S. J., Positronium annihilation in molecular substances. *J. Chem. Phys.* **1972**, 56, 5499-510.

CHAPTER III - FREE VOLUME INFLUENCE ON MOISTURE SORPTION AND INFLUENCE OVER MACROSCOPIC PROPERTIES

3.1 Introduction

Organic coatings implemented in the pursuit of corrosion protection require, fundamentally, adhesion to the substrate and barrier properties sufficient to reduce or prevent the ingress of corrosive species (water, oxygen, and electrolytes) in quantities sufficient to initiate or sustain corrosive degradation.[1] Epoxy-amine networks, along with other crosslinked polymer chemistries, are an often employed source of the matrix or binder material for the primer or intermediate coating layers tasked with helping to prevent corrosion at the metal substrate. Despite a number of beneficial material characteristics, including high hardness, adhesion, and chemical resistance, the hydrogen bonding capability and polar nature of epoxy-amine matrices lends to an inherent tendency to take on moisture, with reported maximum water quantities varying between 1-7 wt% (equilibrium water content – EWC).[2,3,4] The mechanism of moisture sorption and diffusion has been studied extensively to clarify how epoxy-amine network structural and compositional features influence water transport, although the full extent of the relationship between polymer features (free volume, polar group concentration, crosslink density, etc.) and water interaction and transport is incomplete.[5-7] Furthermore, how these characteristics carry over to impact fully formulated coatings containing various solvents, pigments, fillers, and additives in addition to the matrix component is as yet not entirely understood.[8,9]

Positron annihilation lifetime spectroscopy (PALS) has been demonstrated as a powerful and versatile means of evaluating the nano-scale free volume properties of

polymers, including those incorporated into coatings used in corrosion protection roles. Macqueen and co-workers implemented PALS for probing free volume characteristics of epoxy-amine networks based on BPA and glycol ether-based epoxy resins in both dry and H_2O-saturated states. Inconsistency in the correlations between the free volume fractions or hole sizes and the saturation water content and EIS-determined corrosion protection suggested that other factors, including polymer swelling and solvent interaction, determine the shift in material properties in conjunction with free volume traits under variable exposure conditions.[10] Similarly, Madani and co-workers utilized mixtures of the same epoxy resins crosslinked with a polyamide hardener and PALS testing to demonstrate a relationship between free volume fraction and water saturation content while also suggesting that more flexible and hydrophilic matrices are more likely to experience growth in free volume hole size with the ingress of water. It was also determined that the inclusion of borate or silicate inhibitor pigment had no effect on water sorption behavior of DGEBA-based networks but resulted in increased free volume cavity volumes in glycol ether epoxy-amide matrices.[11] However, in these analyses the ability to maintain a controlled relative humidity or water saturation state over the entire PALS measurement period could not be ensured and as such it is possible that the physical state of the samples driven by environmental severity differences shifted during testing.

Additional investigations of epoxy-amine network free volume characteristics have yielded valuable insight into how polymer microstructural features determine transport properties of small molecule penetrants in addition to water. Jackson and co-workers created a model network series consisting of DGEBA, DGEBF, or TGDDM

epoxy resins crosslinked with diaminodiphenyl sulfone isomers and subjected samples to immersion in water or organic solvents of varying van der Waals volumes (18 – 88 $Å^3$). Gravimetric sorption results were compared with PALS measurements of dry samples to determine that as solvent molecular size approached the measured epoxy-amine network free volume values (59 – 82 $Å^3$) the diffusion kinetics slowed or even halted, indicating that free volume sizes and ratios alone could potentially prevent the ingress of penetrant.[12] However, the absence of a direct linear relationship between solvent sorption quantity and permeant volume for each network indicated that additional polymer features (segmental mobility, secondary interactions) also influenced transport. Frank and co-workers studied a series of networks composed of stoichiometric mixtures of di-, tri-, and tetra-functional epoxy resins crosslinked with a single diamine and correlated the resulting H_2O and MEK transport properties with free volume characteristics. It was observed that increasing the proportion of higher functionality monomer resulted in higher crosslink densities and higher free volume fractions while also lowering the average free volume hole size, $<V_h>$. This had the result of increasing the total amount of solvent within the polymer at saturation but decreasing the kinetics of sorption.[13] Lange and co-workers investigated the extent to which polymer physical and chemical characteristics influenced oxygen transport in more than 15 different epoxy-amine combinations and found significant decreases in O_2 permeability as hydrogen bonding and polar group concentration increased but very little to no correlation between T_g and transmission rates although free volume properties were not investigated.[14]

Few investigations have reported the impact of hydroplasticization and the presence of moisture on polymer free volume properties and the resulting shifts in

transport behaviors. Muramatsu and co-workers subjected an ethylene-vinyl alcohol copolymer to increasing relative humidity levels at room temperature and noted a U-shaped decrease then increase in free volume hole size (between 0-95% RH) which corresponded with a similar pattern in oxygen permeability. It was suggested that these trends were the result of water molecules filling free volume pores between 0-30% RH which then induced plasticization and allowed for the increased measured volumes at higher water vapor concentrations.[15] Similar findings were presented by Dlubek and co-workers who subjected Polyamide 6 to varying relative humidity environments and employed PALS to observe an approximately 12% drop in free volume hole size from the dry glassy state to 45% RH followed by an increase to previous values as higher moisture content ranges (> 90% RH) were reached. The authors posited that in addition to simply filling free volume holes the water molecules participated in varying degrees of interaction with the polymer, the extent of which was dependent upon H_2O molar concentration, which resulted in fluctuating degrees of plasticization.[16] Mo and co-workers monitored oxygen and water vapor transmission rates as a function of relative humidity in hydrophilic (polyvinyl alcohol, PVA) and hydrophobic (polypropylene, PP) films and found that the water-soluble PVA exhibited exponential increases in both oxygen and water vapor transport rates as RH increased from 35 to 90%. In contrast, the PP samples exhibited a slight linear increase in water vapor transmission and decrease in oxygen transport over the same range.[17] The differences in response to water vapor concentration indicate that polymer solubility plays a central role in determining both the interaction between matrix and water and the extent to which free volume-directed transport properties are affected.

Extensive investigations of epoxy-amine free volume and topological properties suggest that although these features influence aspects of water, salt, and oxygen sorption and transport behaviors, they act in tandem with other polymer characteristics such as segmental mobility and secondary interactions associated with polar and hydrogen bonding groups.[5-7] However, a comprehensive analysis and explanation of shifts in network free volume properties following uptake of moisture or as a function of water content is not presently available. Given the dynamic nature of polymer free volume hole size and fraction characteristics it is necessary to elucidate these changes as corrosion protection coatings are likely to experience a range of exposure conditions. The following investigation was designed to provide a range of humidity level challenges to a series of epoxy-amine networks which vary in dry or unexposed free volume conditions and observe the resulting impact on transport and thermomechanical properties.

3.2 Experimental

3.2.1 Methodology

A series of five different model epoxy-amine networks were formulated using either E825 or E1510 epoxy resins and combined with one of five different crosslinking agents: EDR148, DDM, DDS, THF100, or ED900, the chemical structures of which are given in Figure 3.1. These matrices provided a means of evaluating glasses that vary in T_g along with a comparison of two rubbery networks that reflect very different extents of water sorption. In addition to these model epoxy-amine networks, a fully formulated coating was selected for comparison in select analyses. Deft® 02GN084, supplied by PPG Aerospace Products, is a two-component solvent-borne non-chrome epoxy polyamide primer (classified as a MIL-PRF-23377K Type I Class N primer) containing a

praseodymium oxide-type corrosion inhibitor. A number of analytical techniques were implemented in evaluating the transport properties as a function of free volume properties using RH-DMA, RH-PALS, and others.

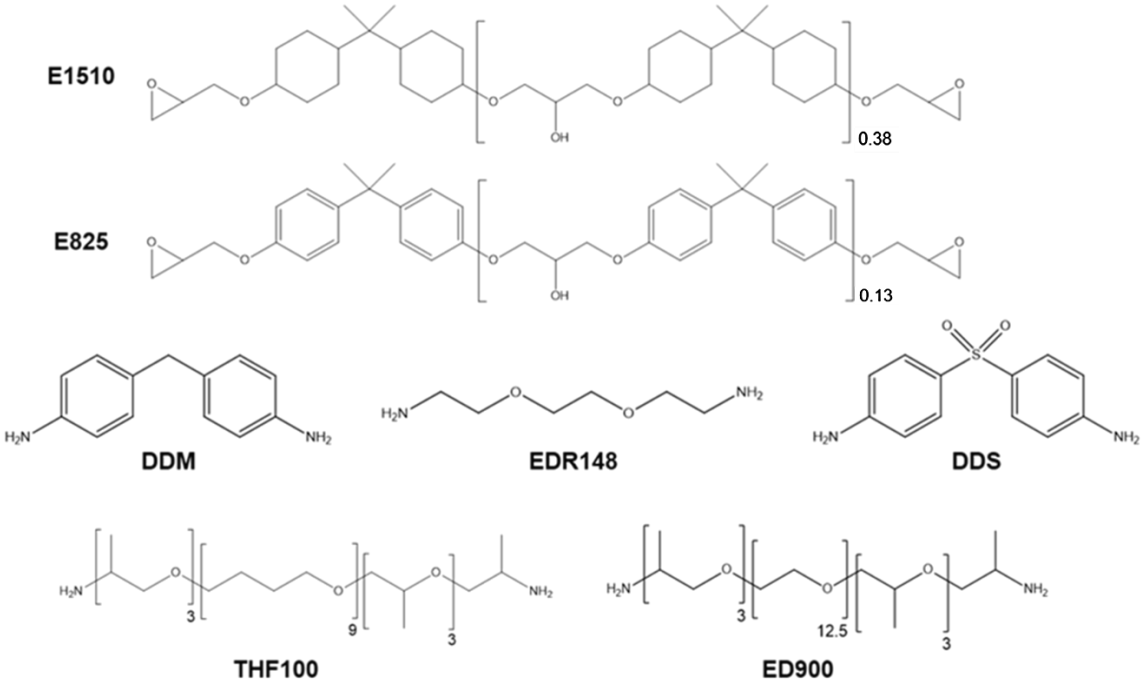

Figure 3.1 Chemical structures of epoxy-amine network monomers.

3.3 Results and Discussion

3.3.1 Thermomechanical Properties of Cured Epoxy-Amine Networks.

Following the cure of epoxy-amine samples, DMA revealed a broad range of T_g values, as interpreted from the maxima of tan δ peaks. Three of the networks exhibited increasing glassy values (at room temperature): 60.56 °C (E1510-EDR148), 135.75 °C (E1510-DDM), and 226.67 °C (E825-DDS) while the two remaining networks revealed sub-ambient values at -8.26 °C (E1510-THF100) and -11.24 °C (E1510-ED900), as shown in Figure 3.2.

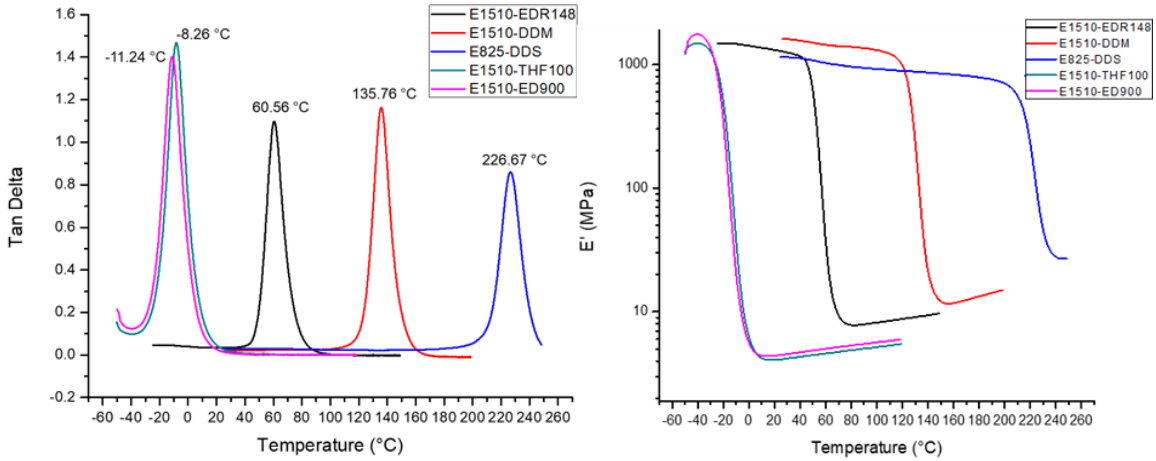

Figure 3.2 DMA thermographs of cured Chapter III epoxy-amine networks.

Tan Delta (tan δ, left) and Storage Modulus (E′, right) and of the matrices through their glass transitions.

These five epoxy-amine networks present a wide range of viscoelastic states at room temperature conditions with T_gs ranging across a nearly 235 °C span and E′ values between 4 MPa and 1.6 GPa at room temperature (approximately 25 °C). The tan δ peaks of all networks reveal uniform Gaussian peaks indicating the complete cure of each epoxy-amine mixture. The two polymers with the lowest T_g values, E1510-THF100 and E1510-ED900, offer the opportunity to evaluate and compare two different epoxy-amine rubbers of similar T_g and network architecture (given the similarity of monomer molecular structure and equivalent weight) that should exhibit very different hydrophilic character due to the difference in the backbone composition that makes up the majority of the polyether component: polytetramethylene oxide (THF100) and polyethylene oxide (ED900), which are known to exhibit moderately hydrophobic and hydrophilic properties, respectively. The three glassy networks (E1510-EDR148, E1510-DDM, and E825-DDS) were selected for comparison primarily for the nearly equivalent separation

in glass transition temperatures (70-90 °C between each network) and not for variability in solubility/hydrophilicity, crosslink density, or chemical composition.

3.3.2 Moisture Sorption of Epoxy-Amine Networks at Different RH Levels

DVS was implemented in determining the kinetics and equilibrium water vapor sorption or saturation limits the various cure thermoset systems at relative humidity limits mirroring those used in RH-PALS testing, specifically, 5, 22, 44, 57, 75, and 95% RH, although some formulations were only subjected to only the upper, middle, and lower RH levels. Sample discs 6.3 mm in diameter and thicknesses ranging from 250 to 300 μm were suspended in a quartz sample pan and subjected to a drying protocol at 60 °C and 0% RH for 60-120 minutes (until a change in mass subsided) then the appropriate moisture sorption levels were applied. Figure 3.3 illustrates the water vapor sorption profiles of the dried epoxy-amine networks at varying RH levels.

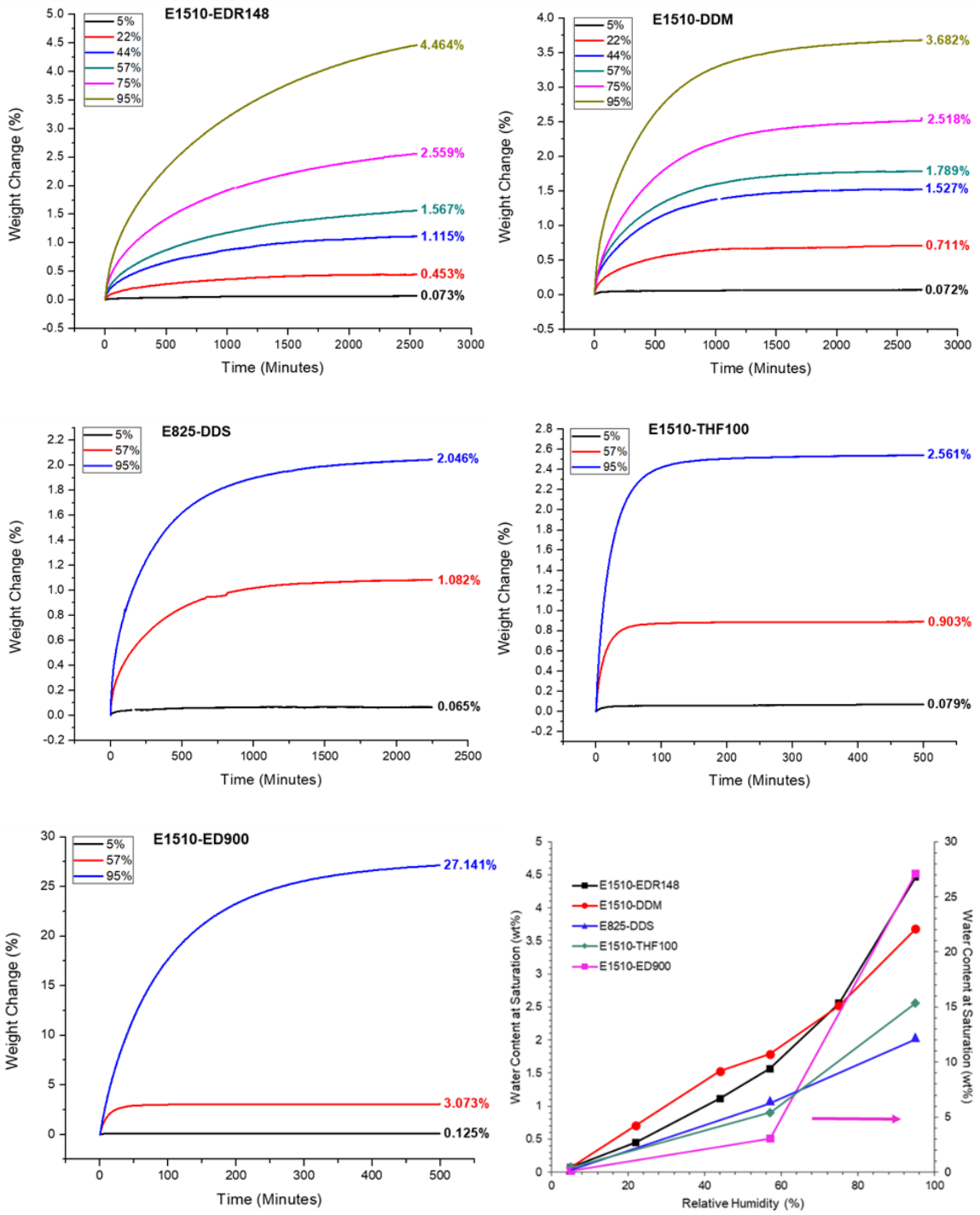

Figure 3.3 Water vapor sorption profiles of each epoxy-amine network and comparison of the water saturation quantities as a function of relative humidity.

What is evident from the DVS plots is the variability in sorption characteristics between the epoxy-amine networks. The glassy polymers take on increasing quantities of moisture with decreasing T_g (E1510-EDR148 > E1510-DDM > E825-DDS, at 95% RH) although the exact extent to which composition and concentration of hydrophilic functional groups is not immediately obvious. The rubbery networks exhibit faster uptake rates, as is evident in Figure 3.4, whereby the samples with sub-ambient T_g values exhibit significantly higher initial moisture uptake slopes and reach near-equilibrium levels within 500 minutes of exposure. At low water vapor all networks except for the hydrophilic rubber take on similar quantities of moisture (between 0.065 and 0.079 wt%) while at higher relative humidity levels the difference in sorption properties becomes more apparent with water content at saturation ranging from 0.903 to 1.789 wt% (and 3.073 wt% for E1510-ED900) at 57% RH. The E1510-ED900 demonstrates a substantially higher hydrophilicity, with a maximum water content in excess of 27 wt% at 95% RH, in contrast to the 2.046 to 4.464 wt% found with the other samples. Additionally, it can be seen that the E1510-EDR148 epoxy-amine network requires more time to reach equilibrium levels of water vapor content than the other glassy samples.

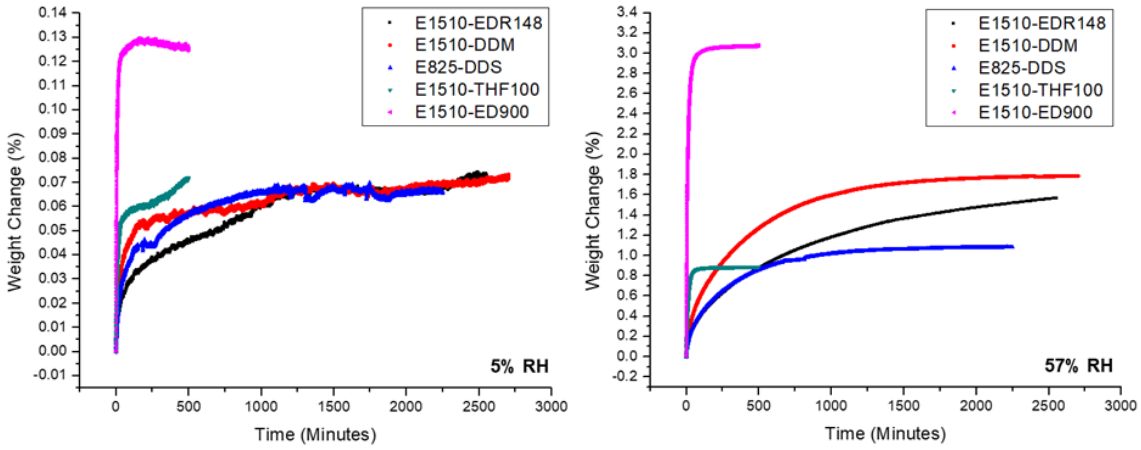

Figure 3.4 Water vapor sorption profile comparison of the epoxy-amine matrices at 5% (left) and 57% RH (right).

A wide array of epoxy-amine diffusion kinetics have been reported, with both Fickian (Case I) and non-Fickian characteristics (for example anomalous[21,22] or dual-mode sorption[23] mechanisms), with some apparent dependency on the exact combination of resin and curing agent, T_g and/or testing temperature, stoichiometry, degree of cure, solvent content, etc. However, to easily estimate the variability in water vapor sorption kinetics, all were treated as Fickian in nature, in which case the water uptake and diffusion process can be described via the Fickian diffusion solution[24] as:

$$\frac{M_t}{M_\infty} = 1 - \frac{8}{\pi^2}\sum_{k\ odd}\frac{e^{-tD\left(\frac{k\pi}{l}\right)^2}}{k^2} \cong 1 - exp\left[-7.3\left(\frac{Dt}{l^2}\right)^{0.75}\right]$$

wherein D is the diffusion coefficient, M_t is the moisture content at time t, M_∞ is the moisture content at saturation, and l is the sample thickness. This can then be simplified at early stages[25] to:

$$\frac{M_t}{M_\infty} = \frac{4}{\pi^{1/2}}\left(\frac{Dt}{l^2}\right)^{1/2}$$

When M_t/M_∞ is plotted as a function of $t^{1/2}/l$ the initial slope (usually when $M_t/M_\infty < 0.5$), or I, is related to D by:

$$D = I^2\left(\frac{\pi}{16}\right)$$

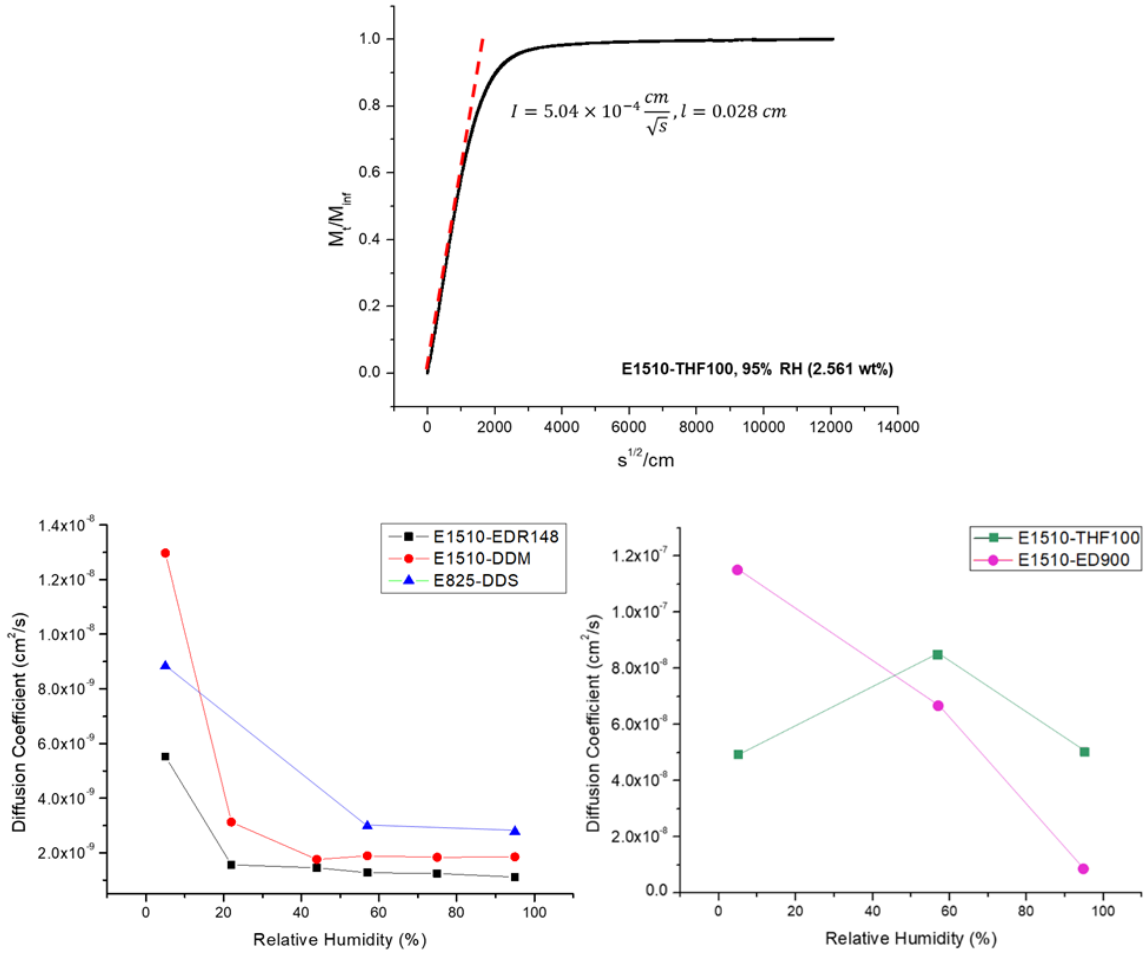

Figure 3.5 Demonstration of diffusion coefficient, *D*, calculation for DVS sorption process of E1510-THF100 sample at 95% RH (top), and *D* as a function of relative humidity for glass (bottom left) and rubber (bottom right) samples.

Applying this method (Figure 3.5) to the DVS isotherms resulted in calculated diffusion coefficients that predictably varied between the networks[24] with higher diffusivity ranges (8.55×10^{-9} to 1.15×10^{-7} cm^2/s) for rubbery epoxy-amine samples, regardless of saturation quantity, compared to glassy networks (1.12×10^{-9} to 1.3×10^{-8} cm^2/s). It is also apparent that glassy network diffusion coefficients exhibit little to no dependency on relative humidity level beyond 5% RH. However, given the lower signal-to-noise ratio of the measured masses when operating near the lower limits of the DVS instrument it is possible that these values (< 20% RH) may be inflated. The diffusion coefficient of the hydrophilic low T_g epoxy-amine network, E1510-ED900, demonstrates the greatest dependency on RH level with a near linear decrease in diffusivity as environmental moisture concentration increases.

3.3.3 Free Volume Properties at Different RH Levels

The use of a relative humidity-controlled apparatus combined with positron annihilation lifetime spectroscopy (PALS) allowed for probing of the epoxy-amine network free volume characteristics at various points of moisture exposure without risking any loss of water during testing. Samples were held at different relative humidity levels in chambers equilibrated using saturated salt solutions until an anticipated equilibrium saturation level was reached within each epoxy-amine network, for a period of time determined by DVS. These samples were then transferred and subjected to PALS testing and the influence of water at specific levels of exposure concentrations that were maintained throughout the course of the measurement. As seen in Figure 3.6 the glassy and rubbery epoxy-amine networks exhibit distinct ranges of measured free volume hole sizes across the entire range of relative humidity levels, with the two rubbery samples

yielding sizes ranging from 140-150 $Å^3$ and glasses bearing values between 60-90 $Å^3$. This separation between networks based on T_g is predicted by classical polymer free volume theory but an additional dissimilarity between the two groups is the presence of an RH-dependent increase or decrease in free volume size that is not present in the rubbery samples. All three glassy networks reveal decreasing pore volume between 0-75% RH and increasing or rebounding values at higher RH levels (75-100%). Due to the interaction between positrons and water leading to annihilation it is assumed that the decreasing trend in sizes observed at lower relative humidity levels is due to the filling of free volume holes at lower sorption levels. As moisture levels are increased the number and extent to which pores are filled with water molecules increases until approximately 70-80% RH is reached at which point large scale swelling occurs allowing for substantially increased polymer chain mobility. This swelling results in larger voids forming throughout the sample which further expand upon increasing humidity levels. When comparing these data to DVS results it is apparent that this shifting in free volume hole sizes does not have a direct impact on the kinetics of water diffusion (Figure 3.5) nor do the saturation quantities reveal a shift in uptake behaviors within the same range (70-80% RH). However, it could be expected that at longer times the increase in average free volume hole size would allow for additional ingress of water.

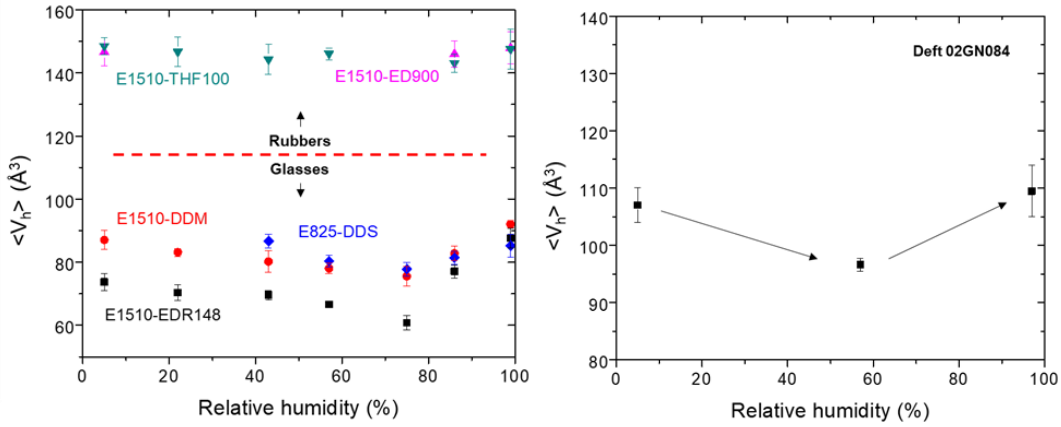

Figure 3.6 Average free volume hole size as a function of relative humidity level for glassy and rubbery epoxy-amine network samples (left) and a commercial CRI-containing pigmented epoxy primer (left).

A free film of a CRI-pigmented epoxy-amine primer, Deft 02GN084 ($T_g \approx 85$ °C), was subjected to the same testing protocol and a similar pattern in free volume average hole size decrease from lower to mid-range relative humidity followed by a subsequent increase at higher levels was observed. This demonstrates that the effect of shifting polymer properties is not hindered via the addition of pigments, solvents, or additives and could be expected to occur throughout the service lifetime of a coating subjected to variable humidity or precipitation conditions (e.g., any exterior corrosion protection coating). Inevitably, fluctuating water transport behaviors will directly influence the sorption and permeation of other penetrants central to corrosion protection performance, specifically, oxygen and ions (including inhibitors) by occupying to varying degrees what is ostensibly the primary, or most accessible, pathways for diffusion to the substrate.

3.3.4 Water Vapor and Oxygen Transmission Analysis

Two glassy epoxy-amine networks, E1510-EDR148 (T_g = 60.56 °C) and E1510-DDM (T_g = 135.76 °C), were selected for additional investigation regarding transport of both water and oxygen through epoxy-amine network samples under varying relative humidity conditions. Free films were subjected to specific relative moisture concentrations (43, 58, 73, 83, and 99% RH) in humidity chambers until a sorption saturation point was attained, as determined via DVS. These samples were then secured in pre-weighed PTFE cups filled with DI H_2O and placed back into the humidity chambers with periodic measurements of weight according to ASTM E-96. From this the respective transmission and permeability were calculated, as illustrated in Figure 3.7. It is apparent from these data that a shift in transport rates occurs at approximately 75% RH whereby exposure to higher relative humidity conditions results in higher rates of permeation. This coincides with the steep increase in measured free volume hole size observed in the RH-PALS experiments at higher relative humidity levels. It is likely that a threshold is reached wherein a sufficient moisture concentration is reached for swelling to occur due to increases in polymer segment or chain mobility which results in growth of pore volume and an escalation in water permeability.

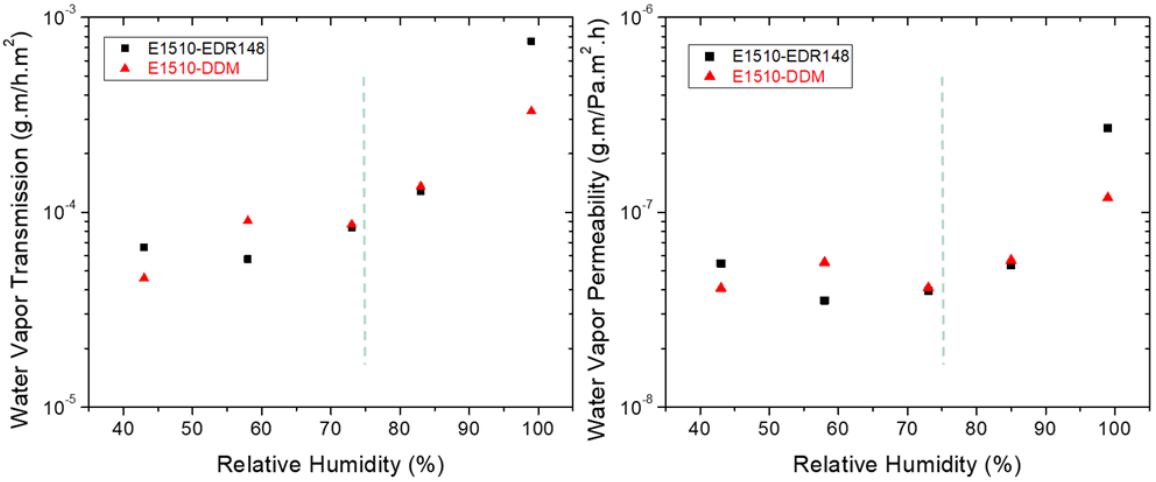

Figure 3.7 Measured water vapor transmission (right) and calculated permeability (left) through epoxy-amine networks E1510-EDR148 and E1510-DDM.

Additionally, the transmission of oxygen is influenced by the presence and concentration of H_2O within epoxy-amine networks. As water molecules occupy the empty physical spaces and interact with polar and hydrogen bonding sites accessible to penetrants following sorption, it could be anticipated that competition for space availability within the polymer could limit the ingress or transmission of additional penetrants. Figure 3.8 illustrates the effect of the presence of moisture on O_2 transport behaviors within the epoxy-amine network E1510-DDM and the resulting permeability, diffusivity, and solubility as a function of relative humidity exposure. Free film samples (thicknesses of approximately 0.3 mm) were subjected to oxygen transmission testing using a continuous flow technique in a humidity-controlled instrument following exposure to varying relative humidity environments until moisture saturation levels were reached. It is evident that increasing the concentration of H_2O within the polymer (as much as 2.518 wt% at 75% RH) has the resulting effect of lowering O_2 transmission equilibrium levels.

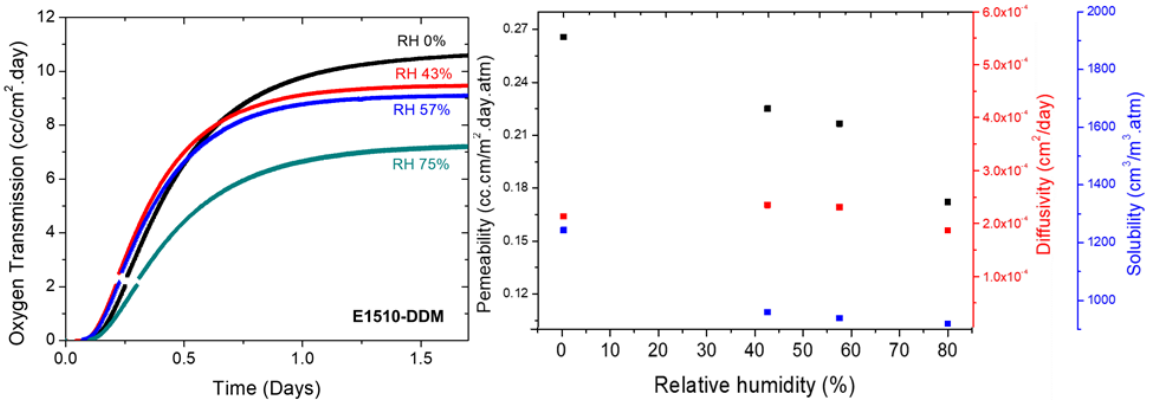

Figure 3.8 Measured oxygen gas transmission rates through glassy E1510-DDM (right) under varying relative humidity levels and the respective calculated permeability, diffusivity, and solubility under those conditions.

From these data the oxygen permeability, diffusivity, and solubility are determined (as these properties are related by $P = D \times S$) and evaluated as a function of relative humidity. Both the permeability and solubility terms drop off in value with increasing moisture content while the diffusivity exhibits a very slight increase and only decreases at the highest measured relative humidity (75%). This indicates that the increasing concentrations of water molecules within polymer free volume holes reduces the transport of oxygen through the samples without having a pronounced impact on the kinetics of diffusion until higher moisture content levels are reached at which point it is expected that swelling of the epoxy-amine network is beginning to occur. Oxygen permeation analysis of E1510-EDR148, shown in Figure 3.9, reveals a fairly dissimilar response to increasing relative humidity. It is seen that this lower T_g network exhibits a lower (approximately halved) flux compared to E1510-DDM under dry conditions and reveals a more pronounced drop in O_2 transmission following the sorption of moisture at lower levels (44 and 64% RH). Furthermore, this system exhibits a slight increase at a

higher relative humidity level indicating that once a higher moisture content is reached (2.559 wt% at 75% RH) either polymer swelling or intensified segmental mobility due to hydroplasticization allows for more extensive oxygen transmission despite the presence of more water within the matrix as compared to previous levels.

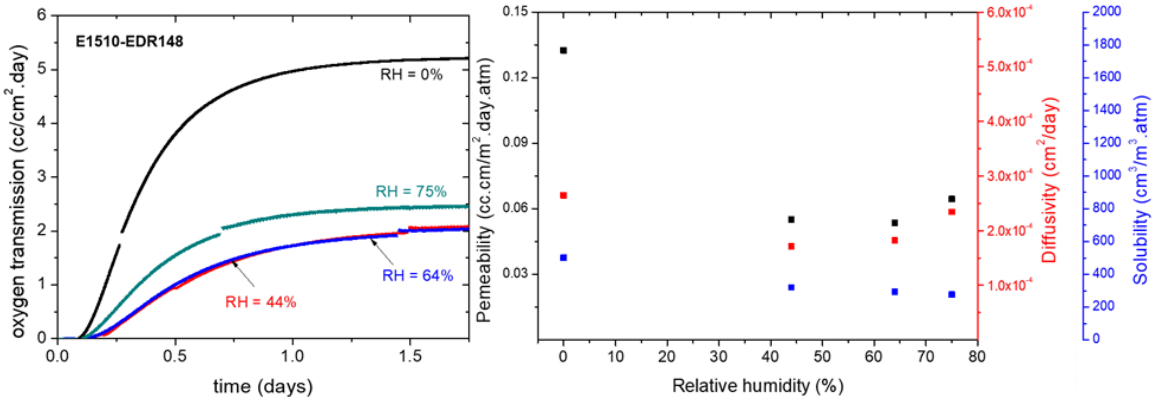

Figure 3.9 Measured oxygen gas transmission rates through glassy E1510-EDR148 (right) under varying relative humidity levels and the respective calculated permeability, diffusivity, and solubility under those conditions.

Comparison of transport terms between the two networks reveals that the O_2 permeability and solubility is generally lower in E1510-EDR148 across all RH levels although both systems exhibit decreases in solubility as moisture levels increase. Permeability is seen to decrease within both matrices across RH levels but the higher T_g network reveals a gradual drop-off while the lower T_g matrix demonstrates a more immediate decrease before increasing slightly at 75% RH. Diffusivity of E1510-DDM increases very slightly from 0 to 57% RH before lowering at higher levels while E1510-EDR148 mirrors the permeability term with increasing moisture content.

The saturation water content at various water vapor concentrations as measured by DVS (Figure 3.5) indicates that these systems take on comparable quantities of H_2O

although oxygen transmission analysis suggests differing extents of interaction between water and polymer, which impacts O_2 permeation. Accounting for the variability in oxygen transport properties of the two matrices requires examination of both structural and compositional features, primarily the chemical composition and free volume properties. The higher T_g network maintains a higher average free volume hole size at all tested RH levels (0-75%) while the E1510-EDR148 consists of a higher concentration of polar and hydrogen bond-accepting ether groups which also contribute to a lower molecular rigidity than the diphenyl methane groups in E1510-DDM. These combined features likely determine the extent to which polymer segmental mobility is impacted following sorption of water. Larger free volume hole sizes result in greater oxygen flux regardless of water content (within the tested range) but the potential for H_2O molecules to interrupt intramolecular hydrogen bonding should enhance molecular chain mobility dynamics to the effect of a relative increase in oxygen. In the E1510-EDR148 system this translates into a slight increase in oxygen permeability at higher water concentrations while E1510-DDM reveals a decrease across the entire water vapor concentration range.

3.3.5 RH-DMA of E1510-EDR148

To further evaluate how epoxy-amine network physical properties shifted relative to sorption at low degrees of water vapor exposure, RH-DMA was carried out on samples of E1510-EDR148 at numerous RH levels similar to those implemented in RH-PALS and DVS testing. Sample free films were installed into the RH-DMA tensile clamp, and the testing was initiated with an equilibration step at 35 °C and the appropriate relative humidity level. The samples were exposed, unstrained, to the moisture atmosphere for 200-400 minutes before starting the normal RH-DMA temperature ramp. Figure 3.10

reveals the depression in E′, E″, and tan δ with increasing discrete moisture sorption levels. As expected the maxima of both E″ and tan δ peaks shift to roughly 15 °C lower temperatures as does the E′ transition onset as hydroplasticization occurs. In addition, the E′ signals reveal the development of a peak shoulder in samples at 50% RH and increases with exposure to higher moisture concentrations which suggests that some degree of network heterogeneity appears due to the development of spatial distributions of more and less solvated or swollen regions of the epoxy-amine matrix.

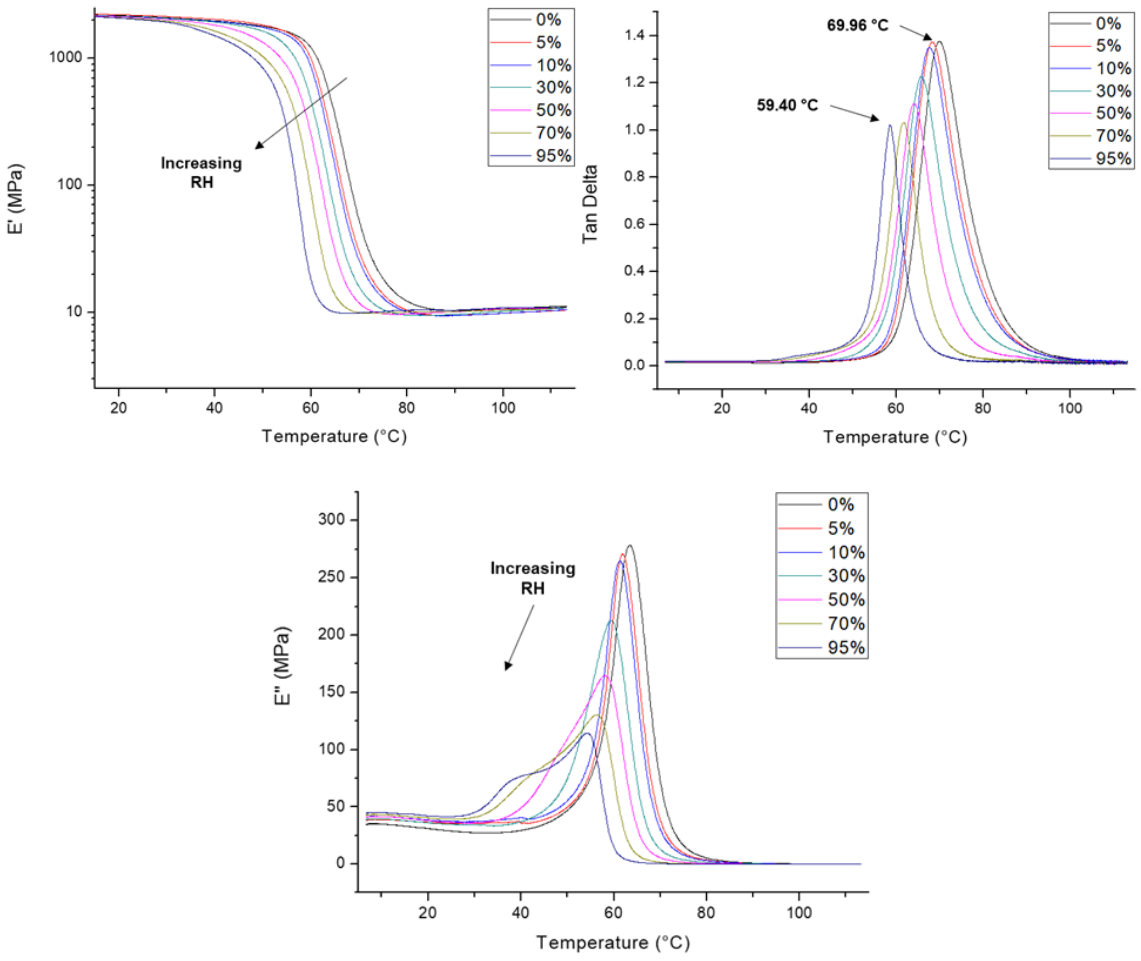

Figure 3.10 Storage Modulus, Tan Delta, and Loss Modulus plots of E1510-EDR148 relative to exposure to various relative humidity levels.

DVS isotherm plots were used to estimate the approximate moisture concentration during testing, assuming minimal loss due to high temperature at later stages during the test. The resulting impact of the presence of water on the glass transition temperature was assessed by comparing observed hydroplasticized T_g values, determined from tan δ peak maxima, at various RH levels with the T_g depression predicted via the Fox Equation which is given by:

$$\frac{1}{T_{g^{total}}} = \frac{wt_1}{T_{g^1}} + \frac{wt_2}{T_{g^2}}$$

In this instance wt_1/wt_2 and T_{g1}/T_{g2} represent the weight fractions and T_gs (K), respectively, of the individual components and T_g^{total} represents the composite T_g of the whole system.[26] This model has traditionally been used to predict the glass transition temperature of polymer blends although it has also been implemented in describing polymer-solvent systems, including hydroplasticized polymers whereby the T_g of water was assumed to be -137 °C.27 Figure 3.11 demonstrates the shift in E1510-EDR148 T_g as water is absorbed and the deviation from predicted values. It can be seen that the presence of even small quantities of moisture depresses the polymer T_g but the experimentally determined hydroplasticized figures are lower than what is predicted by the Fox Equation, which could be due to a number of factors. Although the prediction method assumes a completely homogenized mixture of components, heterogeneous uptake of water by epoxy-amine networks is known to occur due to inhomogeneous distributions microstructural features such as free volume pores and polar group concentrations.[28]

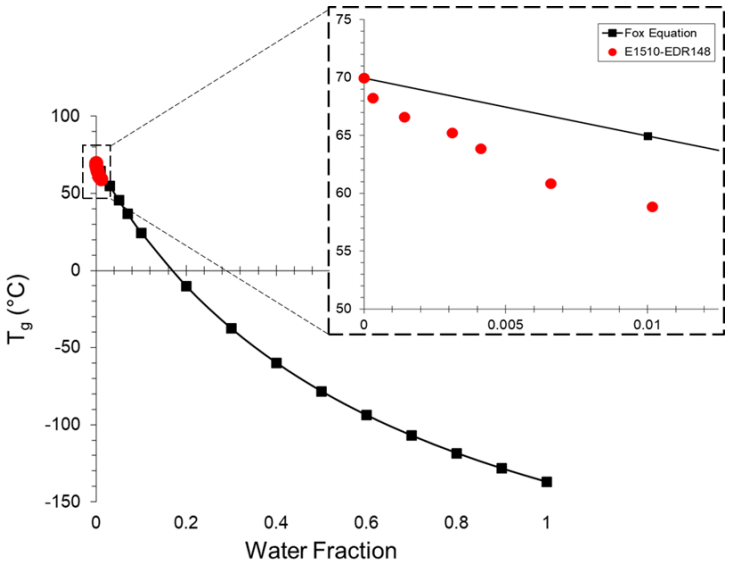

Figure 3.11 Comparison of hydroplasticized T_g values of E1510-EDR148 as measured in RH-DMA and the T_g depression estimated by the Fox Equation.

Additionally, sub-ambient DMA was carried out on samples (rectangular bars with dimensions of 10 x 5 x 1 mm) of E1510-EDR148 immersed in room temperature DI H_2O for 0, 24, and 72 hours to examine the shift in segmental relaxation properties with increasing concentrations of absorbed water prior to saturation. Various secondary transitions in amine-cured epoxy resins have been investigated through numerous studies and correlated with methylene unit trans-gauche isomerization and aromatic ring π flips[29] in addition to camshaft-like rotations of hydroxypropyl ether segments[30] which, as part of the highly polar and hydrogen bonding portion of the polymer network, is purported to contribute a significant role in the water transport mechanism.[6] Figure 3.12 exhibits the change in the β relaxation, with peak maxima centered around -50 °C, with increasing water uptake. Both the tan δ and loss modulus signals reveal an increase in peak heights from 0 to 24 hours followed by a decrease to the lowest values at 72 hours. Although the

peaks are relatively broad, the maximum values also shift slightly to higher temperatures from -48.05 to -41.50 °C following initial immersion then a decrease to the lowest level at -48.68 °C with subsequent water sorption while the peaks broaden and a slight shoulder appears on the lower temperature side, indicating some degree of increase in network heterogeneity. These trends indicate that lower concentrations of water limit the extent of segmental mobility of these hydrophilic units compared to the dry or pristine network before increasing this degree of movement at higher sorption limits, which may coincide with the onset of larger-scale swelling.

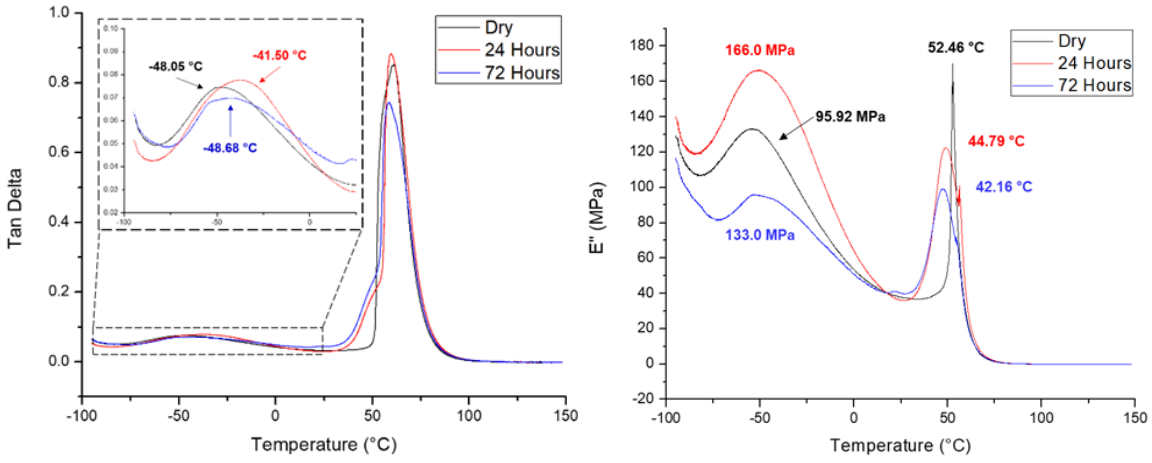

Figure 3.12 DMA thermographs (Tan Delta, left, and Loss Modulus, right) of E1510-EDR148 bulk samples following immersion in DI H_2O at room temperature for 0, 24, and 72 hours.

3.3.6 Volume and Density Analysis of Bulk Samples

In order to further understand how polymer free volume characteristics shift during moisture sorption and the resulting influence on other material properties a macro-scale volume analysis of epoxy-amine network E1510-EDR148 was carried out. Rectangular bulk samples with dimensions of approximately 15 x 12.7 x 6 mm were

prepared and their dimensions were measured with a digital caliper measuring tool while their masses and densities were measured on a Mettler Toledo XS104 analytical balance. All samples were conditioned beforehand in an oven at 85 °C for several hours then placed in a desiccator for several days to remove as much moisture from within the polymer as possible without causing any thermal degradation. These were then placed in humidity chambers at either 43, 57, 75, 83, or 99% RH and removed, patted dry with paper towels, and weighed/measured after several months to allow for samples to reach saturation equilibrium in the respective water vapor environments. Figure 3.13 compares the shifts in nano- and macro-scale volume properties of this epoxy-amine network as a function of relative humidity. It is seen that the volume and density of bulk samples increase across the tested RH range in contrast to the free volume hole size which exhibits a discontinuity around ~75% RH as discussed previously. This indicates that water sorption-induced swelling occurs in distinct stages depending on the size scale observed: as moisture ingress occurs within the network free volume pores are filled until a concentration is reached whereupon hydroplasticization allows for sufficient polymer segment mobility such that these holes can significantly increase in size. However, large-scale bulk sample volume reveals an increase even at low RH levels but does express a more substantial surge within the same high moisture content range. A similar trend is found with the sample density which increases steadily through the tested RH range.

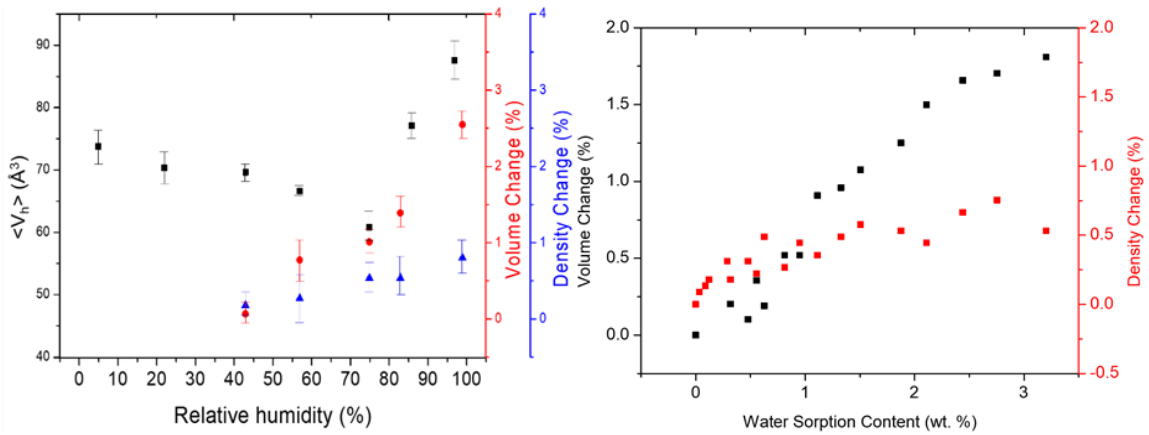

Figure 3.13 Comparison of free volume hole size and macro-scale sample volume and density shift with increasing relative humidity (left) and shifts in volume and density of bulk samples immersed in DI H_2O (left) of epoxy-amine network E1510-EDR148 samples.

Bulk samples of E1510-EDR148 were also subjected to exposure to liquid water by immersing in DI H_2O with periodic measurement of mass, density, and physical dimensions. As seen in Figure 3.13 both volume and density are found to increase throughout the entire sorption process prior to reaching equilibrium or saturation. This further demonstrates that while nano-scale free volume properties of the epoxy-amine network reveals distinct regimes of growth or reduction dependent upon moisture concentration, the macroscopic characteristics respond to the ingress of water unilaterally and immediately.

3.3.7 ATR-IR Evaluation of H_2O-Immersed E1510-EDR148

Free film disc samples of approximately 15 mm in diameter and 0.3 mm thickness were immersed in DI H_2O at room temperature and ATR-IR spectra were collected at 0, 1, 4, and 24 hours. The broad peak centered around 3550 – 3200 cm^{-1} (–OH stretch) was observed and a deconvolution protocol was used to determine the relative peak areas

corresponding to water in different states of hydrogen bonding. These areas were then combined to distinguish "bound" (S_1, S_2', S_2'' or singly, weak and strong doubly hydrogen-bonded) water states from "free" (S_0 or free) molecules, according to the extent of hydrogen bonding between polymer and H_2O.[3, 31]

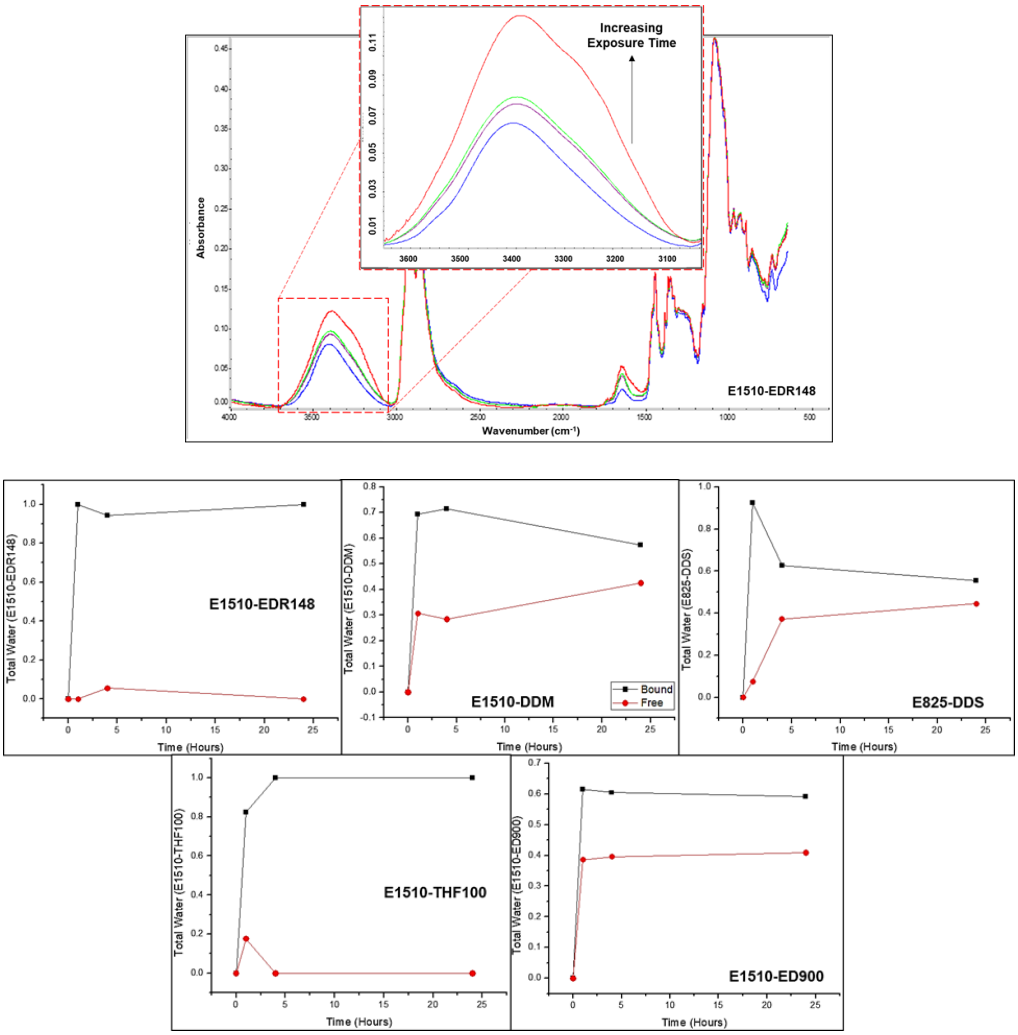

Figure 3.14 ATR-IR overlay of E1510-EDR148 after immersion in DI H_2O and proportions of free (red) versus bound (black) water type populations, as a reflection of the total amount of water present in samples immersed in DI H_2O for 0, 1, 4, and 24 hours.

The resulting groupings as illustrated in Figure 3.14 indicate that at all time points there exists a higher proportion of bound water than free within all formulations. This population includes H_2O molecules that associate with the polymer through only a single hydrogen bond in addition to those that are either loosely or tightly bound to ether, hydroxyl, or tertiary amine moieties within the system. The free water fractions in glassy networks increase across all time points and appear to scale with T_g while the free water fraction of the rubber samples may be primarily dependent upon water content or hydrophilicity. Given the proclivity for polymer free volume hole size at a given temperature to increase with glass transition temperature it is expected that more physical space is available for free water molecules to gather although contributions by network chemical composition must also be considered. These results suggest that increasing free water fractions at longer times in high moisture or liquid water environments may correlate with swelling that is distinct from hydroplasticization (decrease in T_g and modulus) which is detectable even at short times or low moisture content.

3.4 Conclusions

In this collection of experiments a number of interesting trends related to transport properties of both water and oxygen as a function of polymer moisture content in epoxy-amine networks were disclosed. A series of matrices that vary in T_g (a range of nearly 250 °C) were selected for comparison of free volume properties as a function of water sorption and subjected to RH-controlled PALS measurements after samples had equilibrated under a number of humidity conditions. It was noted that each glassy network (T_g > 50 °C) exhibited a water content-dependent reversible shift in free volume hole size that decreased between 0-75% RH and but significantly increased at higher

levels. In contrast, the low T_g systems (rubbery throughout the environmental conditions) demonstrated very little change throughout the entire relative humidity range, regardless of water sorption extent. Although the effect of water on epoxy-amine network properties is evident at low moisture sorption levels (low RH levels or early stages of DI H_2O immersion) the increase in average free volume only takes place at higher levels (≥ 75% RH), suggesting that water molecules first fill the most easily accessible or interconnected free volume voids and act locally on polymer polar or hydrogen bonding segments before a critical water content threshold is reached whereby larger-scale swelling occurs and heightened polymer mobility is possible. However, larger samples were subjected to the same humid environments as well as immersion in DI H_2O and increases in volume and density were found at all exposure levels and times, indicating that although the free volume holes decrease in size between 0-75% RH the macro-scale swelling initiates as soon as water ingress take place. In any case the trend observed in RH-PALS experiments was also reflected by a fully formulated inhibitor-containing epoxy primer which implies that a coating may experience variability in free volume properties due to environmental variability (e.g. diurnal cycle) which could influence barrier properties and therefore corrosion protection.

DVS measurements revealed that although there appeared to be a correlation between T_g and the amount of water absorbed at saturation (> 75% RH), it is more likely to be dependent upon chemical composition than glass transition temperature although the diffusion coefficient of the glasses did appear to scale with T_g which could be explained by the difference in free volume hole size between networks, at least below 95% RH. Rubbery samples exhibited saturation levels and sorption kinetics that are

almost entirely based on differences in polar and hydrogen bonding group concentrations given the similarity in T_g, crosslink density, and free volume hole size. The transport properties of two of the glassy networks, E1510-EDR148 and E1510-DDM, were evaluated further via water vapor permeability testing using the cup method. It was observed that two distinct regimes of permeation rates occurred at RH levels that corresponded with shifts in free volume as measured by RH-PALS. This lends additional credibility to the postulation that below 75% RH the free volume pores are filled by water molecules as polymer moisture content increases before widespread swelling of the microstructure allows for increasing hole size which promotes higher permeability. Oxygen permeability testing yielded results which support this wherein transmission rates were observed to decrease, in general, from 43 to 75% RH despite the lower T_g network demonstrating a slight increase at the higher end of the water vapor range. Although trends in O_2 diffusivity differed between the networks it was revealed that both systems experienced a lowering of polymer-oxygen solubility as water content increased which may be a product of how segmental mobility is modified by the presence of, and interaction with, moisture at varying concentrations.[32]

DMA and RH-DMA of E1510-EDR148 allowed for the examination into the impact of moisture on thermomechanical properties at different concentrations and through these methods it was observed that distinct regimes of hydroplasticization exist. Both the glass transition temperature, given by the tan δ maxima, and glassy storage modulus decrease from higher to lower values from low to high RH, which occurs simultaneously with free volume pore size decrease. The drop in T_g exceeds what is predicted by the Fox Equation which may be due to intramolecular hydrogen bond

interruption following sorption of even small amounts of water. This is supported by shifts in secondary relaxations of E1510-EDR148 following immersion in DI H_2O: early stages of water sorption reveal a decrease in β transition peak height/area as compared to the dry or pristine state before increasing to its highest levels following additional uptake. This would suggest that camshaft rotations of the hydroxypropyl ether segments within the epoxy-amine network are subdued as tightly bound water acts as a hydrogen bonding "bridge" at low water concentrations, then swelling takes place with higher water concentrations which allows for enhanced molecular mobility. ATR-IR analysis of free films following immersion in DI H_2O indicates that the extent to which polymer-water interaction shifts at varying points in the sorption process differs between the epoxy-amine formulations although all systems reveal a surplus of "bound" water at all stages, which would most likely disrupt polymer-polymer secondary interactions.

These results taken in combination reveal a more complete picture of the water sorption mechanism in epoxy-amine networks and demonstrates how the complex interactions between water and polymer shape the shift in thermomechanical properties and oxygen transport processes. The findings indicate that water first traverses the most easily accessible free volume pathways, occupying the empty spaces and acting locally on polymer chains by disrupting a small proportion of hydrogen ponding and initiating hydroplasticization (lowering T_g and E'). As additional water content ingresses, larger-scale swelling occurs such that free volume holes increase and size and allows for additional mobility in polymer chain dynamics as "free" water population size increases. Although this general mode of moisture uptake has been suggested not only for crosslinked epoxy networks but for glassy amorphous polymers in general[33] this work

provides some of the first evidence from the aspect of free volume as a function of water content. Additionally, as RH-PALS testing of an actual formulated corrosion protection primer revealed similar results to the model networks it is possible that these examinations could be applied or extended to the process of coating formulating to influence water transport and hence barrier properties. Based on these results it is hypothesized that coatings systems which absorb higher quantities of moisture allow for less permeation of oxygen to the substrate with greater extent of water-polymer interaction resulting in slower O_2 diffusion rates which would potentially decrease the rates of corrosion initiation and propagation.

3.5 References

1. Wicks, Z. W., Jr.; Jones, F. N.; Pappas, S. P., *Organic Coatings: Science and Technology, 2nd Ed*. Federation of Societies for Coatings Technology: **1999**; Vol. 71, p 67-73.
2. Vanlandingham, M. R.; Eduljee, R. F.; J. W. Gillespie, J., Moisture Diffusion in Epoxy Systems. *Journal of Applied Polymer Science* 1999, 71, 787-798.
3. Musto, P.; Mascia, L.; Ragosta, G.; Scarinzi, G.; Villano, P., The transport of water in a tetrafunctional epoxy resin by near-infrared fourier transform spectroscopy. *Polymer* 1999, 41, 565-574.
4. van der Wel, G. K.; Adan, O. C. G., Moisture in organic coatings - a review. *Prog. Org. Coat.* 1999, 37, 1-14.
5. Soles, C. L.; Chang, F. T.; Bolan, B. A.; Hristov, H. A.; Gidley, D. W.; Yee, A. F., Contributions of the nanovoid structure to the moisture absorption properties of epoxy resins. *J. Polym. Sci., Part B: Polym. Phys.* **1998**, 36, 3035-3048.

6. Soles, C. L.; Chang, F. T.; Gidley, D. W.; Yee, A. F., Contributions of the nanovoid structure to the kinetics of moisture transport in epoxy resins. *J. Polym. Sci., Part B: Polym. Phys.* **2000**, 38, 776-791.

7. Soles, C. L.; Yee, A. F., A discussion of the molecular mechanisms of moisture transport in epoxy resins. *J. Polym. Sci., Part B: Polym. Phys.* **2000**, 38, 792-802.

8. Lyon, S. B.; Bingham, R.; Mills, D. J., Advances in corrosion protection by organic coatings: What we know and what we would like to know. *Prog. Org. Coat.* **2017**, 102, 2-7.

9. Hughes, A. E.; Trinchi, A.; Chen, F. F.; Yang, Y. S.; Sellaiyan, S.; Carr, J.; Lee, P. D.; Thompson, G. E.; Xiao, T. Q., Structure and transport in coatings from multiscale computed tomography of coatings - new perspectives for electrochemical impedance spectroscopy modeling? *Electrochim. Acta* **2016**, 202, 243-252.

10. MacQueen, R. C.; Granata, R. D., A positron annihilation lifetime spectroscopic study of the corrosion protective properties of epoxy coatings. *Prog. Org. Coat.* **1996**, 28, 97-112.

11. Madani, M. M.; Miron, R. R.; Granata, R. D., PALS free volume study of dry water saturated epoxies. *J. Coat. Technol.* **1997**, 69, 45-54.

12. Jackson, M.; Kaushik, M.; Nazarenko, S.; Ward, S.; Maskell, R.; Wiggins, J., Effect of free volume hole-size on fluid ingress of glassy epoxy networks. *Polymer* **2011**, 52, 4528-4535.

13. Frank, K.; Childers, C.; Dutta, D.; Gidley, D.; Jackson, M.; Ward, S.; Maskell, R.; Wiggins, J., Fluid uptake behavior of multifunctional epoxy blends. *Polymer* **2013**, 54, 403-410.

14. Lange, J.; Nicolas, B.; Galy, J.; Gerard, J. F., Influence of structure and chemical composition on oxygen permeability of crosslinked epoxy-amine coatings. *Polymer* **2002**, 43, 5985-5994.

15. Muramatsu, M.; Okura, M.; Kuboyama, K.; Ougizawa, T.; Yamamoto, T.; Nishihara, Y.; Saito, Y.; Ito, K.; Hirata, K.; Kobayashi, Y., Oxygen permeability and free volume hole size in ethylene-vinyl alcohol copolymer film: temperature and humidity dependence. *Radiat. Phys. Chem.* **2003**, 68, 561-564.

16. Dlubek, G.; Redmann, F.; Krause-Rehberg, R., Humidity-induced plasticization and antiplasticization of polyamide 6: a positron lifetime study of the local free volume. *J. Appl. Polym. Sci.* **2002**, 84, 244-255.

17. Mo, C.; Yuan, W.; Lei, W.; Shijiu, Y., Effects of temperature and humidity on the barrier properties of biaxially-oriented polypropylene and polyvinyl alcohol films. *J. App. Packaging Res.* **2014**, 6 (1), 40-46.

18. Cotugno, S.; Larobina, D.; Mensitieri, G.; Musto, P.; Ragosta, G., A novel spectroscopic approach to investigate transport processes in polymers: the case of water-epoxy system. *Polymer* **2001**, 42, 6431-6438.

19. Nazarenko, S.; Meneghetti, P.; Julmon, P.; Olson, B. G.; Qutubuddin, S., Gas barrier of polystyrene montmorillonite clay nanocomposites: effect of mineral layer aggregation. *J. Polym. Sci., Part B: Polym. Phys.* **2007**, 45, 1733-1753.

20. Pramanik, M.; Fowler, E. W.; Rawlins, J. W., Another look at epoxy thermosets correlating structure with mechanical properties. *Polym. Eng. Sci.* **2014**, 54, 1990-2004.

21. Bond, D. A., Moisture diffusion in a fiber-reinforced composite: Part I - non-Fickian transport and the effect of fiber spatial distribution. *J. Compos. Mater.* 2005, 39, 2113-2141.

22. Grace, L. R.; Altan, M. C., Non-fickian three-dimensional hindered moisture absorption in polymeric composites: Model development and validation. *Polym. Compos.* **2013**, 34, 1144-1157.

23. Placette, M. D.; Fan, X.; Zhao, J.-H.; Edwards, D., Dual stage modeling of moisture absorption and desorption in epoxy mold compounds. *Microelectron. Reliab.* **2012**, 52, 1401-1408.

24. Crank, J., *The Mathematics of Diffusion*. Clarendon Press: **1956**; p 347 pp.

25. Miwa, T.; Takeshita, Y.; Ishii, A.; Sawada, T., Simulation of water absorption and desorption behavior for anti-corrosion coatings in existing and new accelerated corrosion tests. *Prog. Org. Coat.* **2018**, 120, 71-78.

26. van Krevelen, D. W., *Properties of Polymers, 4th ed.*; Elsevier: Amsterdam, **2009**.

27. Tsavalas, J. G.; Sundberg, D. C., Hydroplasticization of Polymers: Model Predictions and Application to Emulsion Polymers. *Langmuir* **2010**, 26, 6960-6966.

28. Morsch, S.; Lyon, S.; Smith, S. D.; Gibbon, S. R., Mapping water uptake in an epoxy-phenolic coating. *Prog. Org. Coat.* **2015**, 86, 173-180.

29. Shi, J. F.; Inglefield, P. T.; Jones, A. A.; Meadows, M. D., Sub-Glass Transition Motions in Linear and Cross-Linked Bisphenol-Type Epoxy Resins by Deuterium Line Shape NMR. *Macromolecules* **1996**, 29, 605-9.

30. Monnerie, L.; Laupretre, F.; Halary, J. L., Investigation of solid-state transitions in linear and crosslinked amorphous polymers. *Adv. Polym. Sci.* **2005**, 187, 35-213.

31. Vlasak, R.; Klueppel, I.; Grundmeier, G., Combined EIS and FTIR-ATR study of water uptake and diffusion in polymer films on semiconducting electrodes. *Electrochim. Acta* **2007**, 52, 8075-8080.

32. Hiltner, A.; Liu, R. Y. F.; Hu, Y. S.; Baer, E., Oxygen transport as a solid-state structure probe for polymeric materials: A review. *J. Polym. Sci., Part B: Polym. Phys.* **2005**, 43, 1047-1063.

33. Yushkin, A.; Grekhov, A.; Matson, S.; Bermeshev, M.; Khotimsky, V.; Finkelstein, E.; Budd, P. M.; Volkov, V.; Vlugt, T. J. H.; Volkov, A., Study of glassy polymers fractional accessible volume (FAV) by extended method of hydrostatic weighing: Effect of porous structure on liquid transport. *React. Funct. Polym.* **2015**, 86, 269-281.

CHAPTER IV – TUNING OF TRANSPORT AND THERMOMECHANICAL PROPERTIES OF MIXED THERMOSET NETWORKS AND COATINGS

4.1 Introduction

A pragmatic method of establishing structure-property relationships in epoxy-amine systems has been the utilization of network series whereby a number of distinct matrices are prepared using separate combinations of resins and crosslinking agents and the resulting material properties are evaluated and related to the chemical composition and structural attributes. This is demonstrated in studies reported by Soles and co-workers which evaluated the impact of monomer flexibility and functionality on free volume properties and transport kinetics.[1-2] Additionally, Linde and co-workers compared epoxy-amine matrices composed of disparate crosslinking agents to determine what influence T_g has on moisture diffusion and solubility.[3] However, this method of analysis as applied to the influence of water transport characteristics of a coating binder on inhibitor release and protection efficacy of pigmented coatings is not currently found in the literature. The following research is intended to serve as a means of developing an understanding of the relationships between polymer matrix properties and inhibited primer performance using a series of mixed thermoset networks composed of the same monomeric materials.

Many coatings, and in particular corrosion protection primers, are formulated around polymeric binder materials which are typically glassy in nature with T_g values that vary between 50-150 °C. A higher value is assumed to aid in preventing shifts in coating physical properties upon exposure to a variety of environmental challenges including periodic temperature, moisture, and pressure fluctuations.[4-5] Glass-forming

polymers, including thermoset matrices, represent a non-equilibrium thermodynamic state and as such are prone to physical aging processes. This occurs slowly at temperatures well below the T_g as a gradual shift in molecular configuration via rearrangement to reach a condition closer to equilibrium but is accelerated when exposed to temperatures 10-20 °C within the transition range. Several material property shifts accompany the physical aging process and includes increases in density, modulus, and brittleness in addition to decreases in viscoelastic response and toughness, all of which could potentially impact performance of a coating derived from a glassy polymer. Additionally, small molecule transport rates are diminished as a function of physical aging due to decreases in free volume and would therefore impact both the barrier properties and inhibitor release capability of a pigmented primer coating.[6-7] Due to the tendency of water to depress polymer T_g via the process of hydroplasticization, it could be assumed that sorption of significant quantities would assist in accelerating the physical aging of a given coating system. However, it was demonstrated that exposure of urethane and polyester/melamine coatings to increasing levels of relative humidity had the result of accelerating the initiation but hindering the overall extent of physical aging as compared to dry thermally treated samples.[8] Nevertheless, the impact of specific network features on the interplay between physical aging, transport processes, and inhibited primer protection is still unknown.

In this chapter the relationships between glass transition temperature, crosslink density, and hydrophilic network component proportion and the extent to which transport properties can be adjusted while maintaining a set of matrix structural and compositional targets is described. This was achieved using a series of mixed epoxy-amine systems

consisting of a singular epoxy resin, a chain extender, and two different crosslinking agents, the relative ratios of which were manipulated for iterative shifts in material features. The resulting sample thermomechanical and moisture transport characteristics were observed and compared in both dry and relative humidity-exposed conditions and the impact on physical aging was observed. Free film and substrate-bound coatings, both pigmented and non-pigmented, were developed from a selection of these matrices and the extent of water-polymer interaction was assessed with ATR-IR while the corrosion protection efficacy of the formulations while under static salt fog conditions was observed.

4.2 Experimental

4.2.1 Methodology

A series of nine different epoxy-amine networks were formulated using a single liquid epoxy resin (E825), a chain extender (either BA or PL4200 for Network Series 1 (NS1) and 2 (NS2), respectively), and a mixture of crosslinking agents (ED600 and either 1,3-BAC (NS1) or MPMD (NS2)), all formulated to a 1:1 epoxy:amine-hydrogen stoichiometry. The chemical structures of the monomer components are given in Figure 4.1.

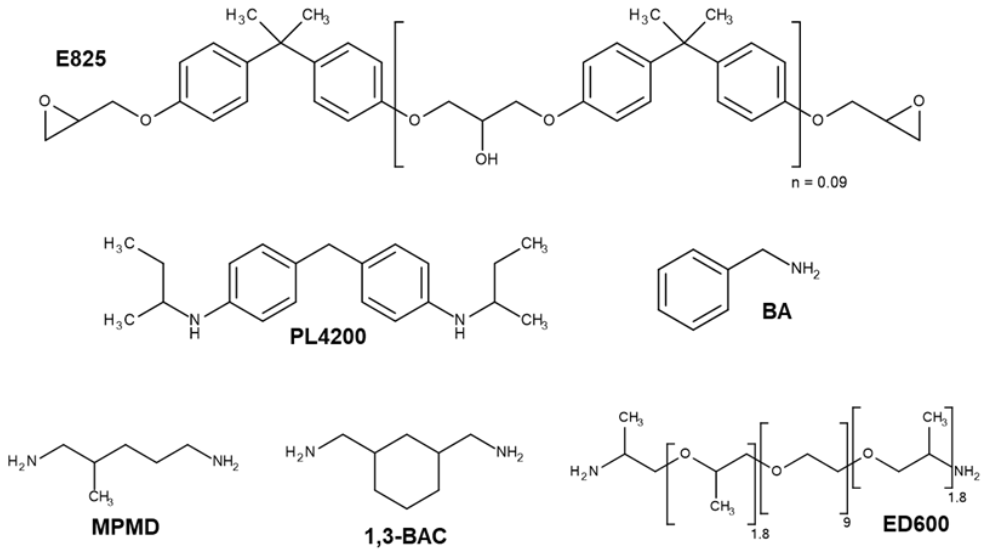

Figure 4.1 Chemical structures of epoxy resin (top) along with primary monoamine and di-secondary amine chain extenders (middle) and tetrafunctional amine crosslinking network reactants (bottom).

Within the respective networks series (NS1 and NS2) each matrix was formulated to contain all of the same monomers (epoxy, chain extender, and two crosslinking agents) in varying quantities as to maintain a 1:1 epoxy:amine-hydrogen stoichiometry and targeted crosslink density and crosslinking agent equivalent percentage.

4.2.2 Epoxy-Amine Network Formulation

A series of nine distinct epoxy-amine networks was prepared with three separate crosslink density ranges (M_c = high, mid, or low) and hydrophilicity levels as contributed by the ED600 polyethylene oxide component while maintaining a 1:1 epoxy to amine-hydrogen stoichiometry for all thermosets. By controlling the percent of amine content provided by the ED600 (≤ 30, ≈ 50, or ≥ 70 eq%) versus the small molecular weight crosslinking agent (MPMD or 1,3-BAC), both the glass transition temperature and hydrophilic nature of overall network was varied. Additionally, the crosslink density was

adjusted to three distinct levels by the careful selection of the ratio of epoxy resin (E825) and chain extender (PL4200 or BA) proportions. Figure 4.2 demonstrates the intended shifts in network structural and compositional features as a function of reactive component ratios. Within each row the network T_g decreases while hydrophilicity increases from α to γ due to increasing ED600 content and each column represents an increase in crosslink density from I to III as the ratio of E825 to chain extender increases. This strategy of network design allows for the creation of a series of distinct epoxy-amine materials that vary in chemical and topological features to the extent that transport properties of water, salt, and inhibitor are impacted. Two different versions of the network series were formulated and prepared: the first employed the use of crosslinking agent 1,3-BAC and chain extender BA (Network Series 1, NS1) while the second substituted these reactants with crosslinking agent MPMD and chain extender PL4200 (Network Series 2, NS2). The resulting formulations were adjusted to ensure the same degree of variability in crosslink density while maintaining 1:1 reactant stoichiometry in both NS1 and NS2. The two different series were produced to provide some flexibility in processing and sample preparation with most fundamental polymer characterizations carried out on NS1 networks and coatings (both pigmented and pigment-free) analyses carried out on NS2 networks.

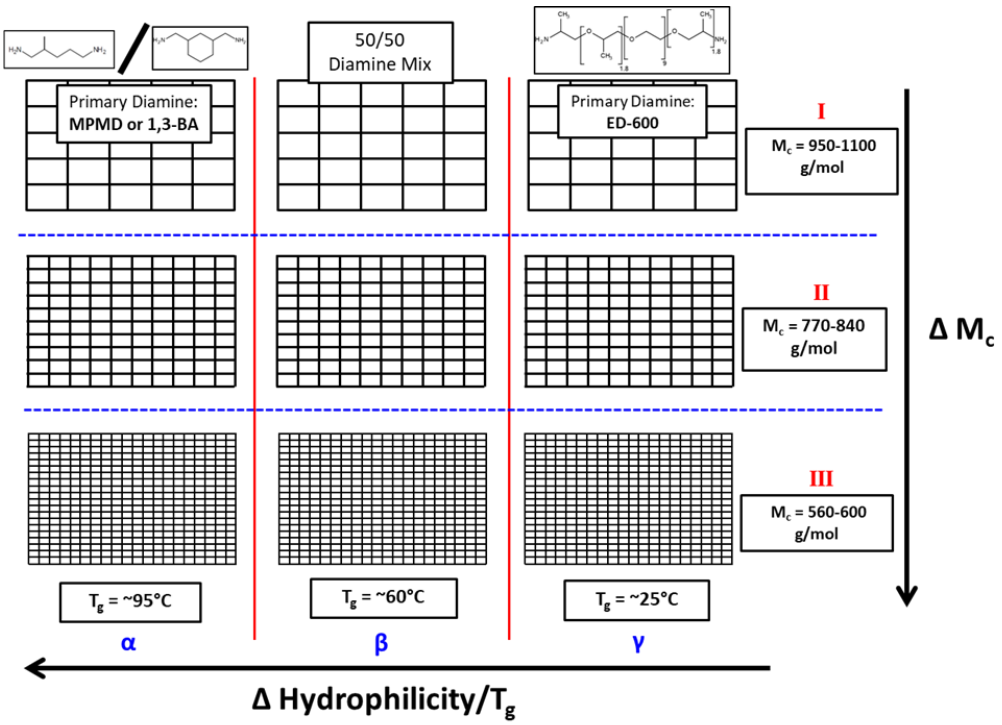

Figure 4.2 Outline of networks series consisting of nine networks containing the same four molecular components at varying ratios.

4.3 Results and Discussion

4.3.1 Thermomechanical Properties of Network Series

Bulk polymer samples (bars) of each of the nine network formulations from NS1 were evaluated via DMA and DSC to evaluate the extent to which varying the network reactant proportions varied the resulting T_g values. Figure 4.3 illustrates the thermomechanical response measured during DMA testing with the tan δ and E′ signals highlighted. It is immediately apparent that three specific groupings exist, owing to the three levels of crosslinking agent ratios included within the networks (α, β, and γ). Glass transition temperatures range from approximately 50 to 95 °C with the lower T_g ranges corresponding to γ networks and higher T_g values represented by α formulations. T_g

values within each grouping were anticipated to increase from I to III as crosslink density increased due to higher ratios of E825 to chain extender BA. However, given the higher molecular flexibility of ED600 the β and γ groupings exhibited limited to slight decreases in T_g with decreasing chain extender and increasing crosslink density per unit volume, respectively.

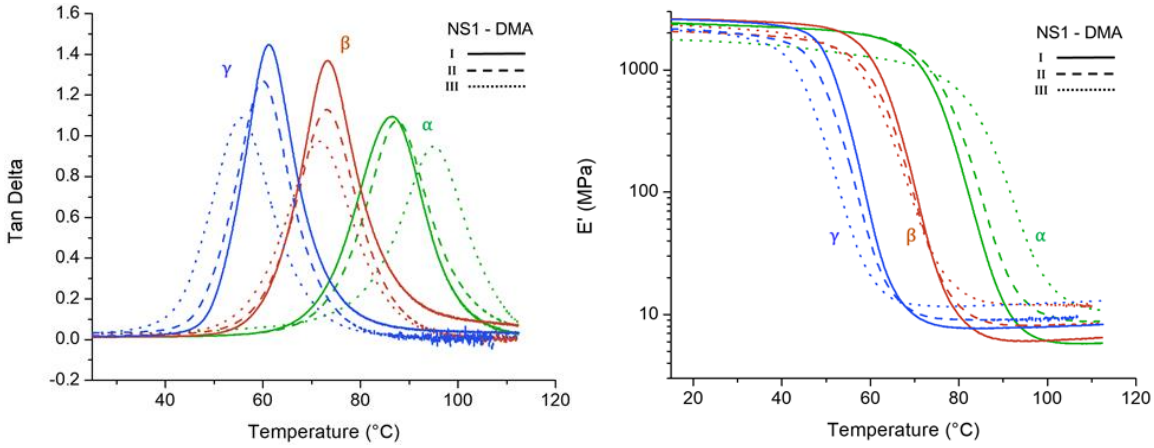

Figure 4.3 DMA overlays of all NS1 formulations detailing the Tan Delta (tan δ, left) and Storage Modulus (E′, right).

These trends were also observed in DSC testing as shown in Figure 4.4, with increasing measured T_g values in the α series as crosslink density increases while the reverse development is found in γ network group. As is commonly encountered in these two methods the DMA T_g values observed are approximately 10-20 °C higher than those found in DSC analysis. A comparison of measured glass transition values (DMA and DSC) is given in Table 4.1.

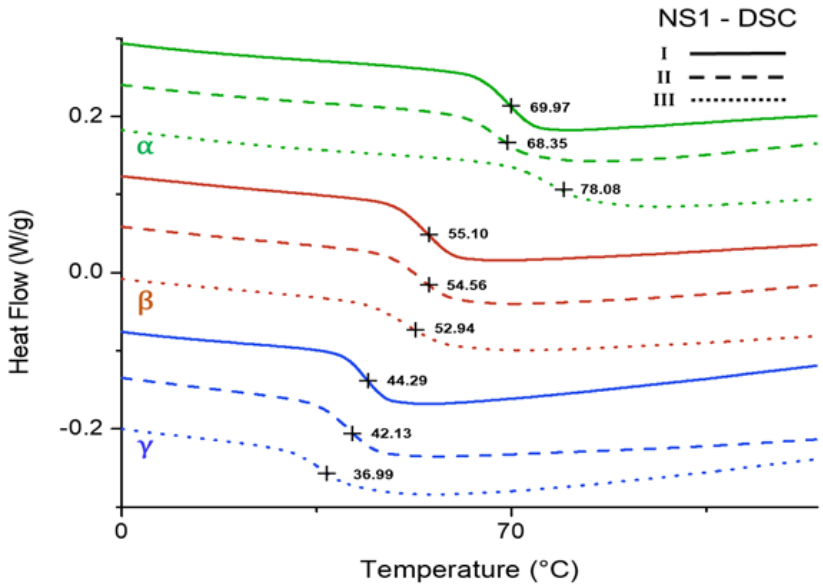

Figure 4.4 DSC overlays of all NS1 formulations detailing the glass transition during the second heating cycle (exotherm up).

Table 4.1

Network Series 1 Measured Glass Transition Temperatures (°C)

Formulation	DMA	DSC
α-I	86.59	69.97
α-II	86.37	68.35
α-III	95.24	78.08
β-I	74.24	55.10
β-II	73.40	54.56
β-III	71.88	52.94
γ-I	60.53	44.29
γ-II	60.09	42.13
γ-III	54.69	36.99

In order to confirm that crosslink density values and groupings conformed to those anticipated based on formulation specifics the post-T_g E′ values were measured and the resulting molecular mass between crosslink junctions (M_c) values were calculated according to the theory of rubbery elasticity as given by the following equation:

$$M_c = \frac{q3\rho RT}{E'_{T_{g+50}}}$$

where q is a front factor (usually assumed to be 1), ρ is the sample density, R is the universal gas constant, T is the temperature at 50 K above T_g, and E′ represents the storage modulus at 50 K above T_g.[9] Three sample bars of each formulation were used to measure average density using the Archimedes method by measuring the samples in air and water.

Similarly, the crosslink density (v_c), or the moles of elastically effective network chains per unit volume, as given by the expression:

$$v_c = \frac{E'}{3RT}$$

was monitored and compared between measured and theoretical values. The resulting quantities are summarized in Table 4.2.

Table 4.2

Network Series 1 Theoretical and Measured v_c and M_c

Formulation	v_c (theoretical) (mol/cm^3 · 10^{-4})	M_c (theoretical) (g/mol)	v_c (measured) (mol/cm^3 · 10^{-4})	M_c (measured) (g/mol)
α-I	12.18	950.17	5.69	1733.27
α-II	15.00	774.53	8.63	1346.11
α-III	19.54	591.78	10.4	1111.65
β-I	12.22	950.16	6.48	1591.63
β-II	14.97	778.06	8.31	1302.20
β-III	19.52	596.82	12.3	946.71
γ-I	12.04	960.24	8.29	1403.35
γ-II	14.80	786.61	9.64	1207.01
γ-III	19.34	603.36	13.3	876.77

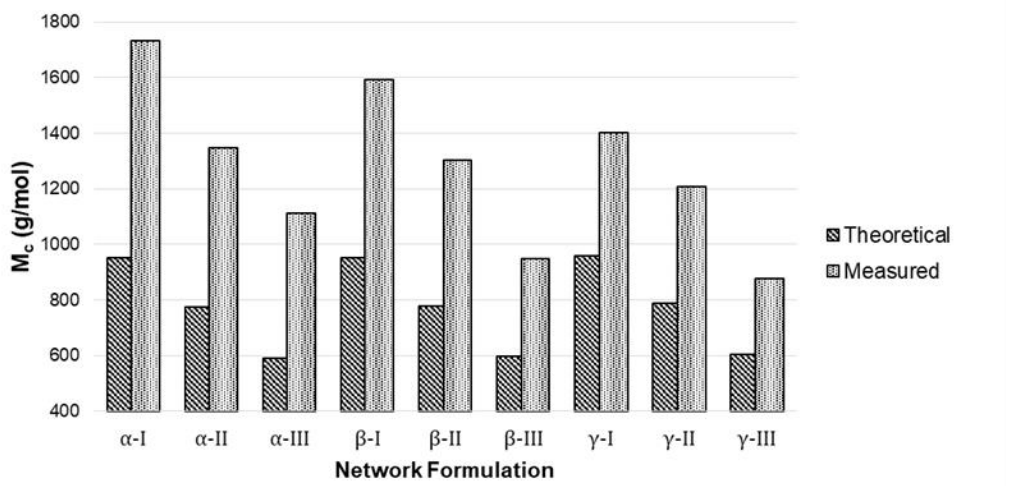

Figure 4.5 Comparison of theoretical and measured M_c values as determined from the theory of rubbery elasticity.

Figure 4.5 compares the differences in theoretical and measured M_c quantities as determined from DMA results for all network formulations. It is seen that all matrices exhibit measured crosslink density values approximately half as high as estimated via the empirical method (measured M_c values are twice as high as theoretical). Deviations from estimated values have been previously noted as larger M_c values are reached (lower crosslink density ranges) using this method.[9] Other sources for the variability may include a difference in front factor (q) between the samples or potential interference between competing epoxy-amine reactions of each crosslinking agent or chain extender, resulting in a number of unreacted functional groups or network defects. DSC thermographs exhibited no residual exothermic activity within the temperature range tested, signifying that the substantially higher M_c values are not due to low conversions but rather inherent to the mixed thermosets as formulated. For the purposes of this research, however, the ultimate crosslink density ranges are not restrictive and rather the

relative increases and spacing between column groupings (I to III for all amine proportions) represent satisfactory variability in network structural features.

4.3.2 Dynamic Vapor Sorption

Polymer thin film discs of each of the nine network formulations from NS1 were subjected to gravimetric experiments under high humidity environments (DVS) at 25 °C. Figure 4.6 illustrates the respective sorption behaviors of the epoxy-amine networks where it is found that, in general, relative quantities of water absorbed by each formulation is similar to the proportion of the hydrophilic amine, ED600 ($\alpha < \beta < \gamma$). Additionally, within each group the trend of increasing absorbed water amounts follows the increase in crosslink density (I < II < III), which is likely due to a combination of two factors: firstly, each crosslink junction is composed of a tertiary amine and two hydroxypropyl ether segments, which are functional groups with a propensity for polar and hydrogen-bonding interactions and are therefore hydrophilic. It has also been observed that increasing crosslink density is accompanied by an increase in free volume fraction, which allows for a greater amount of water to ingress within the polymer.[12]

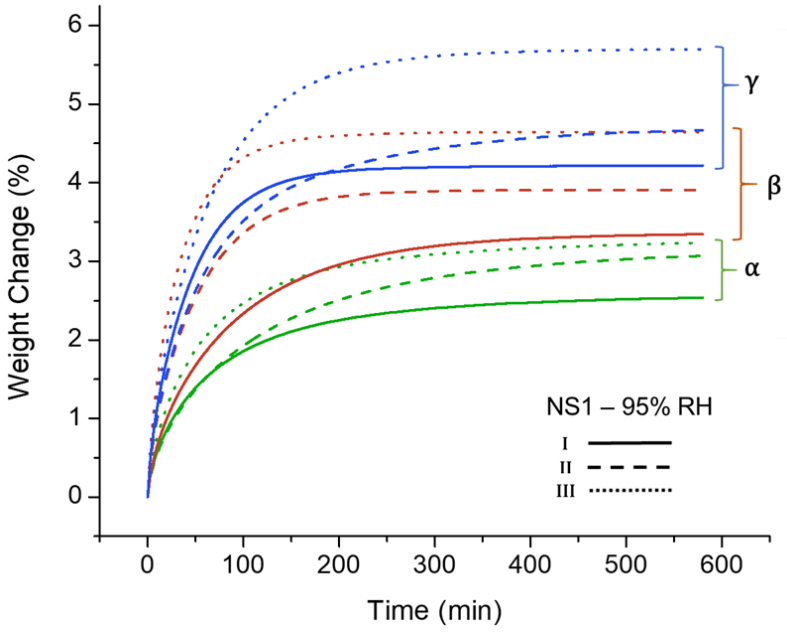

Figure 4.6 Gravimetric analysis of NS1 epoxy-amine samples via DVS testing.

Interestingly, there exists some overlap between some network formulations, specifically, β-I/α-III and γ-II/β-III appear to take on similar amounts of moisture which suggests that the hydrophilic nature of the polymer matrices is a balance of the molar volume of hydrophilic crosslink junction functional groups and the polyethylene oxide segments of the ED600 crosslinking agent. In addition to the total amount of water ingress the rates of diffusion, *D*, were calculated according to the methods outlined in Chapter III, which are outlined in Figure 4.7.

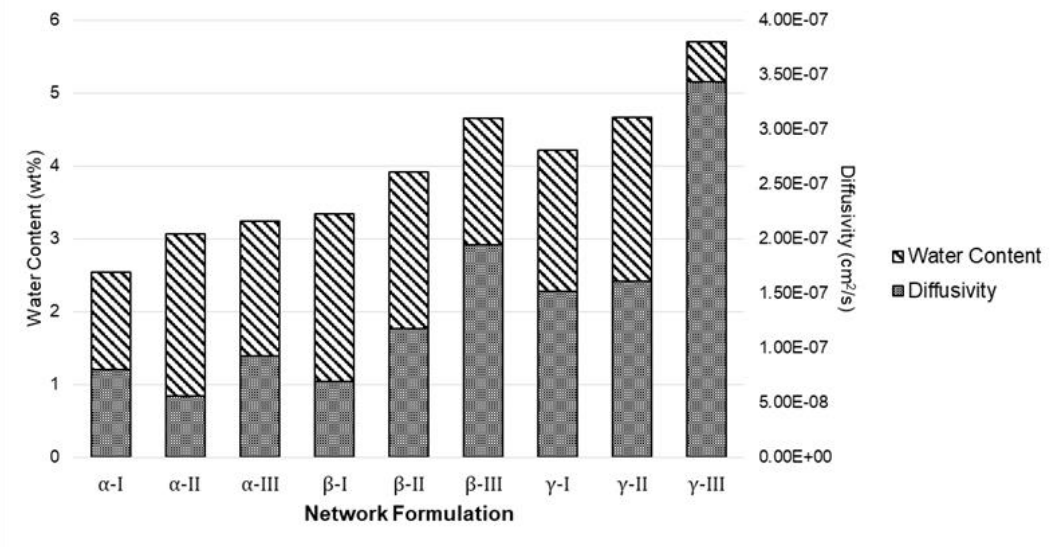

Figure 4.7 Comparison of water sorption contents and rates as measured by DVS.

In general the diffusivity of each epoxy-amine formulation scales with the total amount of absorbed water, although there are some deviations from this trend. It is apparent from these results is the tendency for both the total amount of water absorbed and the rate of water sorption increases primarily with the quantity of the hydrophilic ED600 component. This is reflected in the water vapor transmission rate analysis as determined using the dry cup method of gravimetric analysis (ASTM E-96) in 95% RH at 25 °C, as illustrated by Figure 4.8.

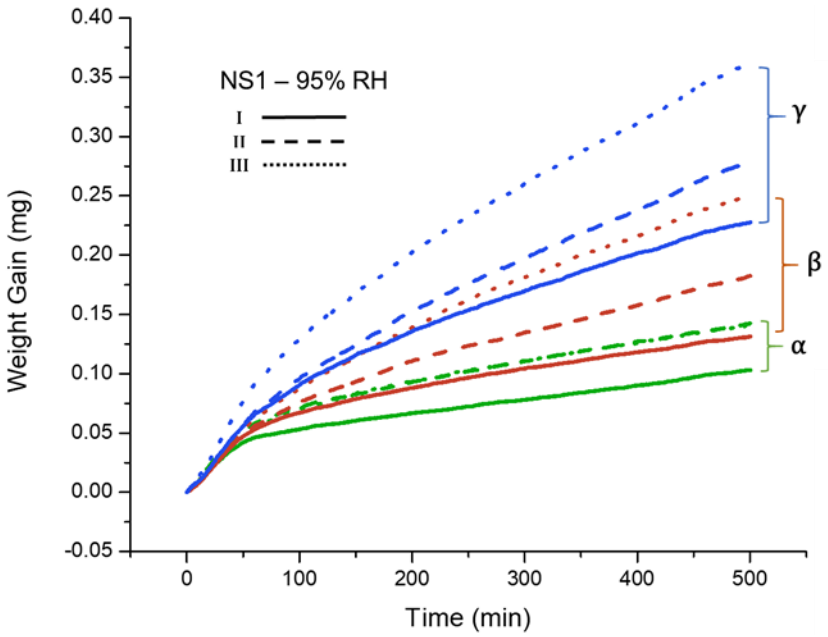

Figure 4.8 Water vapor transmission analysis of NS1 epoxy-amine samples via DVS testing.

As with the sorption analysis the variance in moisture transmission appears to scale primarily with the proportion of hydrophilic crosslinking agent while within each grouping the tendency for greater amounts of vapor to permeate the film progresses with increasing crosslink density. After taking into consideration sample thickness and area the water vapor transmission rate (WVTR) can be determined using the slope of mass increase as a function of time within the linear region at which point the polymer sample is saturated with moisture and a steady rate of water vapor permeates the polymer. Table 4.3 provides a summarization of moisture content at saturation, diffusion coefficient, and water vapor transmission rates of the network formulations under 95% RH.

Table 4.3

Network Series 1 Moisture Sorption Characteristics (95% RH, 25 °C)

Formulation	Water Content (wt%)	Diffusivity ($cm^2/s \cdot 10^8$)	WVTR ($mg/min \cdot mm^2 \cdot 10^7$)
α-I	2.537	8.01	1.567
α-II	3.069	5.63	2.029
α-III	3.234	9.36	1.847
β-I	3.342	6.94	1.987
β-II	3.909	11.8	2.918
β-III	4.648	19.4	4.159
γ-I	4.215	15.2	3.552
γ-II	4.669	16.1	5.061
γ-III	5.699	34.3	7.145

4.3.3 Impact of Hydroplasticization on Thermomechanical Properties

Free film strips of cured NS1 epoxy-amine samples were subjected to RH-DMA thermal sweeps in tensile mode under "dry" and "wet" conditions to compare the extent of hydroplasticization that occurs as a function of crosslink density, moisture content, and T_g and the resulting impact on thermomechanical properties. Samples were installed within the RH-DMA clamp chamber and held at either 95% RH and 25 °C ("wet" condition) or 0% RH and 60 °C (to remove any residual moisture) for up to 300 minutes during equilibration before cooling slowly to 5 °C, at which point the thermal scan proceeded as normal while maintaining the respective relative humidity levels. Figure 4.9 reveals the shifts in T_g as gauged by the tan δ signal under wet and dry conditions. It can be seen that between 90-100 °C many of the samples under the 95% RH condition exhibit artificial peaks in tan δ which are likely caused by the water nearing its boiling point and is amplified in networks which maintain higher T_g values (primarily α matrices) and for the purposes of this work will be ignored.

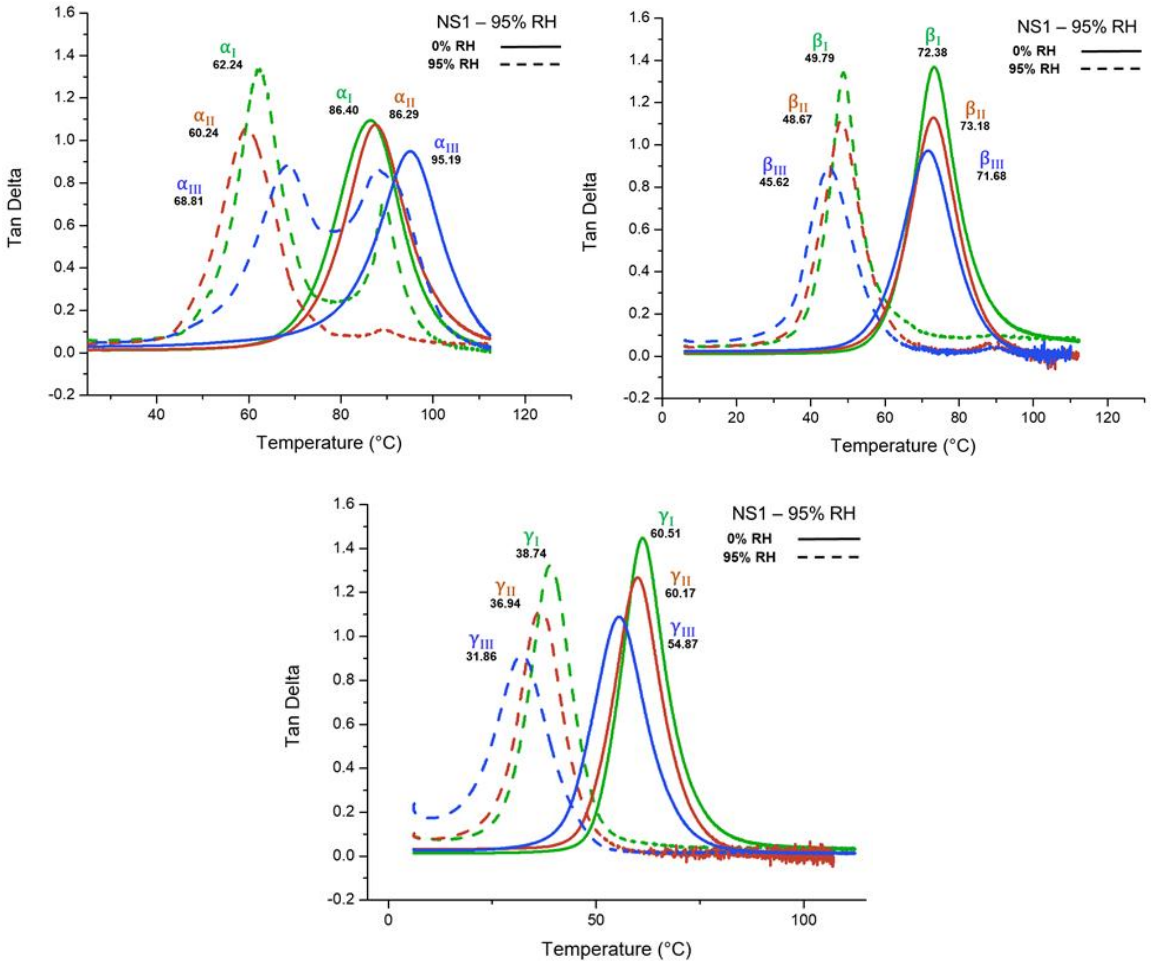

Figure 4.9 RH-DMA tan δ signals of the nine separate NS1 epoxy-amine formulations within 0 and 95% RH environments demonstrating the relative degrees of hydroplasticization in α, β (top left and right, respectively) and γ networks (bottom).

The primary focus of this analysis, however, is the drop in glass transition temperature for each network formulation due to plasticization by the presence of moisture. It can be seen that nearly all of the samples exhibit decreases in T_g by 20-30 °C from dry to wet conditions, as illustrated in Figure 4.10. Again the tendency for increasing crosslink density to correspond with heightened amounts of water ingress results in a more substantial impact on T_g shift. However, within these results the impact

of hydrophilic network component ratio does not trend with the extent of hydroplasticization. That is to say that the formulations which absorb the highest quantities of water and exhibit the highest water vapor transmission rates do not also reveal the greatest decreases in glass transition temperature. This becomes clear following normalization of each network's T_g shift by the respective quantity of water ingress during DVS testing (Figure 4.10) after which it is found that the thermomechanical reduction per wt% moisture sorption decreases as the total amount of water uptake increases. One probable cause for this is the higher flexibility imparted by the hydrophilic ED600 segments which contribute to lower T_g values under dry conditions while maintaining similar or higher crosslink density values than those exhibited by α or β formulations.

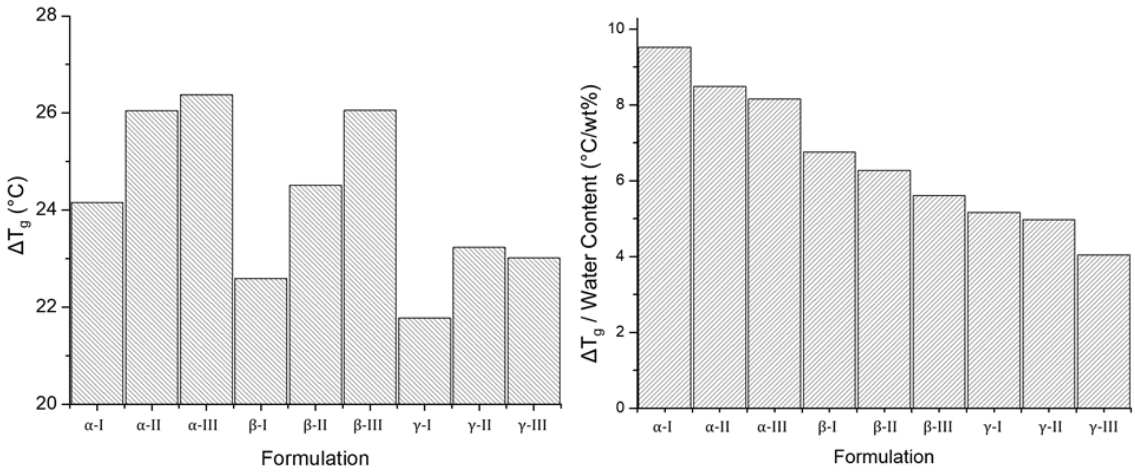

Figure 4.10 Degree of hydroplasticization as measured by shift in T_g from 0 to 95% RH.

Another method of thermomechanical evaluation via RH-DMA included the measurement of swelling-induced tensile displacement or strain during isothermal RH exposure or sweeps. During these tests a sample was held within the clamp under a very

slight preload force (0.001 N) and equilibrated at 0% RH and 25 °C for a period of 120 minutes at which point a 95% RH environment was introduced to the chamber and the displacement or strain required to maintain the static tensile force was monitored as a function of time. It was assumed that the increase in displacement following exposure to the high humidity conditions is due solely to swelling that occurs concomitantly with moisture sorption within the dimension of the applied force.

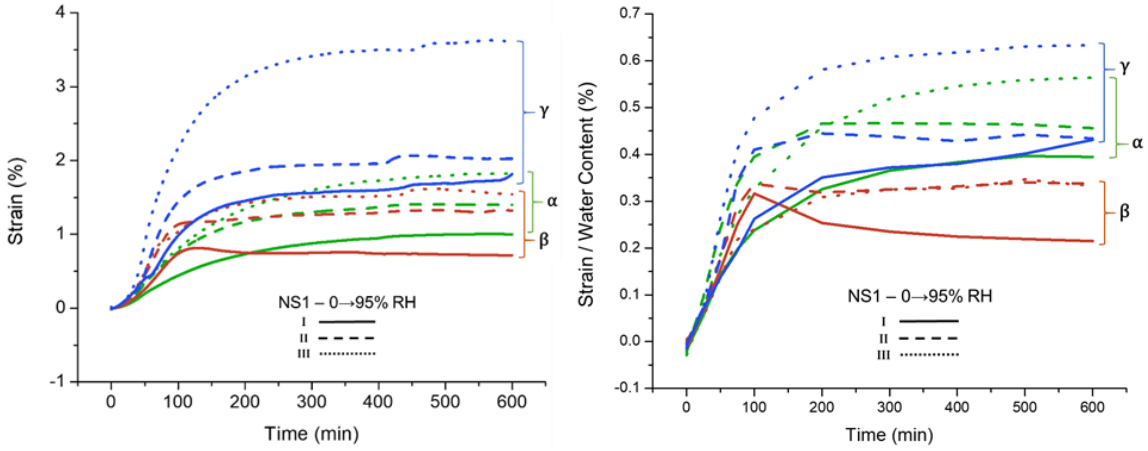

Figure 4.11 Degree of moisture-induced swelling as measured by tensile strain (left) and development of strain per water sorption content (right).

Figure 4.11 highlights the variability in swelling-induced strain that occurs upon shifting from low to high moisture environments with some resemblance of water sorption and transmission time dependencies and an equilibration state achieved by most formulations at longer periods. As with previous analyses the γ group of networks exhibits the most change following exposure due to sorption of the highest quantities of water and within each group increasing crosslink density (I to III) corresponds with heightened degrees of strain development (again, due to more relative water ingress). However, an unexpected deviation from other results is the lower strain developments in

β matrices than α (β < α < γ) despite absorbing a generally higher concentration of water per sample. This becomes more evident following normalization of the strain curves by the respective water content of each formulation with respect to time as determined via DVS, with a more substantial increase in swelling-induced strain per water sorption amount in α and γ than β. Although the exact cause for this is not clear the near 50:50 equivalents content of amine crosslinking agent types within this group may allow for redistribution of water molecules within the network structure in such a way that a minimum stress level is attained. This dissimilarity in strain development during hygrothermal conditioning demonstrates that epoxy-amine networks may take on analogous quantities of moisture but distribute or "manage" the water in different regards.

4.3.4 Physical Aging in Wet and Dry Environments

Free film samples of all nine networks of NS1 were subjected to extensive (long-term) physical aging experiments in both wet and dry conditions. Following sample preparation and cure, free film discs of approximately 15 mm diameter were placed in labeled scintillation vials that were either empty or filled with DI H_2O. These samples were then stored under ambient conditions for 250 days before removing, drying, and cutting small sections for DSC analysis. Figure 4.12 compares the first heating cycle of each formulation under wet and dry aging following exposure. It is immediately apparent that the dry-aged formulations undergo more extensive physical aging, as is seen from the larger enthalpy recovery peaks near the T_g of specific formulations. Additionally, a greater number of dry-aged formulations exhibit the effects of physical aging as compared to those aged while immersed in DI H_2O. The extent to which the physical

aging differs between wet and dry conditions is illustrated in Figure 4.13 which directly compares each formulation during the first and second heating scans following exposure to the different conditions.

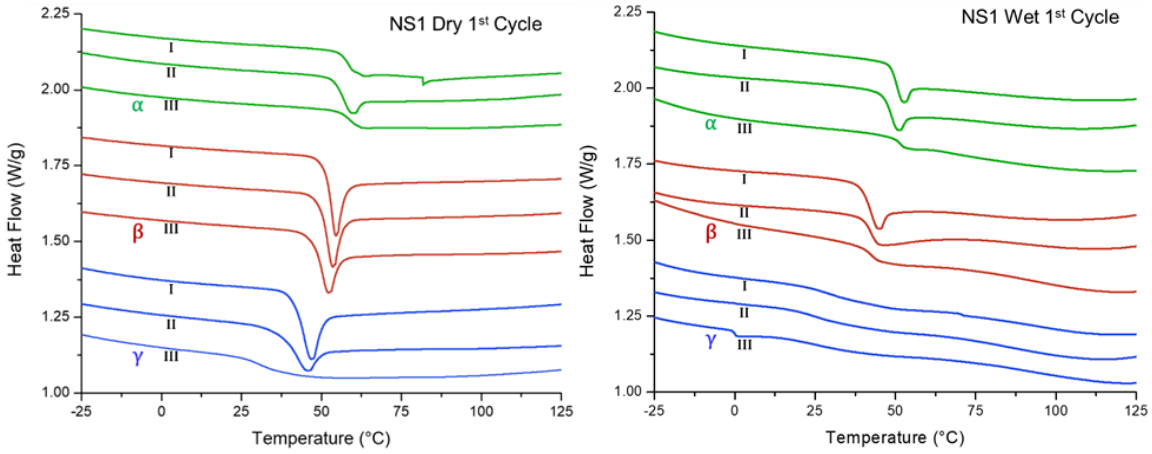

Figure 4.12 DSC heating thermographs (first heating cycle) of dry (left) and wet-aged (right) samples following 250 days of exposure.

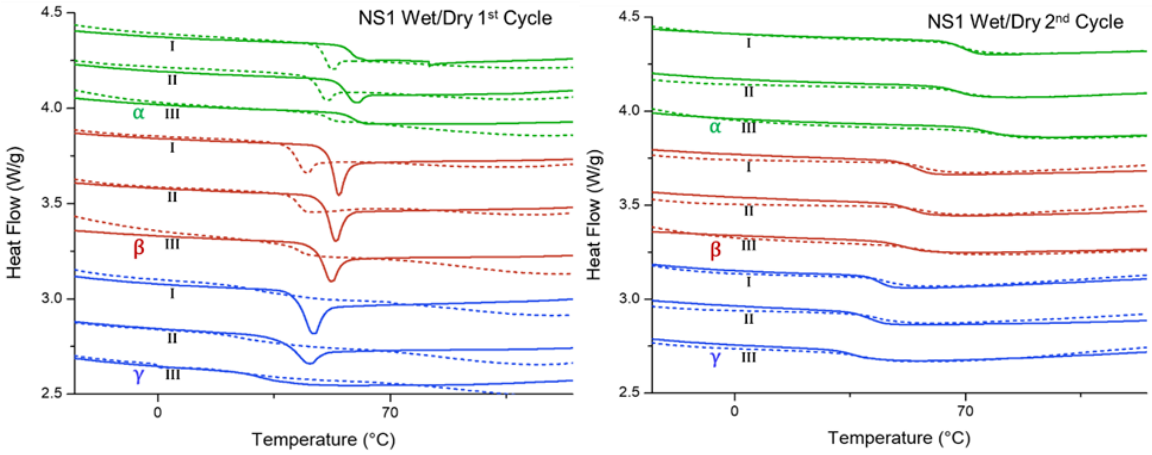

Figure 4.13 DSC heating thermograph overlays of first (left) and second (right) heating cycles of both wet (dashed lines) and dry-aged (solid lines) samples following 250 days of exposure.

It is apparent from the overlay of dry-aged (solid lines) and wet-aged (dashed lines) second cycle DSC thermographs that despite the variability in extent of physical aging between exposure conditions, the removal of moisture and thermal history during the first heating cycle results in plots that overlap nearly exactly. This suggests that no permanent changes to the polymer network compositional or structural characteristics are inflicted by the presence of water during physical aging but also reveals that the presence of moisture severely impedes the aging process. It could be anticipated that the occupation of free volume within the polymer matrix by the water molecules acts as a buffer for physical aging by eliminating available space for conformational or configurational ordering or compression. This is despite the hydroplasticizing effect that water has on epoxy-amine polymer chains which would otherwise aid glassy networks to reach equilibrium dynamic states through physical aging processes.

In order to compare the extent of physical aging of each sample the endotherm area correlating to enthalpy recovery peak near the glass transition region is calculated using previously defined methods.[13] When examining the quantified enthalpy recovery of wet and dry-aged samples, as seen in Table 4.4, it is seen that the dry samples do in fact exhibit greater extents of physical aging than those subjected to immersion conditions.

Table 4.4

Network Series 1 Physical Aging Characteristics

Formulation	Dry T_g (°C)	Wet T_g (°C)	M_{sat} (wt%)	Dry ΔH (J/g)	Wet ΔH (J/g)
α-I	76.40	62.24	2.5	0	2.163
α-II	78.29	60.34	3.1	2.626	2.367
α-III	95.19	68.81	3.2	0	0
β-I	72.35	49.79	3.3	6.247	3.347
β-II	73.36	48.67	3.9	6.424	3.963
β-III	71.90	45.62	4.6	6.095	0
γ-I	60.51	38.74	4.2	7.582	0
γ-II	60.17	36.94	4.7	6.006	0
γ-III	54.87	31.86	5.7	0	0

It has been previously established that exposure of a single coating type to increasing RH levels results in faster initial rates of physical aging but lower final degrees of aging, with a lower T_g - $T_{exposure}$ value correlating with smaller enthalpy recovery peaks at the conclusion of exposure.[8] However, the findings illustrated here reveal that the interplay between T_g, amount of water sorption (and thus T_g hydroplasticization), and crosslink density may further influence the physical aging process.

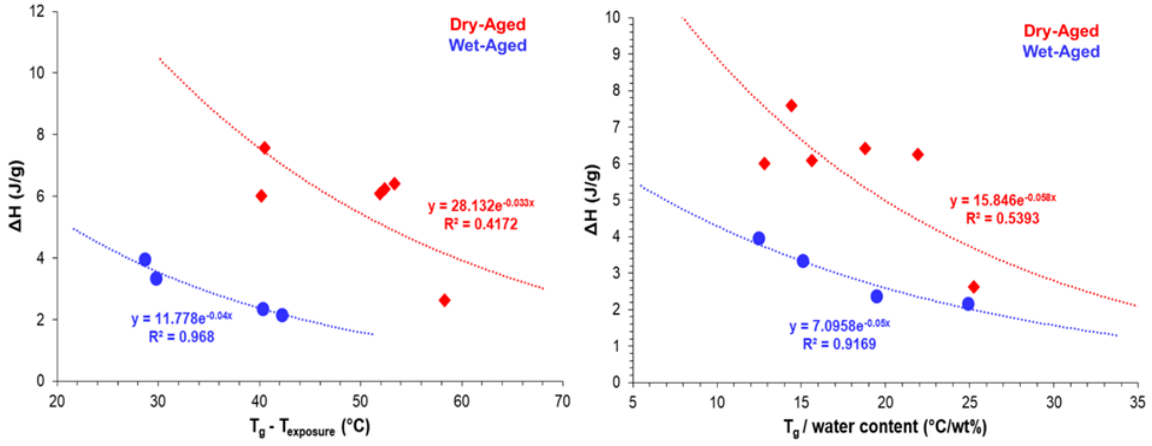

Figure 4.14 Comparison of wet (blue) and dry-aged (red) sample measured enthalpy recovery as a function of reduced T_g (left) and normalized by the total amount of moisture absorbed at saturation (right).

In Figure 4.14 the extent of variability in physical aging between the different conditions is illustrated with a clear differentiation of wet (blue) and dry-aged (red) enthalpy recovery values after 250 days aging while all demonstrate exponential trends. It is found that, in general, as the T_g of the network increases the extent of physical aging decreases owing to the fact that the exposure temperature does not meet or exceed the thermal energy barrier that must be overcome in order to allow for sufficient polymer chain mobility (at least at accelerated rates). This is also encountered when normalized by the amounts of water each respective network absorbs near the saturated state, as determined via gravimetric analysis of samples immersed in DI H_2O. Interestingly, only one formulation containing the highest level of crosslink density (β-II, M_c = 595 g/mol) exhibits any extent of endothermic peak associated with physical aging. When comparing this network to the other β formulations, it is also seen that the measured enthalpy recovery peak area is less than those of β-I and β-II, indicating that increased levels of crosslinking acts to impede the physical aging process through the restriction of mobility on the scale associated with configurational rearrangement. Within the wet-aged samples none of the highest crosslink density formulations exhibited any degree of enthalpy recovery which suggests that the combination of decreased polymer chain molecular mobility and occupation of available free volume by water results in little to no capability for structural relaxation.

The resulting impact these findings could have for protective coatings, and in particular for inhibitor-containing corrosion resistant primers, could vary depending on formulation and environmental conditions. Assuming that the ingress of water and leaching or depletion of inhibitor coincides with or precedes the onset of physical aging

the resulting barrier and transport properties could be influenced in such a way that hinders the protective capability. It is hypothesized that the dissolution and leaching of inhibitor which results in residual voids would decrease barrier properties within the primer matrix while the aging process, with the potential for densification and configurational rearrangement, could mitigate or minimize some of these cavities. Additionally, permeation and other small molecule penetrant transport properties in general have been shown to decrease as physical aging proceeds.[6, 8] However, the reduction in toughness and viscoelastic response rate that also coincides with physical aging may prove detrimental to coating performance with regard to adhesion loss (due to shifts in internal stress) or impact resistance (due to mechanical stimuli). In general, these results suggest that the presence of moisture at or near saturation levels and for extensive periods of time stimulate very little, if any, physical aging to the effect that large shifts in transport or physical properties would be impacted. Whether or not any aging does arise, as determined by the development of endothermic enthalpy recovery peaks in DSC, appears to be dependent upon a balance of polymer T_g, network crosslink density, and the amount of water absorbed by the matrix. While it is possible that the sorption of moisture might plasticize the T_g of a network to within 10-15 °C of the environmental/exposure temperature, and thereby initiate accelerated aging rates, the presence of water molecules within free volume voids and cavities excludes polymer chain or segment rearrangement or densification. Additionally, increased crosslink density will hinder the mobility of polymer chains available for physical aging and may limit any rearrangement to configurational (short-term or segment) only.

4.3.5 Coating Formulations and Characterization

4.3.5.1 Coatings Preparation.

Following evaluation of physical phenomena related to transport processes, select epoxy-amine formulations of NS2 were chosen for development into fully formulated primer coatings for characterization of corrosion protection via accelerated weathering and analysis of transport behaviors using IR spectroscopy. NS2 was chosen in lieu of NS1 due to superior film forming properties while thermomechanical and water sorption properties exhibited trends nearly identical to those of NS1 presented above. Rather than preparing samples and films of each of the nine matrices, three of the networks were selected for further analysis: α-I, β-II, and γ-III due to the largest variation in properties (crosslink density, T_g, and water sorption amount) these formulations provided. Between these samples α-I exhibits the highest glass transition temperature, lowest crosslink density and water sorption at saturation while γ-III is formulated to the highest crosslink density and water sorption but reveals the lowest T_g and in this regard β-II offers a middle ground to each of these characteristics.

Between these systems two separate preparations were developed: pigmented, containing solvents along with filler and inhibitor pigment, and non-pigmented, containing only solvents. For this study anatase titanium dioxide (TiPure™ R-902+, DuPont) and strontium chromate ($SrCrO_4$, Alfa Aesar) were incorporated as filler and inhibitor, respectively, while the mixture of solvents utilized included a 1:1:1 mixture (by mass) of parachlorobenzotrifluoride (PCBTF), methyl propyl ketone (MPK), and sec-butanol. This allowed for the direct evaluation of the impact of pigments, in this instance serving as fillers and corrosion inhibitors, on coating moisture transport and polymer-

water interactions, the exact quantities of which are given in Table 4.5. Coatings were prepared by combining epoxy resin with the solvent blend and mixing via rolling mill until homogeneous at which point the pigments were introduced and agitated through use of a mechanical stirrer then further incorporated on a rolling mill for several days. After homogenization both free films and substrate-bound coatings were prepared by mixing the appropriate amounts of pigmented epoxy grind with amine monomers as described previously and applied to either polypropylene sheets or degreased S-36 CRS SAE 1008/1010 steel Q-panels using a drawdown bar at 6 wet mils. Following an overnight drying period the coatings were subjected to the same cure profile as described previously and the steel coated panel edges were covered with a polyimide water-proofing tape prior to application of X-shaped scribes through the coatings using a hand scribing instrument.

Table 4.5

Network Series 2 Coatings Composition

Component	**α-I**	**β-II**	**γ-III**
Epoxy-Amine Mixture (g)	89.58	104.86	125.62
Solvent Mixture (g)	22.39	26.22	31.40
Solids Content (wt%)	→	80	←
Inhibitor Loading (wt%)	→	6	←
Pigment-Volume Concentration (%)	→	22.83	←
$SrCrO_4$ PVC (%)	→	2.98	←
TiO_2 PVC (%)	→	19.85	←

4.3.5.2 ATR-IR Spectroscopic Evaluation of Substrate-Bound Films.

Figure 4.15 demonstrates a collection of ATR-IR spectra as a function of time and the peaks which correspond to shifts in water absorption of degree of interaction with

polymer, specifically the asymmetrical –OH stretch (3700-3000 cm^{-1}) and H–O–H bend (1650 cm^{-1}) of substrate-bound pigmented films during exposure to 5 wt% NaCl solution.

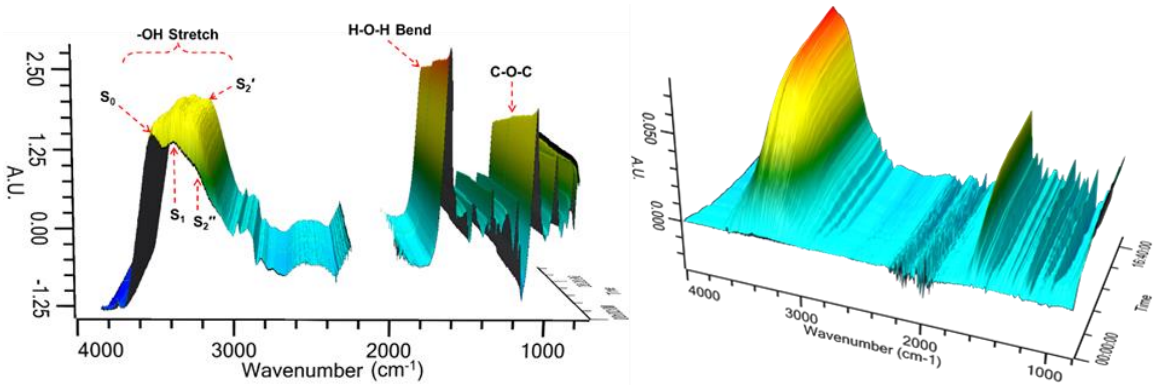

Figure 4.15 Collection of ATR-IR spectra collected at the coating-substrate interface following the introduction of water to the top side with peak assignments (left) and dry film subtraction (right) as a function of time.

The asymmetric hydroxyl stretch peak at from 3700 to 3000 cm^{-1} is associated with the degree of interaction between polymer and water through hydrogen bonding and has been presented as a method of interpreting the states of water within material. Some dispute remains regarding the exact nature of each potential water molecule condition represented by individual peaks at different wavelengths in addition to the number of possible states within this region. Resolutions of the components within this region have been reported as a culmination of anywhere between two to five separate contributions and molecular interactions, most of which are assigned to free or "unbound" water and a range of more or less "bound" or interacting states.[14-16] Additionally, the absorption peak resolution has been described by the extent of water self-interaction via separation of the signals into monomeric, dimer, chain, and cluster assignments.[17] To better identify the species of water, deconvolutions of the saturation of NS2 α-1, β-II, and γ-III were

performed and the resulting summation of the individual peaks were plotted to compare the total peak shape as well as the respective contributions from the different water types. The deconvoluted peaks for each saturation cycle were identified and compared with the area under the total peak for each water species to determine the distribution of water species at the substrate interface.

The asymmetrical hydroxyl stretch peak between 3700-3000 cm^{-1} at the time of 5 wt% NaCl saturation, approximately 16 hours, of the three separate coating systems is compared in Figure 4.16. Although the distribution of peak shape differs between α-I and β-II, the relative absorbance maximum and area is similar especially when compared to that of γ-III. Multi-peak resolution was carried out according to the methods defined by Musto and co-workers which defines four individual components according to polymer-water interaction types and one Fermi overtone assignment.[11] In addition to the increase in overall absorption peak heights of the respective components from α-I to γ-III it is observed that a shift in majority from lower wavelength components to higher values corresponds to an increase in total amount of water sorption.

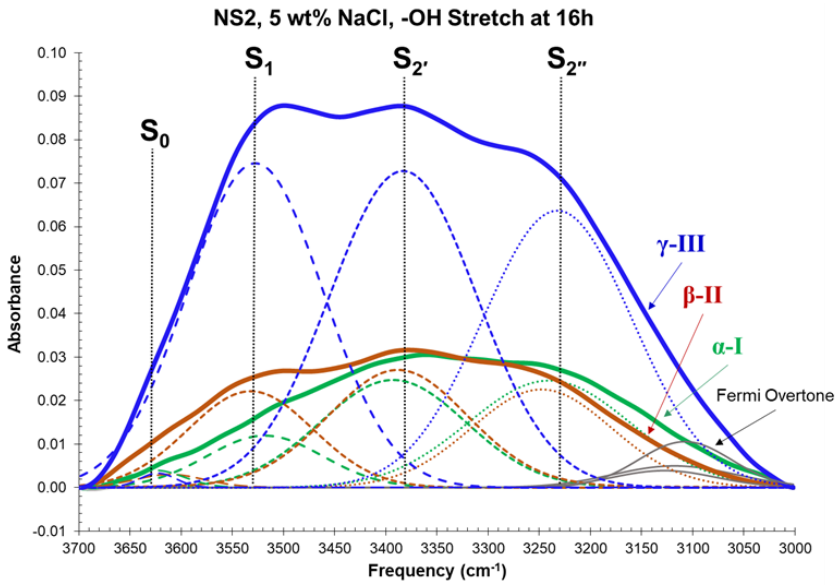

Figure 4.16 ATR-IR subtracted spectra overlay comparing the relative shifts in asymmetric hydroxyl stretch of pigmented α-I, β-II, and γ-III coatings (solid lines) detailing the distribution in water types (dashed lines).

Figure 4.17 highlights the distribution of water types within each coating system as measured from the substrate interface and denotes the peaks assigned to S_0 (free/unbound), S_1 (singly hydrogen bound), S_2' (weak doubly hydrogen bound), and S_2'' (strong doubly hydrogen bound) molecular associations. It is immediately apparent the water type S_1 scales primarily with the increase in water sorption amount, more so than others. S_2' appears to decline in proportion from α-I to γ-III although to a significantly lesser extent which indicates that higher concentrations of absorbed water in separate epoxy-amine network formulations corresponds to a greater proportion of singly hydrogen bound water and fewer doubly hydrogen bound molecules. This decrease in water-polymer interaction would likely serve to assist in heightened mobility of individual molecules. Between all coatings systems the amount of free or unbound water

represents the smallest proportion of water type which is likely due to the restricted amount of molecule clustering per free volume hole.

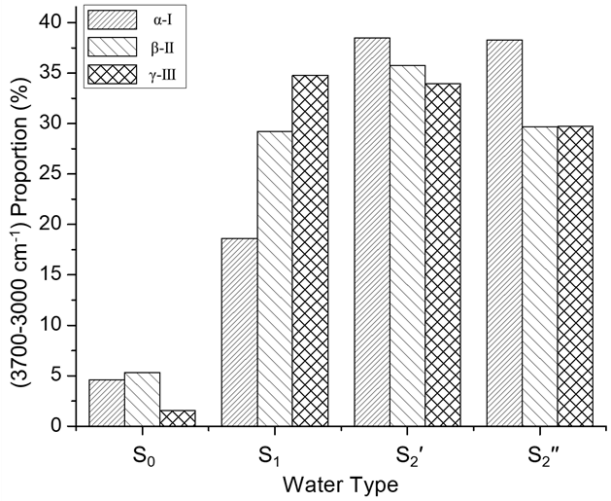

Figure 4.17 Relative quantities of water type populations for each pigmented coating following saturation in a 5 wt% NaCl solution.

Given the likelihood of cyclical exposure conditions (i.e. diurnal cycle) throughout the lifetime of a protective coating it is necessary to understand the impact of repeated moisture sorption and desorption conditions on transport properties. As seen in Figure 4.18 both the T_g and crosslink density have substantial impact on the extent to which sorption behaviors shift during multiple exposures of pigmented coatings to 5 wt% NaCl solution. The normalized uptake amounts and rates increase considerably more between cycles as T_g increases and crosslink density decreases. As reported by others, the potential for microstructural reorganization which would allow for increased access of water ingress to hydrophilic polymeric regions during subsequent immersion or exposure likely accounts for the cause of shifting sorption properties.[18] It could be reasoned that the combination of an increased glassy state (higher T_g) and lower crosslink

density (higher M_c) would result in a more extensive shift in physical properties following the uptake of moisture which would then lead to a heightened propensity for transport variability.

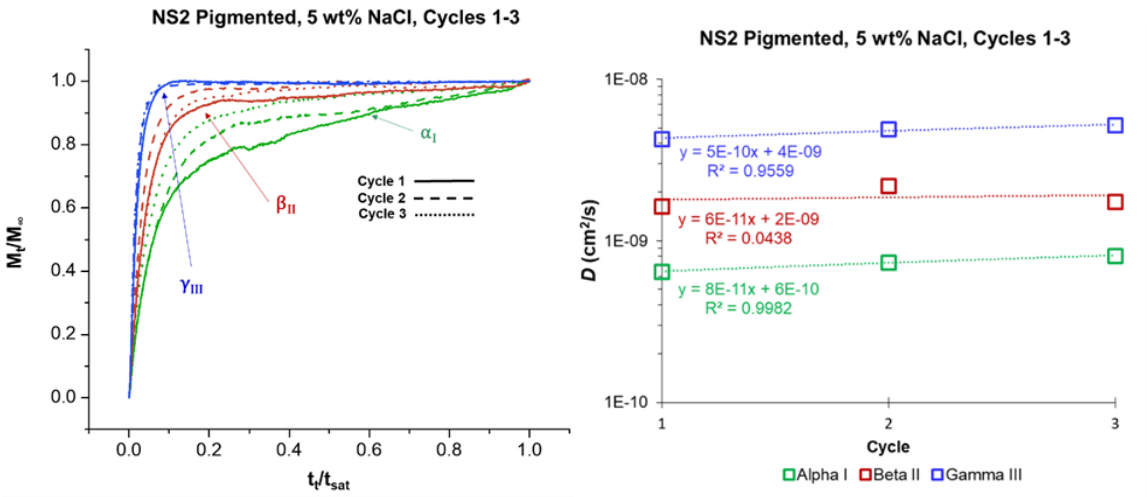

Figure 4.18 Comparison of normalized solution uptake profiles of pigmented NS2 α-I, β-II, and γ-III over the course of three separate exposures (left) and the calculated diffusion coefficients as a function of cycle (right).

The *D* values calculated from these measurements reveal a similar tendency in shifting diffusion trends with increasing rates following subsequent sorption cycles for all networks but is shown to be more substantial (higher slope from cycles 1 to 3) with α-I > β-II > γ-III. This is in agreement with RH-DMA results which indicate higher T_g and M_c values lead to more extensive shifts in thermomechanical properties and swelling per amount of water absorbed.

In addition to comparing the impact of polymer characteristics on water interaction and multiple sorption cycles, the influence of salt concentration was also investigated. Figure 4.19 illustrates the –OH asymmetric stretch peak of each network

following exposure to several solutions of varying NaCl concentration, specifically, 15, 10, 5, and 0 wt% (DI H_2O).

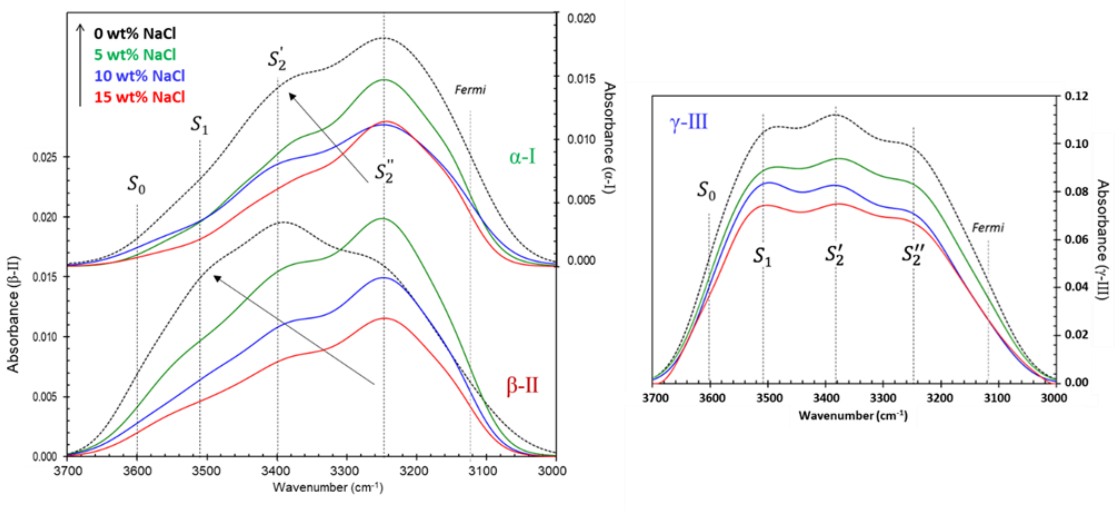

Figure 4.19 Comparison of –OH asymmetric stretch of NS2 α-I, β-II, and γ-III at saturation following exposure to salt solutions of varying concentration.

Each of the NS2 pigmented coatings exhibited increased area of normalized –OH peak absorption as salt concentration decreased, owing primarily to the decrease in water activity of the NaCl solution. In general, the distribution of water type populations did not differ significantly with change in salt concentration although β-II revealed a shift in majority area from S_2'' to S_2', or from tightly to loosely doubly-bound hydrogen bonding water. The α-I coating does exhibit a slight shift between the 5-15 wt% NaCl range of the same water types though not to the same degree and the distribution in water interaction populations of γ-III remains constant throughout each salt solution exposure. Although it is not clear why only the β-II coating exhibited this shift it could possibly be related to the relaxation or short-range rearrangement that occurs during the first sorption

cycle and availability of hydrophilic functional groups to water ingress upon subsequent exposure.

4.3.5.3 Accelerated Corrosion Protection of Steel Substrates by Pigmented and Non-pigmented Coatings.

Coatings of approximately 50-80 μm thickness were applied to cleaned steel panels and cured according to the same temperature schedule utilized for bulk polymer samples. Once dry and cured the panel edges were covered with waterproof tape and a single scribe was placed through each coating to the substrate. These were then subjected to accelerated corrosion testing according to the neutral salt spray (NSS) conditions stipulated by ASTM B117 in a salt-fog chamber (Q-FOG CCT-600) for up to 720 hours with periodic removal for visual inspection. Although both pigmented and non-pigmented (containing only solvent) coatings were subjected to the same exposure conditions the resulting corrosion behaviors were somewhat dissimilar. Figure 4.20 compares α-I, β-II, and γ-III-coated panels following 72 hours of exposure where it is seen that the extent and type of corrosion varies between the samples. All panels reveal reddish-brown corrosion products within the regions of the scribe only while γ-III is marked with small black spots all throughout the steel surface at the coating-substrate interface. It is very likely that these are magnetite (Fe_3O_4) formations due to the black appearance while the reddish-brown corrosion products which formed within the scribed areas panels are various hydrated ferric oxides (Fe_2O_3, "rust"). Additionally, the β-II coating exhibited slight whitening of film area immediately surrounding the scribe mark while γ-III displayed more extensive discoloration which stretched further outward from the demarcation. These findings are indicative of the variability in both the water

sorption amounts and the respective amounts of strain each network experiences following exposure.

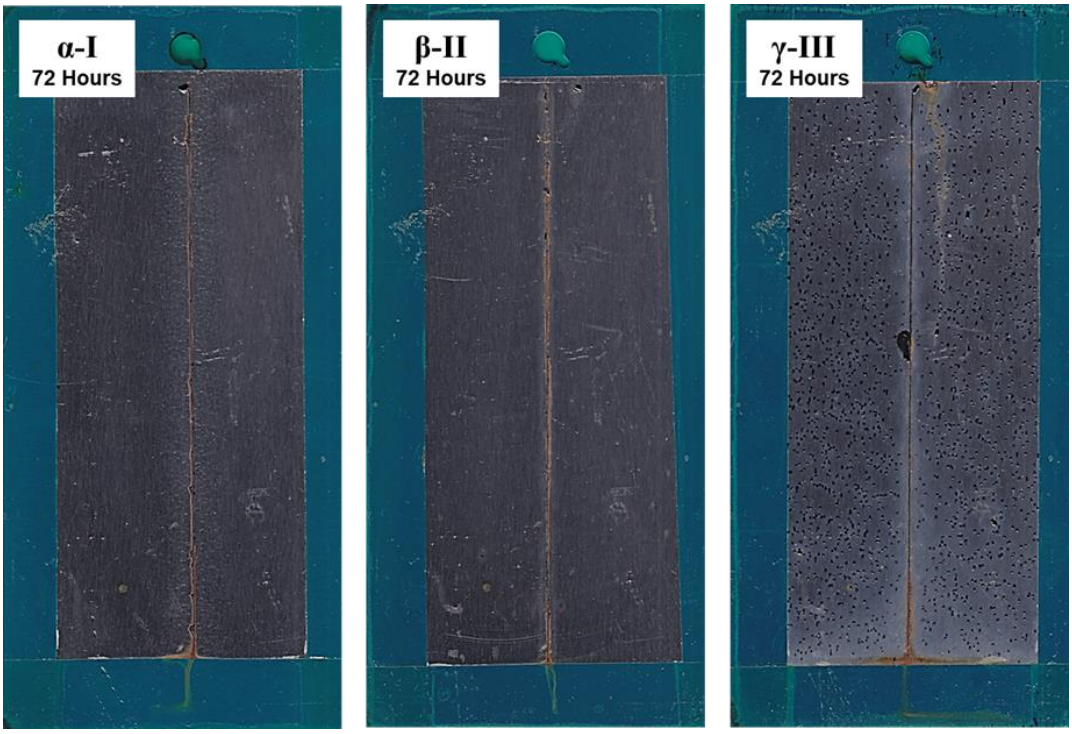

Figure 4.20 Comparison of NS2 non-pigmented film corrosion protection following 72 hours of exposure to ASTM B117 salt fog testing.

Although less stable in air than typical Fe_2O_3-type rust formations, magnetite has been shown to form under conditions of continuous wetting whereby the electrochemical oxidation conditions necessary for rust formation do not develop.[19] This suggests that the amount of moisture present within the γ-III coating is sufficient to form a continuous layer of water within the interface between polymer and metal, potentially displacing points of coating adhesion. As discussed in Chapter III the occupation of free volume pores within the polymer can also potentially exclude the transport of oxygen unless significant swelling occurs whereby the free volume hole size can increase (which is

limited in the case of a substrate-bound film). A similar disparity in panel corrosion condition was exhibited by the pigmented coatings following approximately 720 hours of salt fog testing as seen in Figure 4.21.

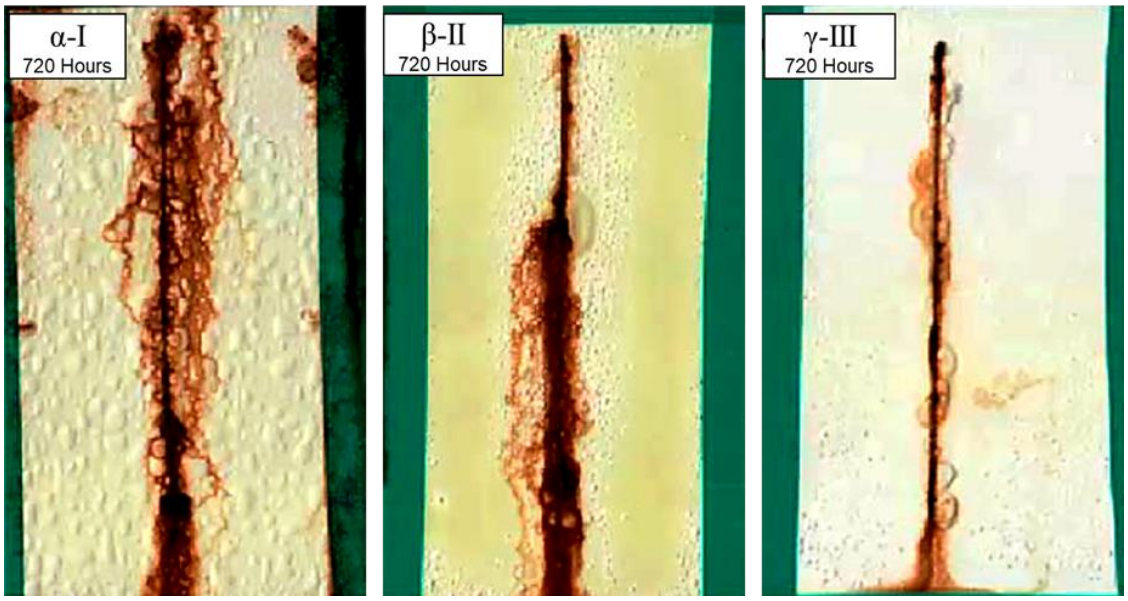

Figure 4.21 Comparison of NS2 pigmented film corrosion protection following 720 hours of exposure to ASTM B117 salt fog testing.

One of the more apparent differences between systems was the discoloration of the coatings from a yellow hue (due to the presence of corrosion inhibitor $SrCrO_4$) to white (TiO_2). The extent of discoloration increases with the amount of network water sorption (α-I < β-II < γ-III) which suggests that modifying this property has a prevailing impact on inhibitor dissolution and release. Interestingly, both α-I and γ-III exhibit consistent coloration across the entire coating area while β-II only reveals a differential in yellow to white transition adjacent to the scribe area, indicating a release of inhibitor only in localized regions. Likewise, the development of blisters is only apparent near the coating damage region while α-I and γ-III developed formations throughout the entirety

of the exposed areas with an inverse relationship between the size of blister and network moisture sorption quantity. Although the extent of iron oxide formation seems to decrease from α-I to γ-III this may be due to either more extensive inhibition from $SrCrO_4$ release or higher rates of corrosion product transport away from the scribe region following iron oxidation.

4.3.5.4 Network Heterogeneity and Impact on Coating Transport Properties.

While developing the network series formulations it was found that diversity in reaction kinetics of the individual matrix components could potentially lead to inhomogeneous network formation as observed via DMA. By adjusting the order of monomer addition and processing the resulting samples of NS1 β-II could present either a single glass transition peak, as shown in Figure 4.22, or a bimodal peak centered around the same temperature region and with an identical transition breadth. The difference between these two networks originated from the addition of all amine components to the epoxy resin at the same time (bimodal) as compared to the pre-reaction between chain extender and epoxy prior to introduction of the crosslinking agents (unimodal). The samples (free films/bars) procured from these methods did not exhibit any visual indication of phase separation such as color change or cloudy appearance, suggesting that the extent of network heterogeneity was either very slight or occurred on a small scale.

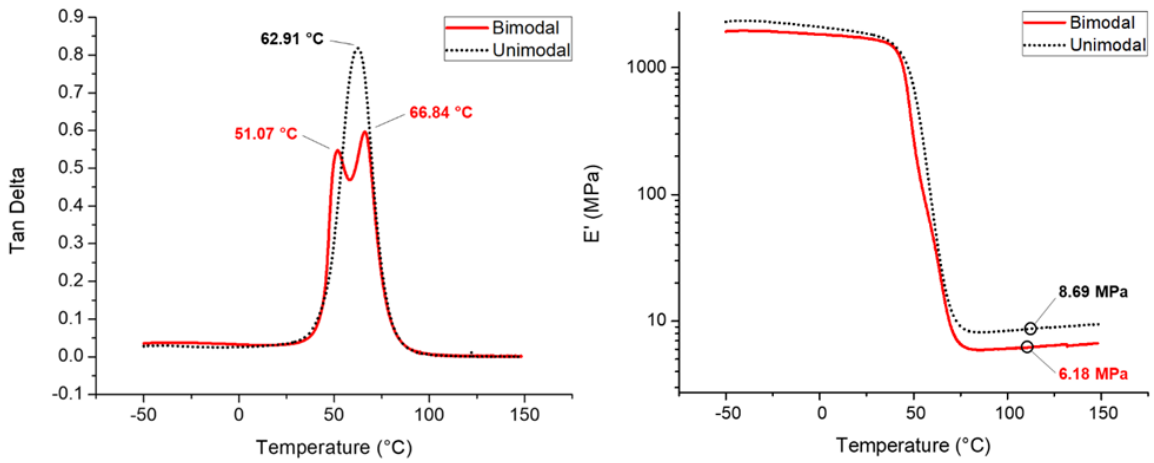

Figure 4.22 DMA thermographs of NS1 β-II free films presenting variability in thermomechanical properties based on network formation differences.

This is confirmed by the presence of a dual peak in the DMA tan δ signal that otherwise overlaps with the unimodal sample while the E′ signals for the two networks are very similar. However, within the post-T_g rubbery plateau region it is observed that a slightly lower modulus value found with regard to the bimodal matrix. Provided that the sample densities of the two networks are similar, this would indicate that the crosslink density is lower than that of the homogeneous network. Considering that DSC tests of prepared samples did not reveal any residual exothermal peaks post-T_g it is likely that this variability in crosslink density resulted from an inhomogeneous topological connectivity that arises from the differences in reactivity towards epoxy of the different amine components. Contemporary theory of epoxy-amine networks suggests that microgel formation and development occurs during early stages of the matrix followed by connection and extensive growth over long ranges at later stages, all of which could be impacted by mixing of two or more co-reactants each with variable reactivity.[20-21]

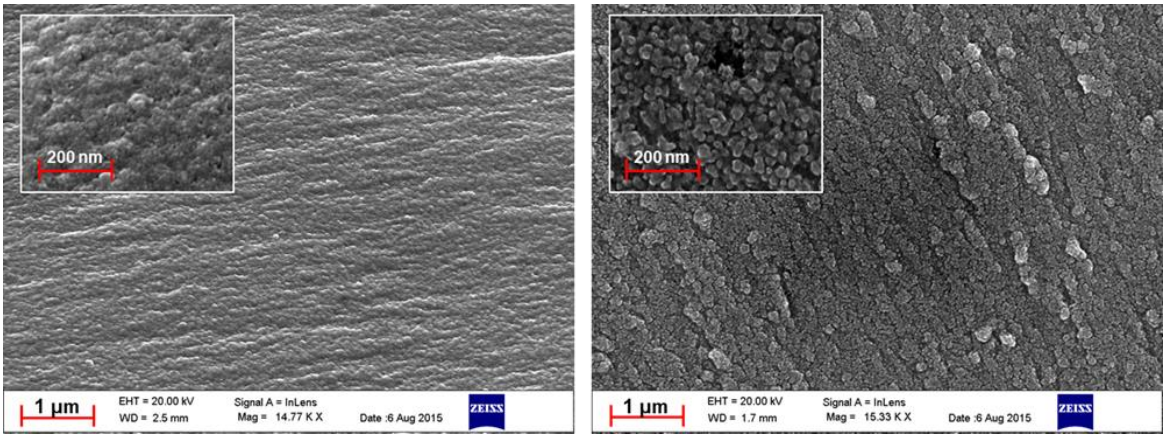

Figure 4.23 SEM micrographs of NS1 β-II unimodal (left) and bimodal (right) samples detailing the differences in fracture surface morphologies.

Scanning electron microscopy confirmed the assumption of small-scale network heterogeneity (Figure 4.23) with a comparison of the cryogenically fractured surfaces of bimodal and unimodal samples revealing a stark contrast in topological connectivity. The NS1 β-II bimodal network is found to consist primarily of well-defined rounded nodules approximately 20-50 nm in diameter, some of which organize into less defined larger bodies within the range of 100-300 nm (mesoscale). The unimodal network sample exhibits a much smoother fracture surface with poorly defined domains on the nanoscale only which indicates a more interconnected matrix structure compared to the bimodal material. It could be expected that an inhomogeneous distribution of crosslink junctions and hydrophilic functional groups would have some influence on transport properties which is confirmed by water sorption measurements as seen in Figure 4.24. It is observed that the film consisting of the heterogeneous network microstructure absorbs more water (46.15% higher moisture content at saturation) at a faster rate (24.59% higher H_2O diffusivity) than the homogeneous matrix, most likely due to more access of

penetrant to interconnected free volume cavities and hydrophilic sites as compared to the unimodal material.

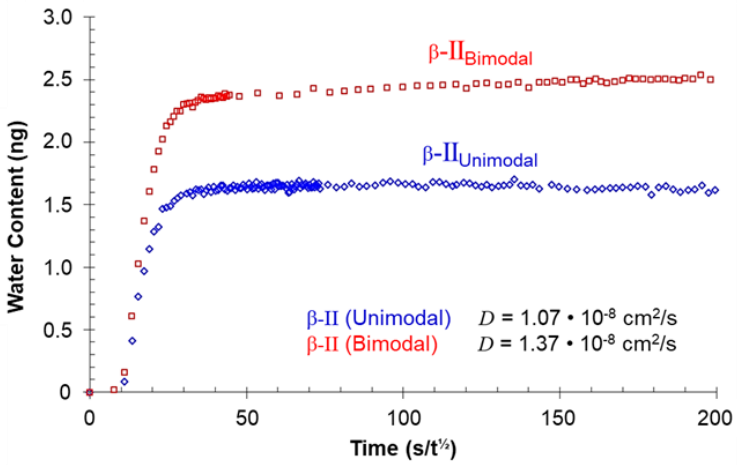

Figure 4.24 Comparison of water sorption behaviors of unimodal and bimodal network variations of β-II free film samples as measured via ATR-IR.

Both network forms were developed into fully formulated primers according to the same methods and quantities of materials as described above, including TiO_2 and $SrCrO_4$ pigments. These were again applied to steel panel substrates and, once dried and cured, immersed in separate containers of deionized water for up to three days at which point aliquots of the immersion solution were obtained and evaluated for chromium (Cr) content via inductively coupled plasma mass spectroscopy (ICP-MS) analysis provided by Bonner Analytical (Hattiesburg, MS). As demonstrated in Figure 4.25 the coating composed of the heterogeneous binder matrix released higher quantities of inhibitor ions into the environment as determined from the amount of Cr content within the leachant when compared to the homogeneous network-containing primer, with nearly twice the amount of Cr detected within the immersion solution after three days (9.1 vs 17.8 PPM).

This provides an additional correlation between increased rates and amounts of moisture transport to enhanced dissolution and release of incorporated corrosion inhibitor.

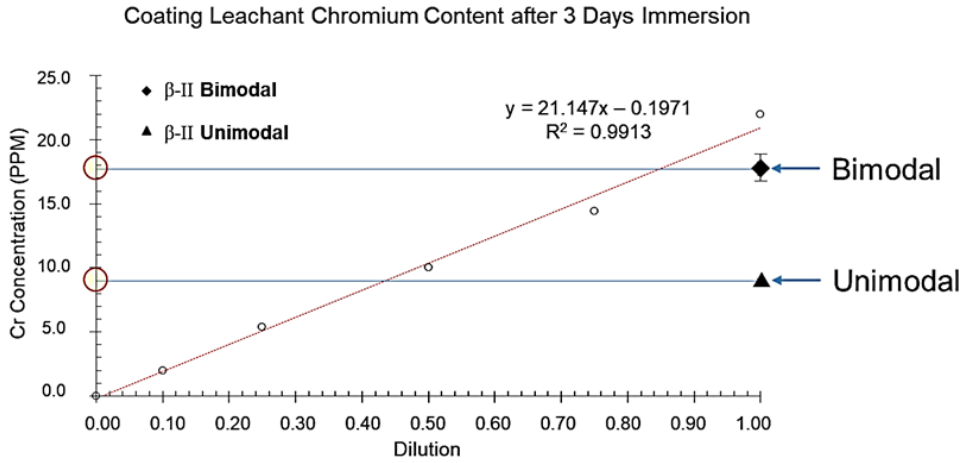

Figure 4.25 Comparison of chromium detected via ICP-MS in the leachant of coatings immersed in 5 wt% NaCl solution after three days and the respective calibration curve.

However, with the increase in small molecule transport properties the propensity for decreased overall barrier efficiency should not be overlooked. This is highlighted in the post-exposure analysis of pigmented primers following 175 hours of neutral salt spray ASTM B117 salt fog testing of steel panels coated with unimodal and bimodal-containing coatings shown in Figure 4.26.

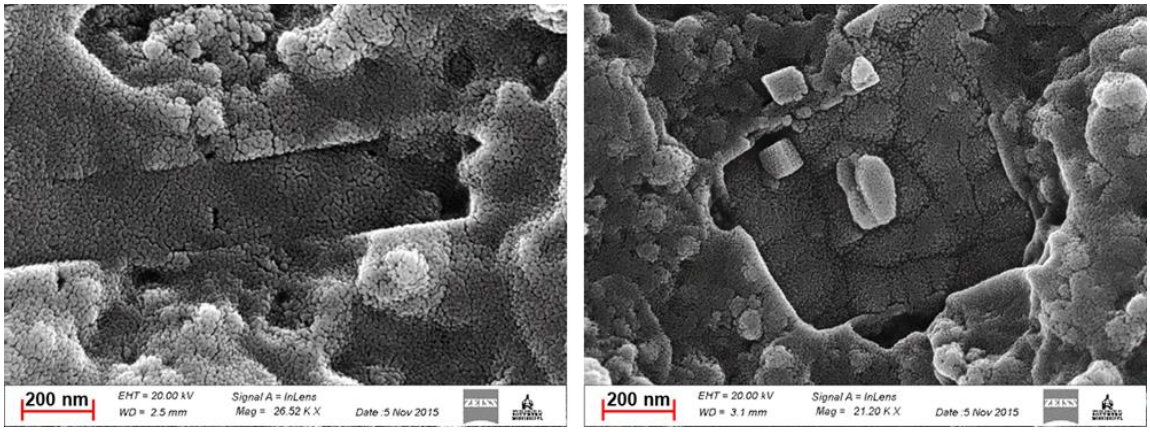

Figure 4.26 SEM micrographs of NS1 β-II pigmented coatings formulated from unimodal (left) and bimodal (right) networks following exposure to 175 hours of ASTM B117 salt fog testing.

SEM analysis of these exposed coatings emphasizes the dissimilar transport properties of topologically homogeneous and heterogeneous matrices. When comparing the pigmented primer microstructure of samples obtained from areas near scribe marks, it can be seen that coating produced from the inhomogeneous network displays a greater extent of creases and protuberances similar to those found in the bulk polymer micrographs. This could impact the dispersion efficiency of pigment particles and potentially be responsible for enhanced small molecule transport by acting as channels for penetrant movement. Additionally, deposited cubic salt crystals attest to the increased transport rates of corrosive contaminants along with water molecules and inhibitor ions. Although the development of a heterogeneous matrix structure assists in the dissolution and release of corrosion inhibitor the resulting decrease in barrier properties to other small molecules, namely oxygen and salt ions, would likely negate any benefit. However, this simple comparison does not account for all potential forms of phase

separation and more extensive isolation of hydrophilic polymer regions could have further impact on transport and barrier properties.

4.4 Conclusions

These series of networks were designed to serve as a tool for developing an understanding of how epoxy-amine matrix properties impact water transport behaviors, the relationship between transport and thermomechanical phenomena, and the resulting influence over inhibited primer corrosion protection efficacy. Rather than developing a collection of networks derived from dissimilar monomeric components to provide a range of structural and compositional features, the approach discussed here revolved around using a mixture of amine reactants with disparate functionality, molecular mass, and concentration of hydrophilic functional groups for all matrices. When combined with an epoxy resin in different pragmatically determined ratios, the crosslink density, T_g, and water sorption/transmission characteristics were shifted iteratively to produce a number of distinct epoxy-amine networks, all of which maintained a 1:1 epoxy:amine-hydrogen stoichiometry and satisfied one of three specific M_c and amine equivalent proportion targets for a total of nine systems. From these formulations bulk and free film samples were produced and subjected to a range of experiments which allowed for comparison of water transport characteristics and thermomechanical property shifts as a function of the structure-property relationships and application form, i.e., solution versus bulk.

The resulting network glass transition temperatures ranged between approximately 55-95 °C (DMA) or 35-80 °C (DSC) and were found to absorb between 2.5-5.7 wt% moisture at 95% RH at diffusion rates of roughly 8-35 · 108 cm^2/s at 25 °C and ambient pressure. Water vapor transmission rates exhibited a spread along the same

lines (1.6-7.4 · 107 mg/min·mm^2) and within each of these properties a trend became apparent of increasing amounts and rates of transport from low to high hydrophilic crosslinking agent content in addition to increasing crosslink density. This is to be expected given that the epoxy-amine crosslink junction consists of a collection of hydrogen bonding functional groups (a tertiary amine and two secondary hydroxyls per crosslink junction) in a relatively small molecular volume and increased crosslink density has been correlated with an increase in free volume fraction.12

However, what was not anticipated was the extent to which Tg decrease was dependent upon the original dry/unexposed glassy state rather than the total amount of water absorbed. Specifically, the degree of T_g depression increased from $\gamma < \beta < \alpha$ while the total amount of water sorption at 95% RH decreased from $\gamma > \beta > \alpha$, which indicated that the higher glassy state is more sensitive to physical property depression upon hydroplasticization. A novel method of measuring swelling-induced strain during exposure to a controlled RH environment (RH-DMA) was employed and found to agree with these findings when each network sample was normalized by the amount of water sorption. Interestingly the β series of formulations (mid-T_g, mid-water sorption amounts) revealed a decreased or lesser extent of shift in physical property than the extremes. Physical aging experiments in both wet and dry conditions indicated that the presence of moisture hinders the process of aging-related processes by occupying molecular volume necessary for polymer relaxation. Additionally, it was observed that an optimal range of crosslink density (M_c > 600 g/mol) and hydroplasticized glass transition temperature (10-20 °C above exposure temperature) resulted in greater extents of physical aging due to

proximity to glassy equilibrium states and molecular mobility necessary for rearrangement.

Further spectroscopic evaluation of water-polymer interaction of substrate-bound pigmented coatings derived from a selection of these networks (α-I, β-II, and γ-III) and from the substrate interface perspective allowed for interpretation of water-polymer interaction as a function of matrix structural and compositional features. Following introduction of a 5 wt% NaCl solution to the top of the coatings the presence of moisture via ATR-IR was measured as a function of time, solution salt concentration, at saturation, and after several dry/wet cycles. Subtracted and normalized –OH stretch peaks were interpreted in such a way as to determine the extent of molecular association between the matrix and water molecules. The coatings exhibited very small proportions of free/unbound water molecules regardless of polymer T_g/M_c/water sorption content while a definitive trend existed in increasing S_1 (singly hydrogen bound) and decreasing S_2' (loose doubly hydrogen bound) populations as overall moisture sorption increased, which is indicative of greater water molecule mobility. This trend also correlated with decreasing T_g and increasing crosslink density from α-I to γ-III with more substantial increases in S_1 proportions than the observed S_2' population reduction. It could be assumed that this development stemmed from a higher concentration of hydrophilic functional groups contributed by both the hydrophilic ED600 and the crosslink junctions in combination with heightened chain mobility.

Similarly, multiple salt solution application and drying cycles revealed the extent to which sorption behaviors shift during subsequent exposures. Each coating formulation exhibited an increase in the rate and amount of solution sorption between the first,

second, and third cycles although the extent of these shifts varied extensively. The greatest degree of shifting transport properties (diffusion rate and sorption quantity) were expressed by the coating composed of the α-I matrix with the highest glass transition temperature and lowest crosslink density, suggesting that these factors predominantly contribute to the extent to which microstructural reorganization takes place while in the glassy state upon the sorption and saturation of water. The coating derived from γ-III exhibited the least amount of drift in water transport behaviors between cycles which indicates that the lower glass transition temperature (within 25 °C of the testing/exposure temperature) undergoes significantly less relaxation following moisture ingress despite absorbing substantially more water than the other coatings and consisting of a higher crosslink density matrix.

Steel substrate-bound coatings, both pigmented and non-pigmented, were subjected to accelerated corrosion conditions in neutral salt spray testing. The non-pigmented test panels exhibited an increase in the extent to which the polymer regions directly surrounding the scribe mark appeared to whiten along with the amount of corrosion product development within the scribe. Furthermore, the coating with the highest water sorption (γ-III) revealed the production of under-film magnetite (Fe_3O_4) formations, signifying that a substantial quantity of water at the coating-substrate interface catalyzes the degradation of steel but also limited oxygen availability which prevented the further oxidation into ferric oxide (Fe_2O_3) and its hydroxides and hydrates. Pigmented coatings containing $SrCrO_4$ corrosion inhibitors demonstrated similar trends in that discoloration of the epoxy-amine primer following exposure increased with the degree of matrix water sorption which indicated greater extents of chromate dissolution

and release. The development of large and small blisters in α-I and γ-III coatings are likely associated with the extensive shift in physical state and displacement by water of polymer at the substrate, respectively.

Finally, a method of heterogeneous network development was pursued and the resulting materials were evaluated via electron microscopy along with thermomechanical and moisture sorption analysis. Fully formulated and inhibited coatings were developed utilizing either heterogeneous or homogeneous epoxy-amine matrices for the binder component, applied to steel substrates, and immersed in electrolyte solution. It was determined that the increase in transport properties afforded by the microstructural inhomogeneity resulted in faster chromate inhibitor leaching rates but also allowed for more rapid accumulation of salt within the coating, which could potentially result in more extensive corrosion at longer periods of exposure. Taken in concert these findings demonstrate the potential to modify coating protection efficacy through manipulation of the polymeric structural and composition properties without introducing new monomeric or network component species. By adjusting the T_g, M_c, hydrophilic crosslinking agent fraction, and microstructural homogeneity the water sorption and transmission behaviors were varied extensively. The relationship between transport and thermomechanical properties was assessed in addition to the contribution of these characteristics to aging processes and coating performance in accelerated weathering. Based on these results it could be posited that a balance of mechanical resilience and heightened moisture transport would provide for a more effective inhibited primer. It is hypothesized that an inhibited epoxy primer would most benefit from a glass transition temperature of approximately 40-50 °C above the anticipated average exposure temperature, molecular

mass between crosslinks value of anywhere between 400 and 1000 g/mol, and moisture sorption/solubility of 3-5 wt% (with nearly equal proportions of S_1 to S_2' water types for maximum small molecule mobility) for optimal balance of inhibitor release and barrier integrity.

4.5 References

1. Soles, C. L.; Chang, F. T.; Bolan, B. A.; Hristov, H. A.; Gidley, D. W.; Yee, A. F., Contributions of the nanovoid structure to the moisture absorption properties of epoxy resins. *J. Polym. Sci., Part B: Polym. Phys.* **1998**, 36, 3035-3048.
2. Soles, C. L.; Chang, F. T.; Gidley, D. W.; Yee, A. F., Contributions of the nanovoid structure to the kinetics of moisture transport in epoxy resins. *J. Polym. Sci., Part B: Polym. Phys.* **2000**, 38, 776-791.
3. Linde, E.; Giron, N. H.; Celina, M. C., Water diffusion with temperature enabling predictions for sorption and transport behavior in thermoset materials. *Polymer* **2018**, 153, 653-667.
4. Wicks, Z. W., Jr.; Jones, F. N.; Pappas, S. P., *Organic Coatings: Science and Technology, 2nd Ed*. Federation of Societies for Coatings Technology: **1999**; Vol. 71, p 67-73.
5. Mueller, B., *Coating Technology - BASF Handbook*. Mater. Corros. **2003**, 54, 812.
6. Perera, D. Y., Physical ageing of organic coatings. *Prog. Org. Coat.* **2003**, 47, 61-76.
7. Guo, J. H.; Robertson, R. E.; Amidon, G. L., Influence of physical aging on mechanical properties of polymer free films: the prediction of long-term aging

effects on the water permeability and dissolution rate of polymer film-coated tablets. *Pharm. Res.* **1991**, 8, 1500-4.

8. Perera, D. Y., Effect of thermal and hygroscopic history on physical ageing of organic coatings. *Prog. Org. Coat.* **2002**, 44, 55-62.

9. Pramanik, M.; Fowler, E. W.; Rawlins, J. W., Another look at epoxy thermosets correlating structure with mechanical properties. *Polym. Eng. Sci.* **2014**, 54, 1990-2004.

10. Fieldson, G. T.; Barbari, T. A., The use of attenuated total reflection FTIR spectroscopy to characterize penetrant diffusion in polymers. *Polymer* **1993**, 34, 1146-53.

11. Cotugno, S.; Larobina, D.; Mensitieri, G.; Musto, P.; Ragosta, G., A novel spectroscopic approach to investigate transport processes in polymers: the case of water-epoxy system. *Polymer* **2001**, 42, 6431-6438.

12. Frank, K.; Childers, C.; Dutta, D.; Gidley, D.; Jackson, M.; Ward, S.; Maskell, R.; Wiggins, J., Fluid uptake behavior of multifunctional epoxy blends. *Polymer* **2013**, 54, 403-410.

13. Croll, S. G.; Shi, X.; Fernando, B. M. D., The interplay of physical aging and degradation during weathering for two crosslinked coatings. *Prog. Org. Coat.* **2008**, 61, 136-144.

14. Sun, Q., Local statistical interpretation for water structure. *Chem. Phys. Lett.* **2013**, 568-569, 90-94.

15. Marechal, Y., The molecular structure of liquid water delivered by absorption spectroscopy in the whole IR region completed with thermodynamics data. *J. Mol. Struct.* **2011**, 1004, 146-155.

16. Max, J.-J.; Larouche, P.; Chapados, C., Orthogonalyzed H_2O and D_2O species obtained from infrared spectra of liquid water at several temperatures. *J. Mol. Struct.* **2017**, 1149, 457-472.

17. Sutandar, P.; Ahn, D. J.; Franses, E. I., FTIR ATR analysis for microstructure and water uptake in poly(methyl methacrylate) spin cast and Langmuir-Blodgett thin films. *Macromolecules* **1994**, 27, 7316-28.

18. Bouvet, G.; Cohendoz, S.; Feaugas, X.; Touzain, S.; Mallarino, S., Microstructural reorganization in model epoxy network during cyclic hygrothermal ageing. *Polymer* **2017**, 122, 1-11.

19. Nasrazadani, S.; Raman, A., Formation and transformation of magnetite (Fe_3O_4) on steel surfaces under continuous and cyclic water fog testing. *Corrosion* (Houston) **1993**, 49, 294-300.

20. Sahagun, C. M.; Morgan, S. E., Thermal Control of Nanostructure and Molecular Network Development in Epoxy-Amine Thermosets. *ACS Appl. Mater. Interfaces* **2012**, 4, 564-572.

21. Vidil, T.; Tournilhac, F.; Musso, S.; Robisson, A.; Leibler, L., Control of reactions and network structures of epoxy thermosets. *Prog. Polym. Sci.* **2016**, 62, 126-179.

CHAPTER V - INVESTIGATING THE ROLE OF MATRIX HYDROPHILICITY IN THE PERFORMANCE OF INHIBITED PRIMERS

5.1 Introduction

In an anticorrosive multilayer coating system, the top coat provides the aesthetics and serves as the first barrier against environmental factors such as humidity and UV radiation, while the primer provides adhesion to the substrate and is formulated with corrosion inhibitor pigments.[1] Water ingress through the topcoat and primer solubilizes the inhibitor pigment, releasing inhibitor ions that block the anodic and/or cathodic pathways of the redox corrosion reaction, and minimize substrate corrosion. Historically, chromates have been favored for use as corrosion inhibitors as they are capable of mixed inhibition, i.e., their constituent ions interfere with both the anodic and cathodic pathways. Strontium chromate salts also possess nearly ideal water solubility characteristics to meet the substrate quickly without much waste; they exhibit low solubility in water (< 0.2 g/100 mL) but are practically insoluble in the polymer.[2] It is widely acknowledged that hexavalent chromium-based corrosion inhibitors pose a threat to the environment as they are highly toxic, mutagenic, and carcinogenic.[3] Compounds intended to replace chromates, commonly termed chromate-replacement inhibitors (CRIs), have not exhibited the potential to effectively replace chromates in all coating functions. For many military and aerospace applications, chromate pigments continue to serve as the corrosion inhibitor of choice in many primer formulations.[4]

In addition to the electrochemical nature of the pigment, the effectiveness of corrosion inhibiting pigments is partly dependent upon the ability of the constituent ions to reach the substrate.[4] Since the solubilization and mobility of inhibitor ions is driven by

the presence of water, it follows that the rate and mode of water uptake would influence the coating's ability to inhibit corrosion. If water uptake is too high, the inhibitor concentration would be depleted rapidly, thus reducing the coating longevity, moreover, the ions could cause delamination via osmotic pressure build-up.[5] If water uptake is too low, an insufficient quantity of inhibitor ions may diffuse, or they may diffuse too slowly to inhibit corrosion.[6] Additionally, increasing water sorption could potentially lead to greater corrosive ion mobility, leading to enhanced corrosion rates and therefore a careful balance must be struck. Currently, epoxy-amine formulations are based on various processing and performance needs, and an understanding of water transport is not of great concern, save for the study and usage of extremely hydrophobic or hydrophilic coatings. The ability of an organic coating to take in water and transport solute depends on both the structure and composition of the polymer and, although studied extensively, is still not well understood. In epoxy-amine networks, water uptake is mostly determined by the crosslink density of the network and the hydrophilicity of the network components.[7-9] By adjusting the network structure, it is possible to influence drastic changes in crosslink density and hydrophilicity of the final coating. Crosslink density depends on the molecular weight, functionality, and chemical structure of the curatives, while hydrophilicity depends on the type and concentration of polar groups on the polymers.

Altering the hydrophilicity of a given epoxy-amine matrix should influence the water sorption and transport behavior and also determine the rates of inhibitor dissolution. However, epoxy-amine networks pose a unique challenge in that shifting any compositional features directly related to hydrophilicity/solubility also impacts structural characteristics which will inherently further affect transport characteristics.

This has been demonstrated in a multitude of studies wherein the utilization of an epoxy network series provides a means for elucidating polymer structure-property relationships and their influence on water transport behaviors.[10-12] Often these series will consist of networks that differ in reactant stoichiometry, extent of cure, functionality, or molecular weight. Given that the most hydrophilic molecular components of epoxy-amine networks are the crosslink junctions that consist of localized secondary hydroxyls and tertiary amines, modifying any aspect of the these structural features will directly impact polymer polar/hydrogen bonding group concentration.[13] An example of this condition is illustrated by Figure 5.1 whereby alteration of model epoxy-amine network crosslink densities results in vastly different concentrations of hydrophilic moieties per unit area. Specific formulation considerations must be employed to create a series which varies in compositional features without also shifting structural characteristics.

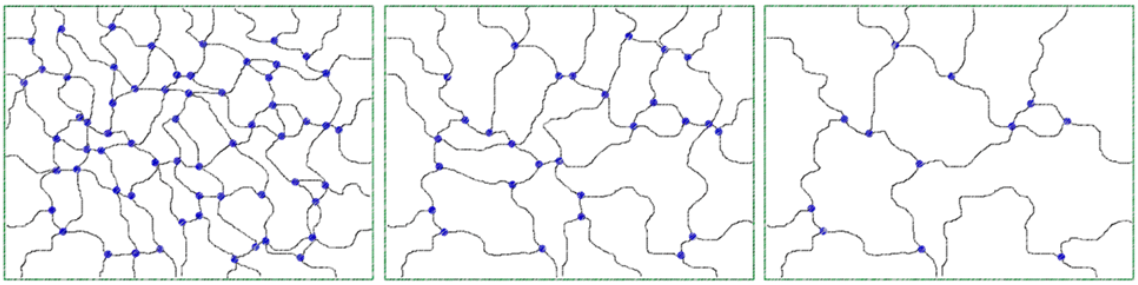

Figure 5.1 Comparison of concentration of hydrophilic regions (filled blue circles), composed of the secondary hydroxyl and tertiary amine groups found at the crosslink junctions, between epoxy-amine networks of varying crosslink density.

In the current study, a series of epoxy primers with quantifiably distinct solubility characteristics were designed via the use of various ratios of hydrophobic and hydrophilic amine curatives. To reduce the variability of water uptake resulting from disparate network architecture, only amine curatives of nearly equal molecular mass and size were

considered while pigment packages were selected to evaluate chromates against CRI pigments. DMA studies were employed to establish the differences in network parameters such as extent of cure, T_g, crosslink density, and molecular weight between crosslinks in addition to following shifts in thermomechanical properties upon sorption of water. DVS and water absorption studies were conducted to determine the water diffusion coefficients and compare uptake saturation levels. The coatings were tested for hardness, gloss, adhesion, and impact resistance, while corrosion resistance was evaluated via natural outdoor weathering and accelerated weathering testing with neutral salt spray (NSS) exposure according to ASTM B117. In addition to bulk polymer and model primer analyses a polyurethane top-coated multilayer system was formulated and the resulting corrosion protection performance was compared to other testing results. The subtle differences in the coating hydrophilicity resulting from the variable compositional ratios were expected to be reflected in varying levels of corrosion resistance and provide some insight into how polymer matrix composition might be used to influence inhibitor efficiency.

5.2 Experimental

5.2.1 Methodology

The network series implemented in this research was designed such that each epoxy-amine matrix exhibited the same structural or topological framework while iteratively shifting the compositional (hydrophilic) nature in small increments. This is made possible using two amine-functional polyethers (THF100 and ED900) of very similar molecular weight and length but dissimilar water solubility owing to the majority content of polytetramethylene oxide (THF100) or polyethylene oxide (ED900), as demonstrated in

Chapter III. Chemical structures of the network components and CRI are given in Figure 5.2.

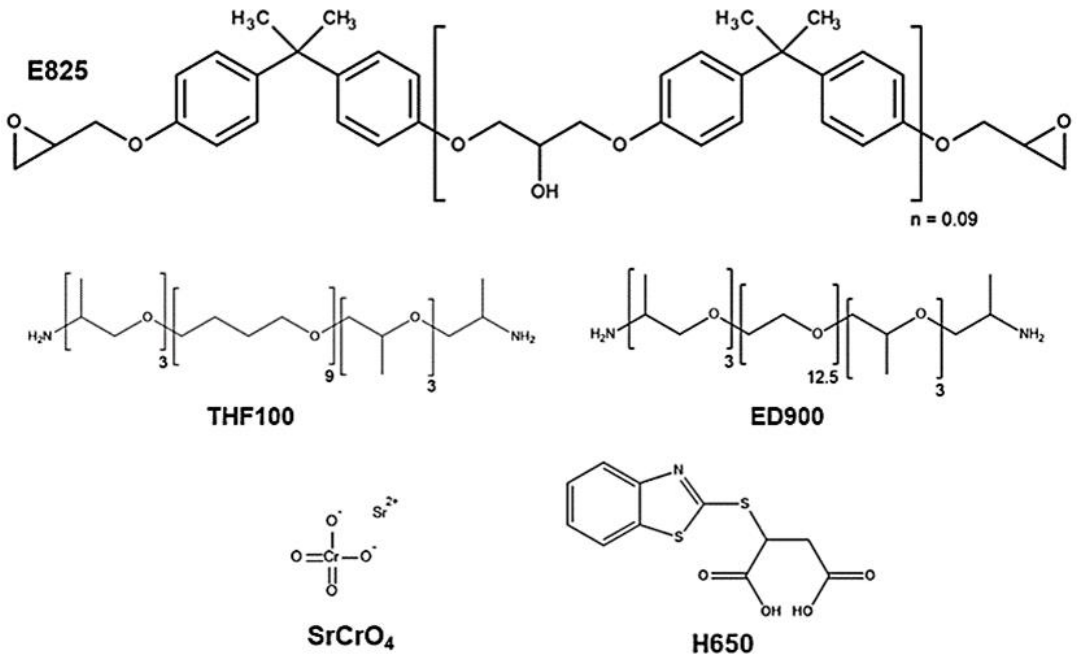

Figure 5.2 Chemical structures of epoxy resin, amine-functional polyethers, chromate-based inhibitor, and organic-type CRI pigment.

This series is constructed by formulating a 1:1 epoxy:amine-hydrogen network of E825 and a commercial polyamidoamine organic coating curative (Ancamide® 2445) which serves as a suitable host for the polyether modifiers while also acting as a glass-forming thermoset hardener that would find application in corrosion protection coatings. Approximately 15% of the amine-hydrogen equivalents of the polyamidoamine (as provided by the manufacturer-specified AHEW) is removed from the formulation and substituted with a mixture of THF100/ED900, the ratio of which determines the extent of hydrophilic nature, as demonstrated in Figure 5.3. Five separate modifier ratios were chosen for most analyses (THF90-ED10, THF75-ED25, THF50-ED50, THF25-ED75,

THF10-ED90) while an abbreviated series (THF90-ED10, THF50-ED50, THF10-ED90) was implemented in select characterizations and coatings evaluations. Adjusting the ratio of polyether amines should have very little impact on structural variability given the similarity in molecular weight and length of the two.

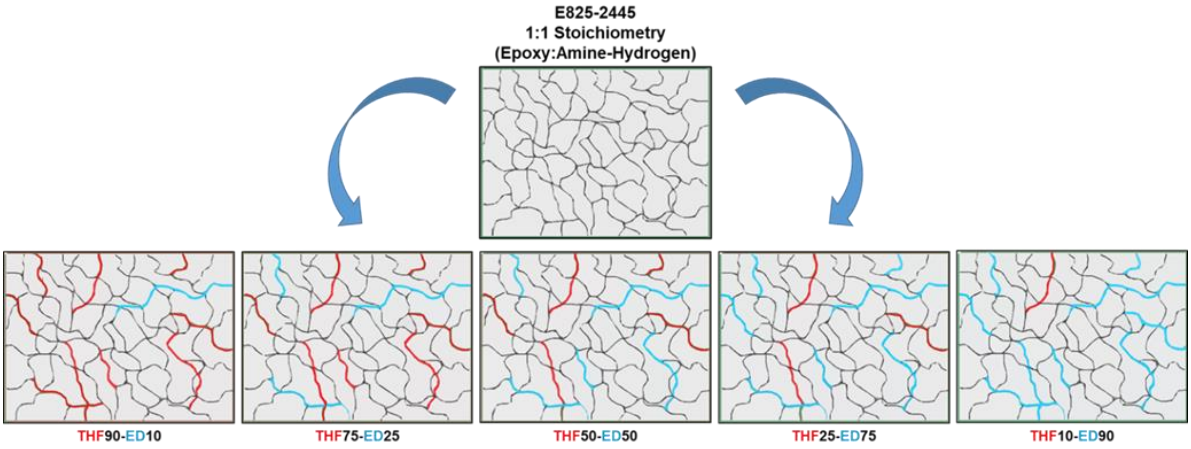

Figure 5.3 Design of Chapter V & VI epoxy-amine network series with controlled matrix hydrophilicities.

A theoretical 15 eq% of the amine crosslinking content of an E825-2445 network (1:1 epoxy:amine-hydrogen stoichiometry) is replaced by a mixture of hydrophilic (ED900) and hydrophobic (THF100) diamine crosslinkers, the ratio of which determines the overall network hydrophilicity while maintaining 1:1 stoichiometry

5.3 Results and Discussion

5.3.1 Bulk Polymer Characterization

An attempt to quantify the characteristic differences of in network solubility utilized the Hoftyzer-Van Krevelen group contribution theory for Hansen Solubility Parameter development (HSP, δ).[14-16] The method provides estimates of the dispersion (δ_d), polar (δ_p), and hydrogen bonding (δ_h) components which contribute to an average HSP value (δ_{total}, otherwise known as the Hildebrand Solubility Parameter) and are given by the following equations:

$$\delta_{dispersion} = \frac{\sum n_i F_{di}}{V}$$

$$\delta_{polar} = \frac{\sqrt{\sum n_i {F_{pi}}^2}}{V}$$

$$\delta_{h-bonding} = \frac{\sqrt{\sum n_i E_{hi}}}{\sqrt{V}}$$

$$\delta_{total} = \sqrt{{\delta_d}^2 + {\delta_p}^2 + {\delta_h}^2}$$

whereby n_i corresponds to the number of specific functional groups per average network unit (without accounting for cure/conversion), V is the material volume, and F_{di}, F_{pi}, and E_{hi} represent specific functional group values in $(MJ/m^3)^{½}$/mol or J/mol as per the group contribution theory.[15] Differences between the various matrix dispersion, polar, hydrogen-bonding, and total HSP value estimates are illustrated in Figure 5.3.

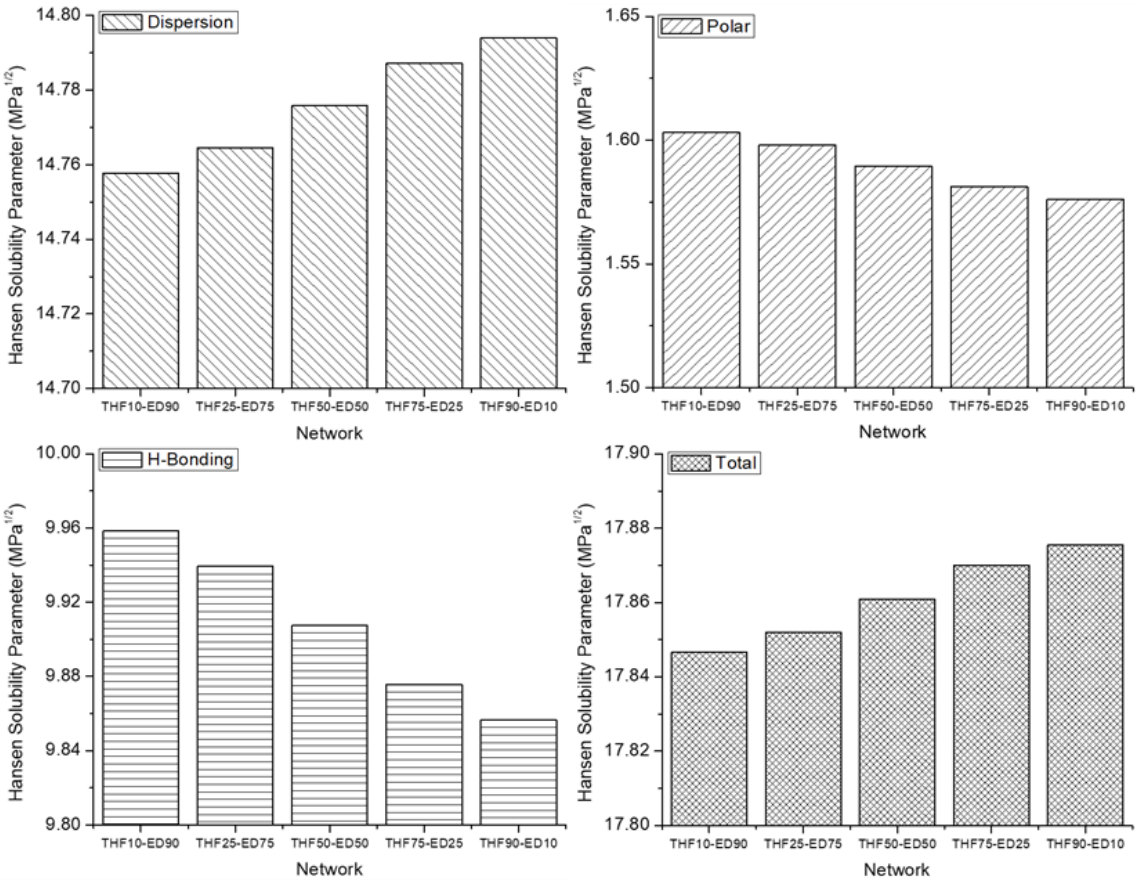

Figure 5.4 Calculated total Hansen Solubility Parameter component values based on average network unit structures and group contribution theory from the building block basis.

It can be seen in each of the solubility components that altering the THF10-ED90 ratio results in only slightly varied increments in the overall network solubility. The hydrogen bonding and polar parameters, which are correlated with polymer hydrophilicity, exhibit shifts by only approximately 0.1 and 0.02 MPa^{½}, respectively, between the modifiers ratio as the concentration is shifted from the mostly hydrophobic THF100-containing formulation to the predominantly hydrophilic ED900-containing network. The engineered shifts could potentially be explained by the relatively low concentration of the polyether content (accounting for only about 10% of the total network volume, i.e.

decreasing the 90% THF100 ratio to 75% results in only 0.10 * 0.15 = 1.5% increase in hydrophilic volume content). Additionally, group contribution theory may not fully account for the differences in hydrophilicity between varying polyether species (in this case polyethylene oxide [ED900] and polytetramethylene oxide [THF100]). Nevertheless, it was sufficient to reveal and exhibit calculated differences in matrix response to water and inhibitor uptake or transport to molecular composition in thermoset networks and establish the starting basis for macroscopic properties predictions through a relative comparison of interaction magnitude (i.e. polar, hydrogen bonding).

Water absorption of polymer bar sections (5 x 5 x 1 mm) was studied via gravimetric analysis of samples immersed in DI H_2O at ambient temperature. Periodically over the course of one month, samples were removed from the water, patted dry, and weighed. The relative change in weight due to water sorption (wt%) was calculated according to the expression:

$$Water\ sorption\ amount\ (wt\%) = \left(\frac{M_t - M_0}{M_0}\right) \times 100\%$$

where M_0 represents the sample weight in the dry state and M_t is the weight at time *t*. The resulting gravimetric uptake plots (Figure 5.5) reveal a gradient in both water sorption rates and saturation levels in the polymer samples derived from the network series. As the hydrophilic ED900 content fraction increased, so did the maximum amount of water taken on by the networks, ranging from 3.04% (THF90-ED10) to 5.57% (THF10-ED90). Slight increases in the slope of the initial (linear) region of the uptake plots suggested that increasing the hydrophilic ratio increases both the rate of water uptake and maximum of water sorption at saturation.

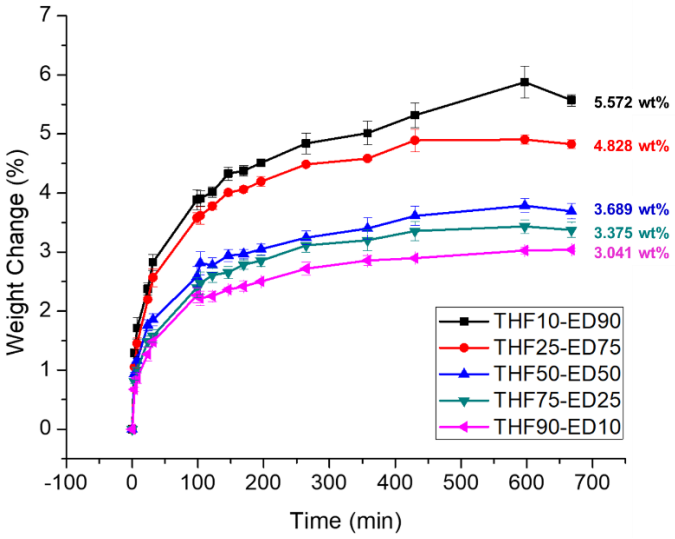

Figure 5.5 Gravimetric water uptake plots of the modified network series.

From the modified matrix series, three networks (low, medium, and high hydrophilicity) were selected for additional gravimetric analysis DVS to identify differences in liquid and gas-phase water transport behaviors. Samples were subjected to consecutive sorption/desorption cycles at 0 and 95% RH to the extent that equilibrium levels were reached as revealed in Figure 5.6. During the 0% RH step the networks equilibrated at 0.08, 0.07, and 0.25 wt% (for THF90-ED10, THF50-ED50, THF10-ED90, respectively) which indicates that some quantity of moisture is retained during the desorption process at 0% RH, which is similar to the findings of other investigations that report most epoxy-amine networks require long times at high temperatures and vacuum to completely remove all water.[17] These results suggest that quantity of "captured" (tightly bound or S_2'') water molecules may be dependent upon either the hydrophilicity of the polymer network or the amount of water present at saturation and less so on the chemical structure or architecture.

A wide array of epoxy-amine diffusion kinetics have been reported, with both Fickian (Case I) and non-Fickian characteristics (for example anomalous[18-19] or dual-mode sorption[20] mechanisms), with some apparent dependency on the exact combination of resin and curing agent, T_g and/or testing temperature, stoichiometry, degree of cure, solvent content, etc. However, to easily estimate the variability in water vapor sorption kinetics, the plots were treated as Fickian in nature, in which case the water uptake and diffusion process can be described via methods outlined in Chapter III.[21-22] Table 5.1 outlines the respective diffusion coefficients for each network from each sorption and desorption step. It can be seen that desorption diffusion rates suggest a substantially faster transport process than during sorption, which is often encountered in glassy epoxy thermosets.[23-24] The trend of increasing diffusivity from the most hydrophilic network to the least indicates that rates of transport is slowed by penetrant-polymer interactions, which would dominate the earliest stages of sorption.

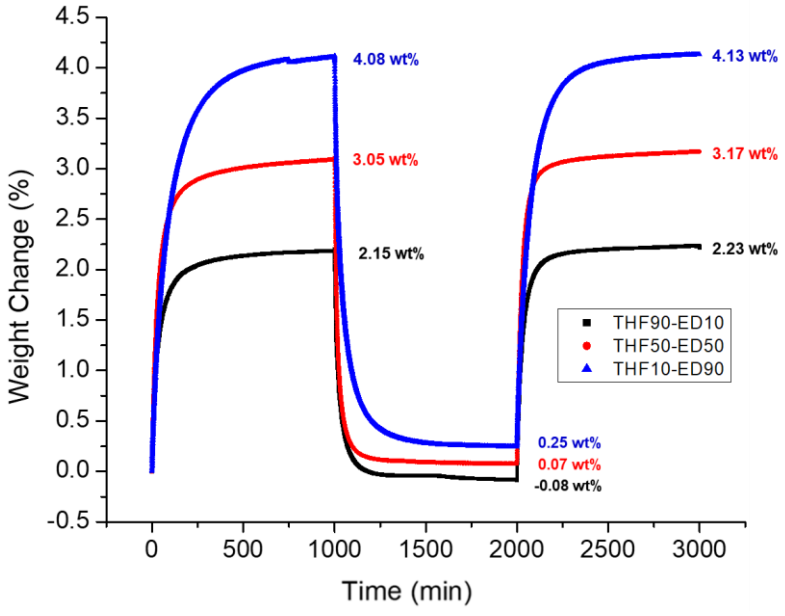

Figure 5.6 Water vapor sorption plots for select networks THF10-ED90, THF50-ED50, and THF90-ED10 through cyclic exposures to 95% and 0% RH.

The increase in diffusion coefficient from the first to second sorption cycles is a phenomena found in many epoxy-amine networks and has been attributed to a "homogenization" process whereby the hydroplasticized polymer becomes more relaxed and allows for more polar or hydrophilic sites to become exposed and interact with water upon subsequent moisture exposures.[25] As demonstrated in Figure 5.7, the difference in diffusion coefficient between the first and second 95% RH exposure cycle increases with greater THF100 content which would suggest that the initial uptake of moisture results in a microstructural relaxation that allows for some degree of separation between hydrophilic and hydrophobic polymeric regions. Upon additional sorption cycles the exposure of higher concentrations of polar and hydrogen bonding groups available as compared to the initial state manifests as a greater increase in water diffusivity. Interestingly, these data reveal a greater variance between the rate of water sorption of first and second cycles as polymer network hydrophilicity decreases (Figure 5.7). This may suggest that a higher water-polymer solubility allows for greater ingress into the matrix as well as within free volume pores and voids with more access of water molecules to polar and hydrogen bonding moieties. This increased availability of polymer sites to moisture may result in a comparatively muted response to sorption of water, i.e. microstructural reorganization, between multiple sorption and desorption cycles. It could be expected that a more significant shift in matrix transport properties during cyclic exposure conditions (e.g. diurnal or precipitation cycles) would result in more dramatic alterations in coating protection performance of the service lifetime of a given coating.

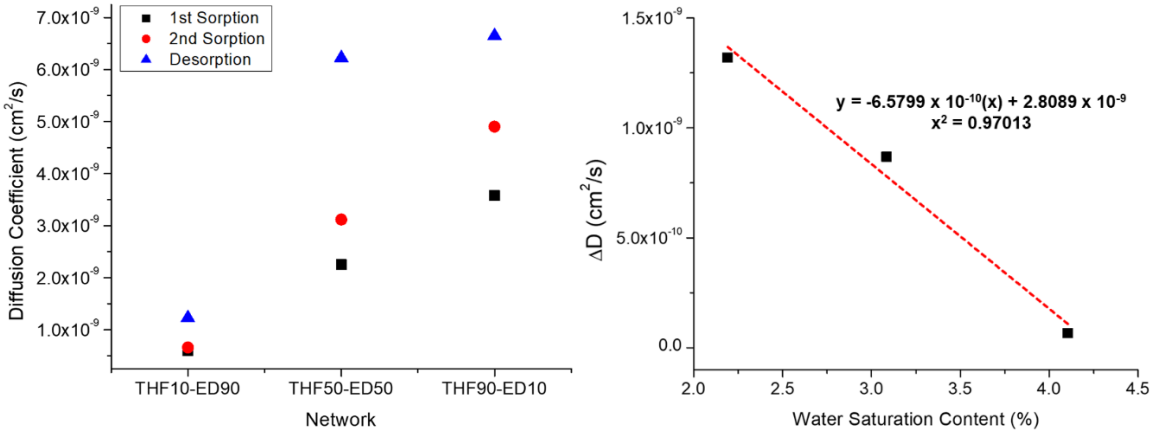

Figure 5.7 Diffusion coefficients of the modified epoxy-amine networks as interpreted from each sorption/desorption cycle (left) and relationship between the difference in calculated diffusion coefficients between first and second sorption cycles as a function of the average quantity of moisture content at saturation (right).

Although it has been suggested or demonstrated that some extent of polymer hydrolysis[26] or oxidation[27] upon sorption of water may occur in some epoxy networks, typically when combined with exposure to high temperatures, the trends shown here are not likely a result of any degradation given the mild ambient conditions under which the testing was carried out.

Table 5.1

Modified Matrices Dynamic Vapor Sorption Measured and Calculated Quantities

Formulation	**1st Sorption Cycle**	**2nd Sorption Cycle**	**Desorption Cycle**
	Water Content (wt%)		
THF10-ED90	4.08	4.13	0.25
THF50-ED50	3.05	3.17	0.07
THF90-ED10	2.15	2.23	-0.08
	Diffusivity (cm^2/s)		
THF10-ED90	$5.94 \cdot 10^{-10}$	$6.61 \cdot 10^{-10}$	$1.23 \cdot 10^{-9}$
THF50-ED50	$2.25 \cdot 10^{-9}$	$3.12 \cdot 10^{-9}$	$6.22 \cdot 10^{-9}$
THF90-ED10	$3.58 \cdot 10^{-9}$	$4.91 \cdot 10^{-9}$	$6.65 \cdot 10^{-9}$

The network series was designed with the intent of altering only the compositional element of the matrices, i.e. developing networks with higher or lower hydrophilicity while maintaining the same general network structure and connectivity. For this reason, DMA was used to investigate the various mechanical properties associated with these network characteristics, which can be interpreted within the framework of molecular architecture and glassy/rubbery dynamics. Figure 5.8 reveals a very narrow range of T_g values (average 57.84 ± 5.88 °C) as interpreted from the tan δ signal peaks. The slight increase in peak height and decrease in peak width of the samples as the ratio of polyether modifier ranges from 90% ED900 to 90% THF100 may be due to differences in flexibility of PEO and PTMO backbone units and the polydispersity of the two amine-functional polyethers, which influences the overall material dampening and network heterogeneity, respectively, by the ratio of the two modifiers. All networks exhibited glassy (pre-T_g, ~0 °C) storage modulus values between 1.7 and 1.9 GPa and rubbery (post-T_g, 105 °C) values ranged between 9.1 and 11.1 MPa. A summary of various thermomechanical properties is given in Table 5.2.

Table 5.2

Modified Matrices Bulk Polymer Thermomechanical Properties

Formulation	**Tan δ Peak Max (°C)**	**Tan δ FWHH (°C)**	**E″ Peak Max (°C)**	**E′ Glassy (-50 °C, GPa)**	**E′ Rubbery (125 °C, MPa)**
THF10-ED90	54.47	39.35	33.63	3.507	15.83
THF25-ED75	55.80	38.14	34.95	3.424	15.73
THF50-ED50	58.45	36.28	36.47	3.231	14.51
THF75-ED25	60.16	35.36	37.04	3.154	14.28
THF90-ED10	60.35	35.82	37.42	3.212	14.20

The molecular weight between crosslinks (M_c) was determined via the theory of rubbery elasticity as described in Chapter IV using an average density value of 1.045 g/cm^3 and a relatively small range of M_c values was determined (average of 1,075 ± 115 g/mol), suggesting that the average crosslink densities of the networks were approximately the same. These trends, taken in concert, signify that altering the ratio of the two polyether modifiers successfully resulted in matrices with variable solubility characteristics while maintaining a similar network connectivity between all systems.

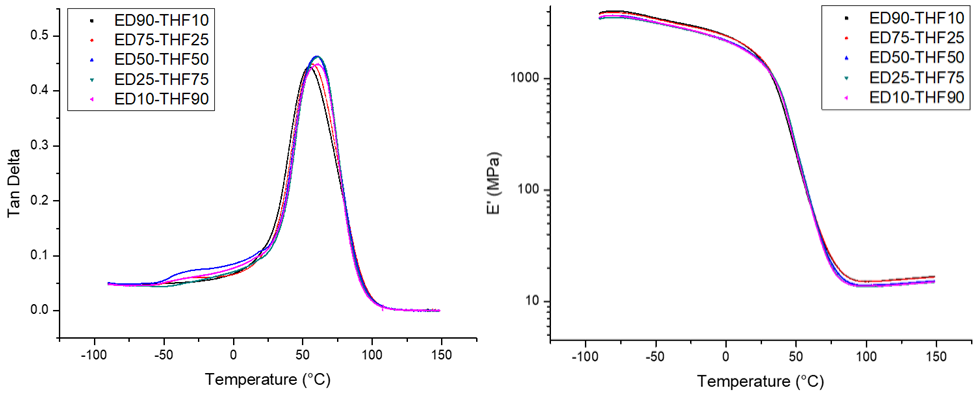

Figure 5.8 DMA thermograph overlays of the modified epoxy-polyamidoamine networks: Tan Delta (left) and Storage Modulus (right).

Additionally, cured bar samples (10 x 5 x 1 mm) of select networks (THF10-ED90, THF50-ED50, and THF90-ED10) were immersed in DI H_2O and subjected to DMA testing after 1, 5, 25, and 60 days. DMA was performed twice on the samples immersed for 60 days, with the bar dimensions being re-measured and the samples re-installed prior to the second temperature ramp. Figure 5.9 exhibits the shift in glass transition properties as given by the tan δ signal across the various immersion times. Each of the networks exhibits a similar trend in initial reduction of T_g by approximately 10 °C after 1 day immersion in water accompanied by a slight increase in tan δ peak maximum value, indicating a

dampening of the transition associated with hydroplasticization. Each subsequent time point plot reveals a decrease in tan δ signal peak maximum and slight increase in T_g which is suggestive of increasing polymer network conversion. After 60 days of immersion in DI H_2O the glass transition temperatures have increased to 1-2 °C above the original/dry values, demonstrating a complex sequence of events associated with interactions between the polymer and water. Immediate response to water ingress is the depression in thermomechanical properties but as mobility increases the residual conversion of unreacted epoxy and amine groups takes place, leading to higher T_g values.[29-30]

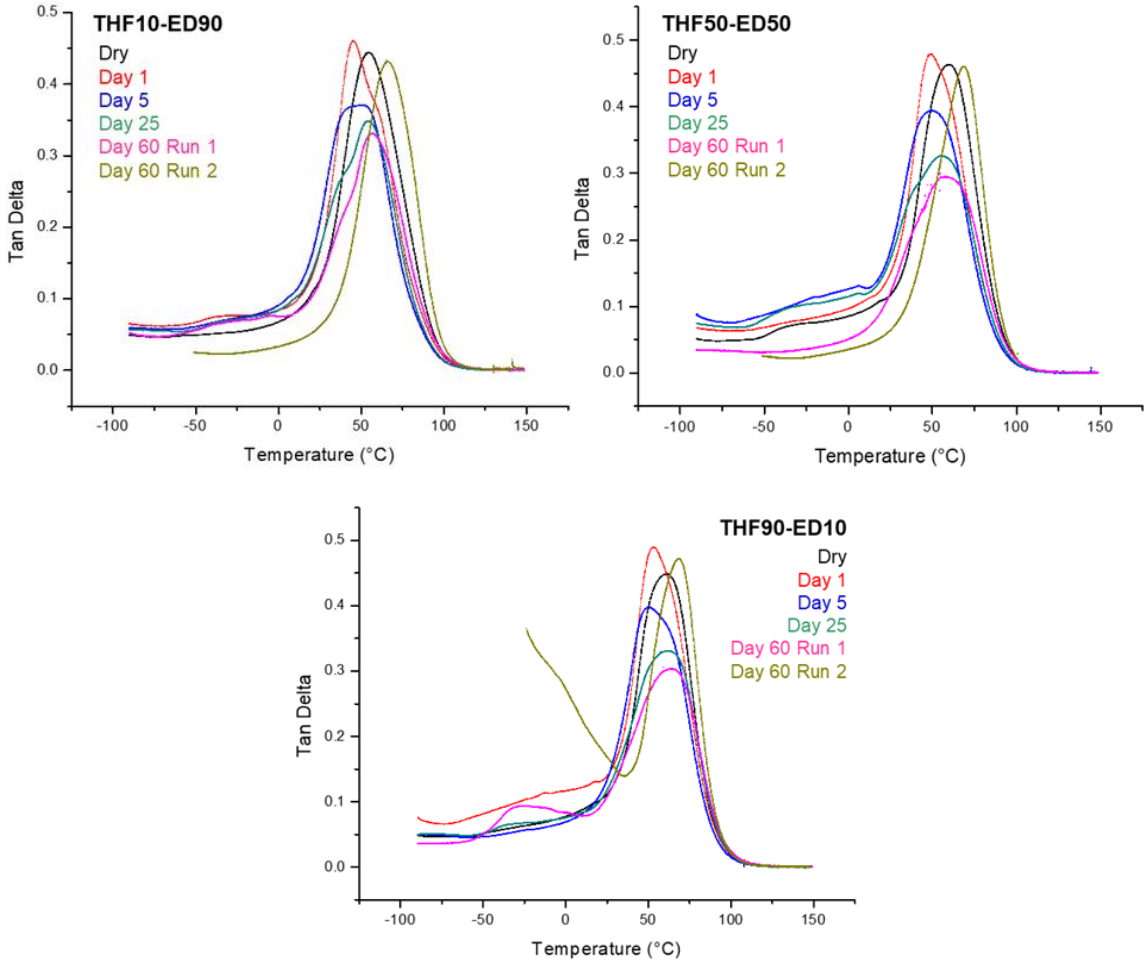

Figure 5.9 DMA (tan δ) thermograph overlays of the modified epoxy-polyamidoamine networks following immersion in DI H_2O for various times.

The evolution of the tan δ peak shape at the glass transition throughout the immersion process also exhibits similar trends between the formulations with high temperature shoulders appearing after 1 day of exposure and low temperature shoulders at 25 and 60 days. The presence of these features indicates a non-uniform distribution of more or less plasticized regions early in the sorption process then higher or lower crosslinked regions following residual conversion of unreacted groups. After completing a DMA test on each sample immersed in DI H_2O for 60 days the samples were removed, the dimensions measured, and then re-installed into the DMA clamp. These samples were then subjected to a second DMA temperature ramp to determine what effect the removal of water (due to heating during the original test) would have on the polymer network state following saturation with water. As exhibited in Figure 5.10 the tan δ peak widths and maximum values return to within 1-3 °C of the original quantities although the T_gs reveal a slight increase, most likely due to a combination of enhanced cure attributed to residual non-reacted group mobility imparted by hydroplasticization and additional exposure to higher temperatures during testing. However, the samples exhibited signs of brittle failure during the second DMA cycle which indicates some degree of hydrolysis took place concurrently as an effect of simultaneous presence of exposure to higher temperatures and water content. These findings indicate that the matrices undergo considerable thermomechanical shifts following sorption of moisture although the extent to which these properties alter is not necessarily dependent upon total water present within the matrix.

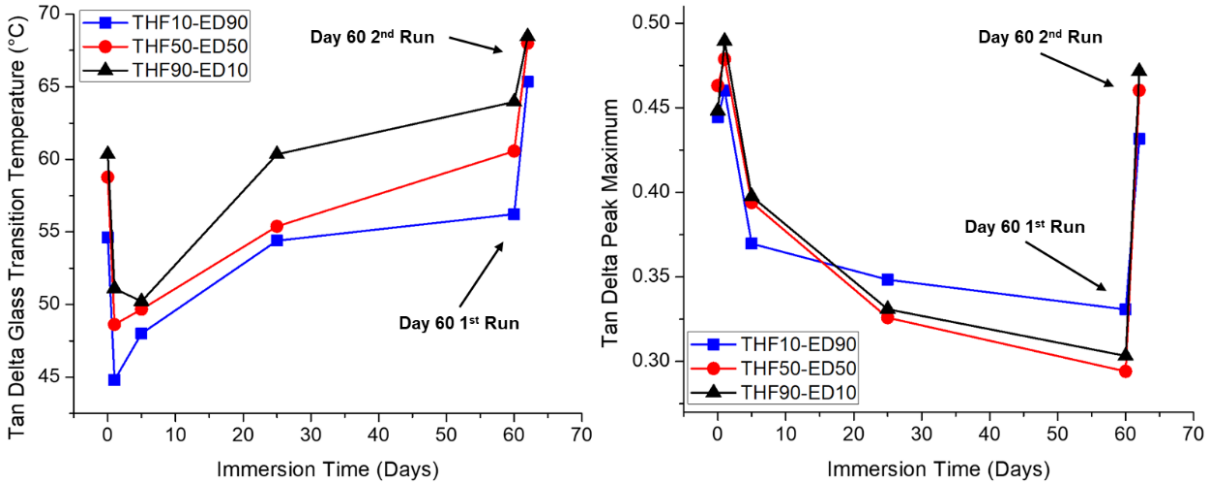

Figure 5.10 DMA (tan δ) peak value trends for the modified matrices as a function of immersion time.

5.3.2 Coatings Characterization

All the coatings exhibited very similar properties as measured by the different test methods and the results suggested favorable primer performance: high flexibility (all coatings passed mandrel bend test), good mechanical resilience (> 120 in-lb. impact resistance), excellent crosshatch adhesion (5B), and chemical resistance (200+ MEK double rubs). Koenig hardness readings (Figure 12) of the different coatings were also similar (between 20-40 seconds); in general, the addition of the ED900 and THF100 resulted in slightly lower hardness as compared to the unmodified system (E825-2445). Only the gloss measurements revealed any variance between the systems, which is potentially due to the tendency for PEO units to aggregate at the interfacial surface and would result in some mild phase separation that influenced the light scattering. Although care was taken to mechanically agitate the reactant mixture until moderate viscosities were obtained, which would assist in network growth under homogeneous mixture conditions,

it is still possible that some degree of mobility differentiation at later stages of cure could have resulted in higher concentrations of ED900-containing groups near the interface. Other coating properties suggested that, in general, the different formulations yielded uniform networks and primers.

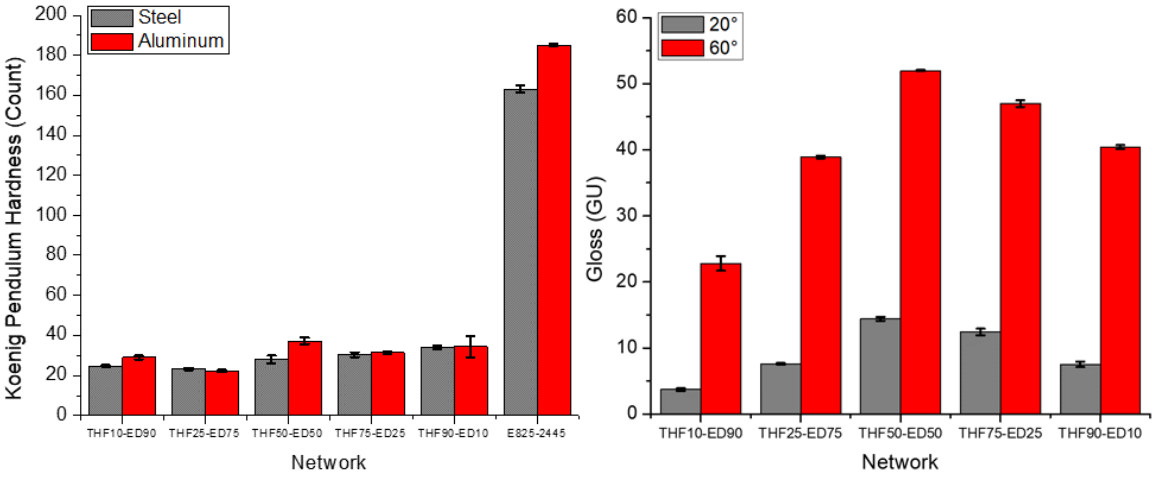

Figure 5.11 Comparison of fully formulated chromate-containing coatings properties: König pendulum hardness values of all modified network coatings on S-36 steel and 2024T3 aluminum panels (left) and 20°/60° gloss measurements of coatings on steel.

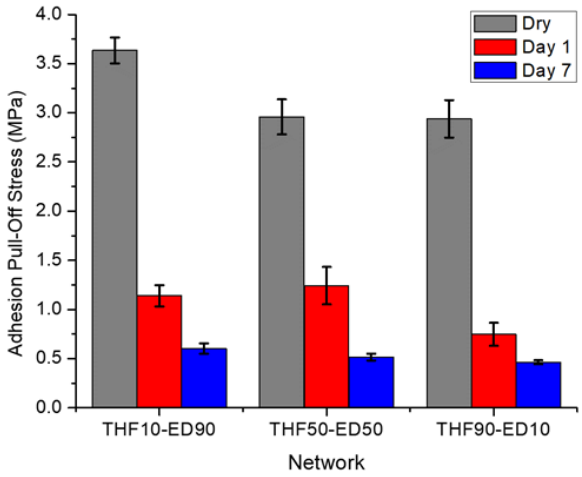

Figure 5.12 Comparison of fully formulated chromate-containing coatings pull-off stress of select networks (THF10-ED90, THF50-ED50, and THF90-10) on steel panels before and after immersion in DI H_2O.

Of significant importance is the extent to which the sorption of water affects coating adhesion during the service lifetime. Given the necessity for the presence of moisture within the primer to allow for inhibitor dissolution and leaching, a careful balance must be achieved to avoid coating delamination via displacement of polymer-substrate interactions at the interface by water molecules. For that reason the shifts in adhesion between primer and metal following exposure to DI H_2O were evaluated according to ASTM D4541 pull-off testing. As seen in Figure 5.12 the coatings exhibit very little variation between formulations following 1 and 7 days immersion. In the dry state the most hydrophilic primer matrix (THF10-ED90) reveals a slightly higher average pull-off stress, likely due to a higher concentration of ether functional groups available for secondary interactions with the metal hydroxide layer, but at later stages of exposure almost no variance is found between the formulations at the respective time points, despite the different levels of moisture ingress each matrix is found to experience. These results indicate that among the range of modified matrices analyzed here the difference in absorbed moisture has minimal effect on adhesion properties, at least within the time frame of exposure seen here.

Coated panels tested in a Q-FOG CCT-600 neutral salt spray (NSS) cabinet as per ASTM B117 (35 °C and 20 psi) for at least 440 hours were scanned as such after patting them dry with paper towels. The corroded area was expressed as a percent of the total exposed area determined for each series by using the trace feature of imaging software to measure a set distance from the center of the scribe to the ends of the scribes and connecting the corner points. Images of the coated steel panels following testing and the corresponding corrosion area percentages are shown in Figure 5.13 along with a comparison of steel and

aluminum panel scribe corrosion areas at the conclusion of testing (Figure 5.14). A general trend was noted in that increasing matrix hydrophilicity (as quantified via the hydrogen bonding Hansen solubility component and by the amount of water each polymer sample absorbed) correlated with lower values of average corrosion product area, although this variability was very slight in the case of the non-chromate inhibitor. Coating systems containing the chromate inhibitor exhibited greater differences in corrosion area between the various networks with approximately 58% difference between the least and most hydrophilic formulations on steel and 35% difference on aluminum substrate. The CRI inhibited systems only revealed a 13% difference in measured scribe corrosion area on steel panels but those on aluminum substrates revealed a distinct pattern, as illustrated in Figure 5.15. CRI-containing aluminum coated panels did not exhibit any formation of visible corrosion products within the scribe but rather developed coating blisters within the defect area which first appeared at around 100 hours with the most hydrophilic networks. It was somewhat expected that the most hydrophilic matrices would absorb and retain sufficient water for hydroplasticization and loss of modulus to surpass the wet state osmotic pressure/adhesion ratio threshold to blister formation, leading to localized delamination and eventual ineffectiveness, while the most hydrophobic panels would be unable to transfer enough inhibitor to the substrate to be effective. The CRI primer containing equal amounts of the hydrophilic and hydrophobic polyethers appeared to offer a sufficient balance between water transport to facilitate inhibitor release/mobility and delivery to better passivate corrosion without resulting in excessive osmotic pressure development that would ultimately lead to delamination.

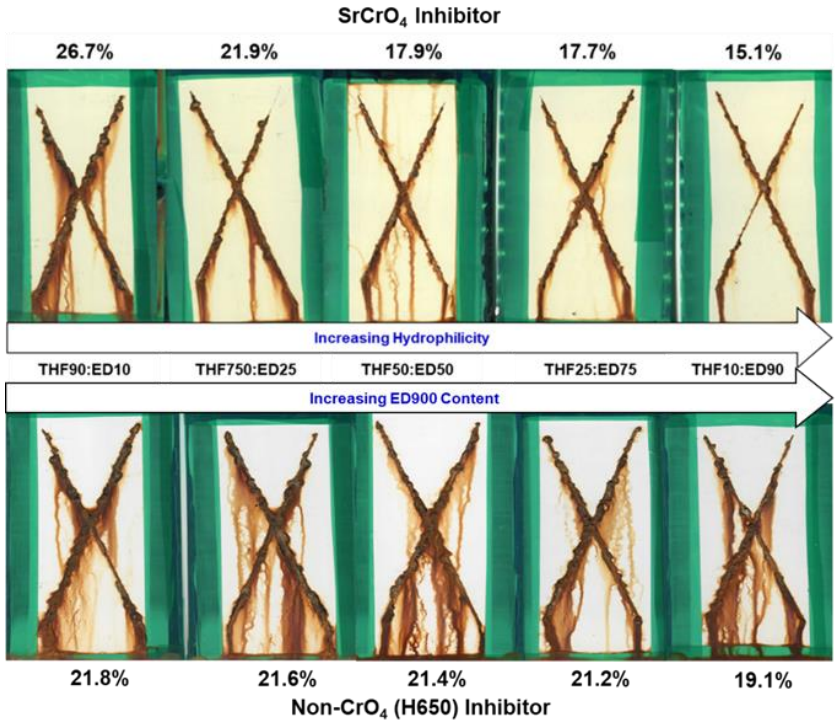

Figure 5.13 Comparison of relative scribe corrosion areas of S-36 steel panels coated with chromate (top) or CRI (H650, bottom) inhibited primers following exposure to ASTM B117 for 440 hours.

Numbers correspond to the relative size of corrosion product growth.

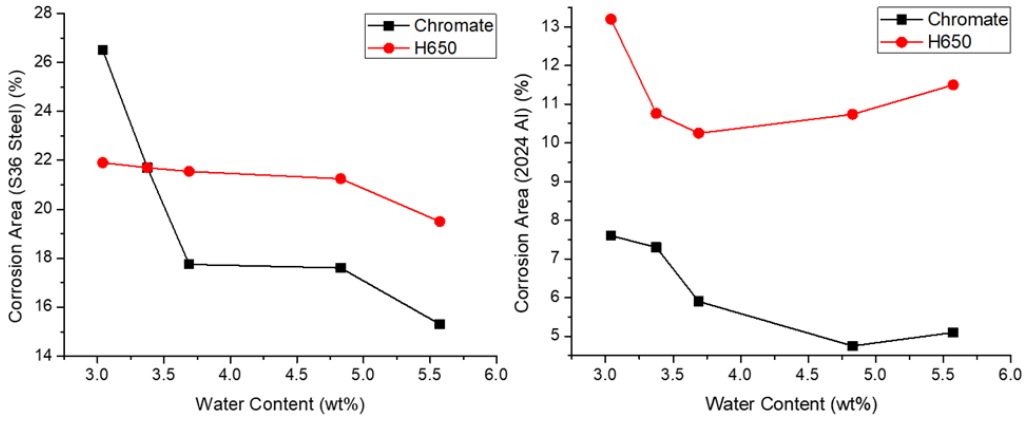

Figure 5.14 Comparison of scribe corrosion areas of S-36 steel (left) and 2024T3 aluminum (right) coated panels following exposure to ASTM B117 for 440 hours relative to the quantity of water absorbed by the respective polymer networks.

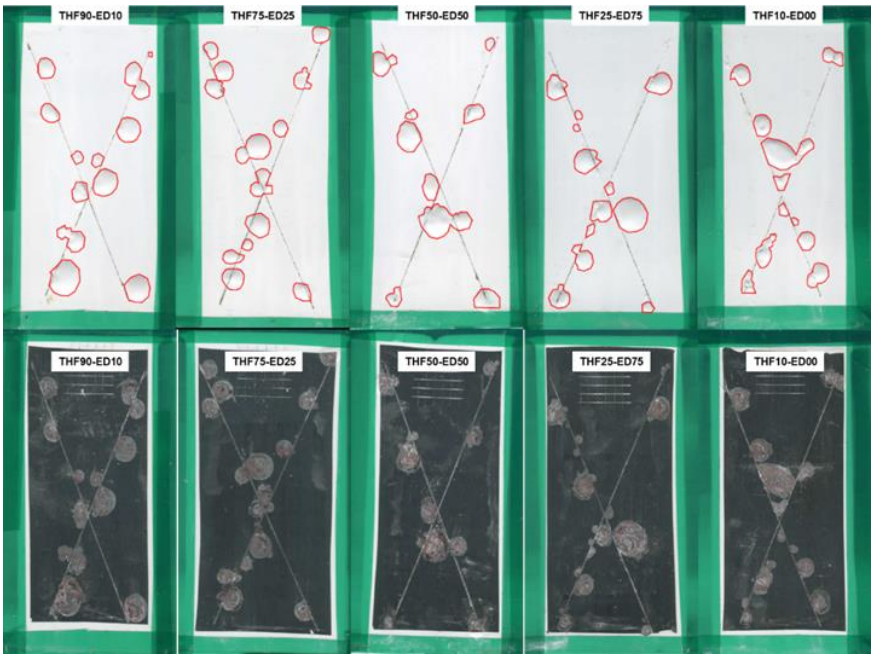

Figure 5.15 Comparison of modified matrix coating formulations containing the CRI H650 on 2024T3 aluminum panels following exposure to ASTM B117 for 440 hours.

Panels with intact coating (top row) and following coating removal to reveal corrosion pitting at the sites of blisters (bottom row). Coating blisters are outlined in red.

5.3.3 Comparison of Modified Matrix Primers within a Multi-Layer Coating

Until researchers are able to mitigate the dissimilar results found in natural outdoor/in-service and laboratory/accelerated corrosion testing it is vital to understand how coatings may perform differently in varied conditions.[22] In addition to analysis and characterization of bulk polymer and solvated, substrate-bound, and pigmented single layer films, the impact of a modified primer matrix within a multi-layer or stack-up coating system must be evaluated in both static and cyclical stimuli environments. As many modern protective coatings consist of two to six individual layers, each serving a distinct purpose (adhesion to substrates, adhesion between layers, UV exposure protection, selective gas barrier, etc.), analyses of both individual layers and stack-up or multilayer

systems are necessary. Moreover, natural outdoor exposure testing of coated panels can yield insight into top-coated primer corrosion protection that is not found within artificial testing conditions. For these reasons an additional testing protocol consisting of outdoor exposure of multilayer systems was employed for further understanding of the relationship between matrix hydrophilicity and on coating performance in real-world conditions.

Multi-layer coatings consisting of THF10-ED90, THF50-ED50, or THF90-ED10-based primers were applied via drawdown bar film applicator at 6 wet mils on S-36 steel Q-panels then dried and cured according the profiles described previously. The topcoat chosen for this study, Deft® 99GY001, is a two-component fluorinated polyurethane specified for use on aircraft external structures (classified as a MIL-PRF-85285E Type IV Class H topcoat). The base and hardener/catalyst were mixed, applied, and cured according to the manufacturer specifications to result in two-layer coating systems consisting of the modified epoxy-amine matrix primers (chromate-containing) and urethane topcoats with approximately similar thicknesses (60-80 μm each). To some of the panels a scribe through the coating to the steel substrate (65 mm length, 0.35 mm width) was applied using a narrow-nosed rotating burnishing tool on a Vision Express engraver. Top-coated panels were then subjected to either ASTM B117 salt fog cabinet (Q-FOG CCT-600, 35 °C and 20 psi) or outdoor exposure testing (mounted 120° to the southern horizon in Hattiesburg, MS) and occasionally images on a flatbed scanner to define progress of the corrosion within and around the scribe could be determined via image analysis.

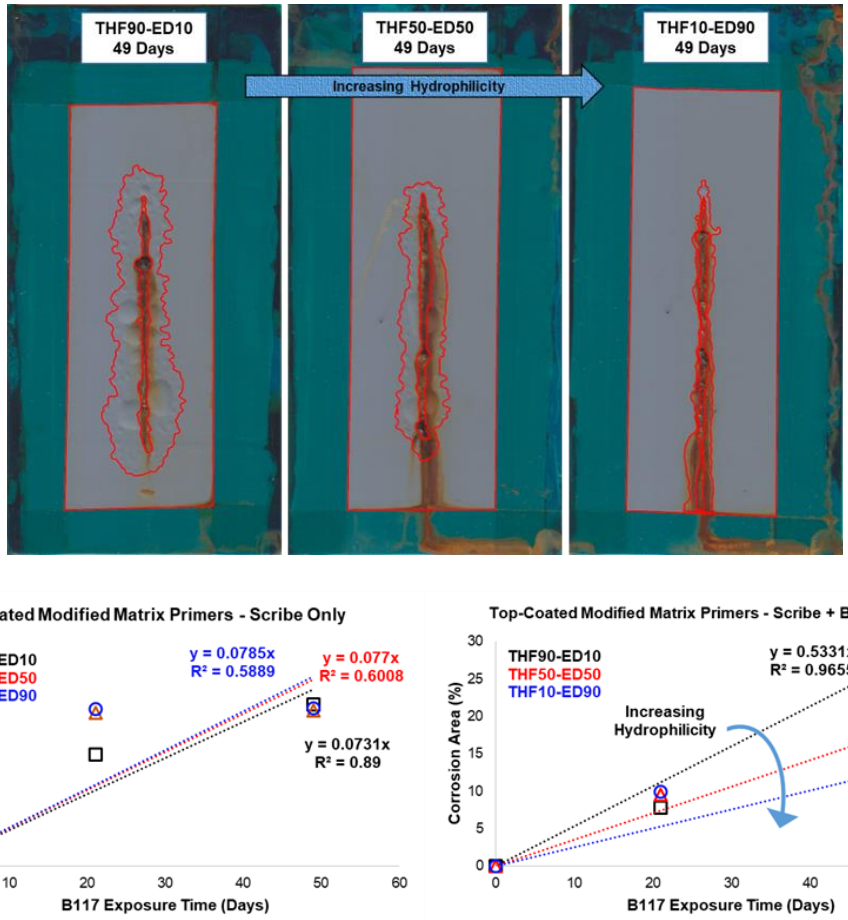

Figure 5.16 Results of ASTM B117 NSS testing of top-coated samples after 7 weeks (top), with relative rates of in-scribe or scribe + blister corrosion product formation are compared (bottom).

The iron oxide-containing scribe areas and blisters are outlined separately (top).

It can be seen in Figure 5.16 that the relative rates of corrosion product and coating blister formation in salt fog cabinet accelerated corrosion testing decreases as primer matrix hydrophilicity increases. The extent to which iron oxide products form within the scribe areas does not vary to a substantial degree between the different formulations but at later stages of exposure the formation of both large and small blisters adjacent to and around the scribe is more apparent within the lower hydrophilicity systems. Blisters form due to the

build-up of osmotic pressure between the coating and substrate as water ingresses and collects at the interface and is commonly associated with the delamination of coating and the development of cathodic sites within the corrosion electrochemical cell region. A lack of these features would suggest that a sufficient quantity of corrosion inhibitor has leached from the coating to prevent to further corrosion at exposed substrate sites. However, at earlier times the opposite trend is observed: at 21 days a slight increase in the corroded scribe area correlates with increasing hydrophilicity which could possibly be explained by the expectation for latency of inhibitor activity between the initial exposure period and later time points. During accelerated testing the higher hydrophilicity coating takes on more moisture and electrolyte contaminants which results in faster initial corrosion rates prior to dissolution and release of inhibitor but results in less relative corroded area at later stages due to a greater extent of substrate passivation by the chromate.

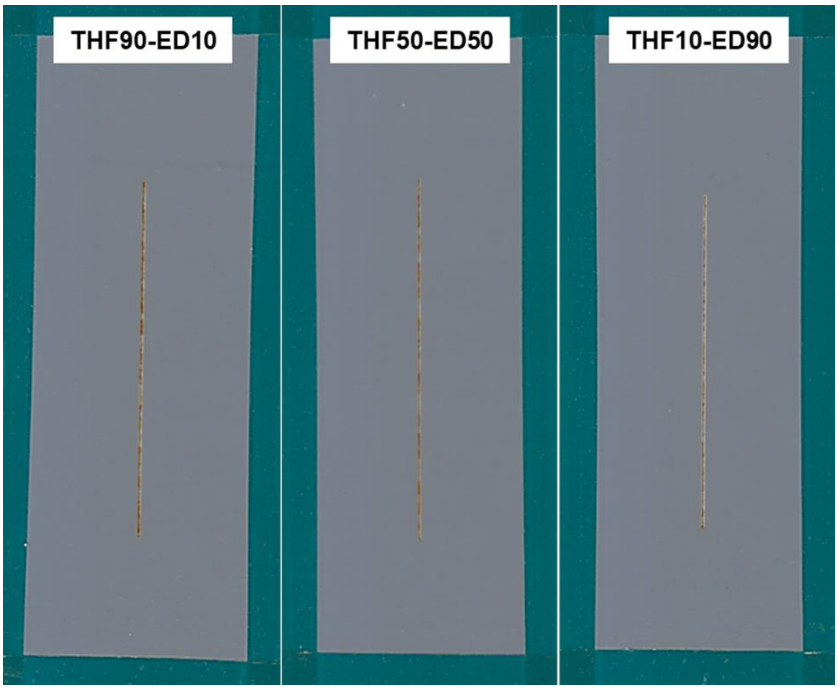

Figure 5.17 Scribed polyurethane top-coated panels containing modified epoxy-amine matrix primers with chromate corrosion inhibitor after 21 days of outdoor exposure.

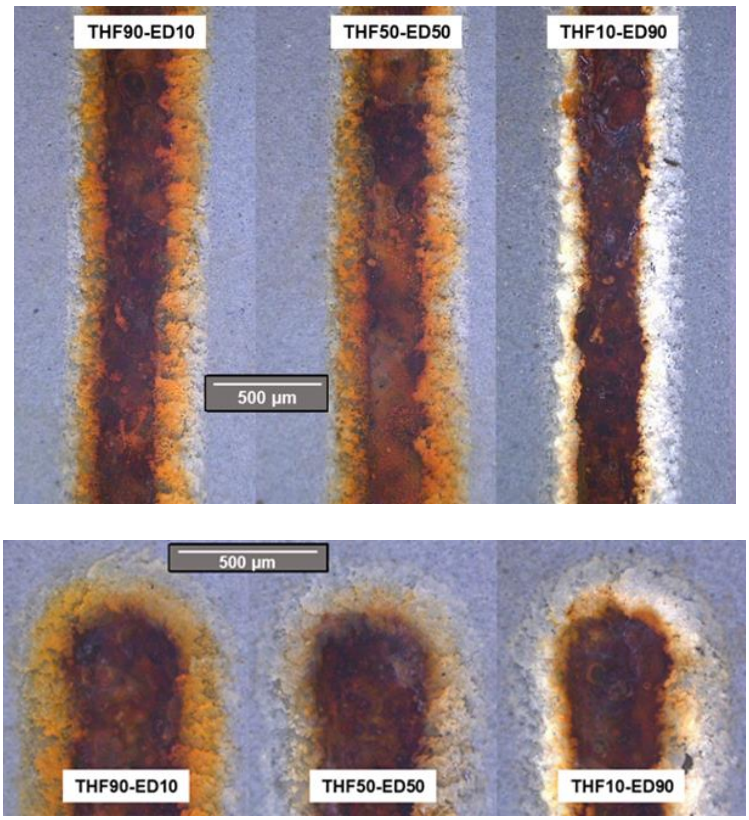

Figure 5.18 Magnified images of scribed top-coated panels containing modified epoxy-amine matrix primers with chromate corrosion inhibitor after 2.5 months of outdoor exposure.

The results of top-coated panel outdoor exposures also yield interesting trends within the relatively short time scale (approximately 2.5 months) and vary from accelerated corrosion testing trends. At 21 days a noticeable decrease in the amount of dark iron oxide corrosion products within the scribe region correlates with THF100 content decreases and ED900 content increases, as seen in Figure 5.17. Unlike what is observed in accelerated corrosion testing, the slower rate of contaminant ingress allows for greater quantities of inhibitor to dissolve and reach the substrate for the most hydrophilic primer such that it results in lower levels of corrosion products throughout the duration of the exposure.

Optical microscopy examination of the scribe regions, shown in Figure 5.18, reveals varying degrees of coating discoloration at the edge with increasing primer matrix hydrophilicity resulting in less brown or red iron oxides/hydrates and more whitening. The composition of whitened areas would most likely be a result of leaching of pigment and residual solvent from the urethane top coat layer, the exact identity and quantity of which is unknown. The corrosion protection performance of the top-coated primers suggests that the presence of a protective outer layer enhances the corrosion prevention capabilities of inhibited primers composed of hydrophilic matrices. In both accelerated and natural exposure conditions the amount of corrosion product formed (both iron oxides/hydrates and coating blister areas) is found to decrease with increasing matrix hydrophilicity when formulated with inhibitor on steel panel substrates. The addition of an outer layer consisting of polymer that presents a lower water solubility to a hydrophilic inhibited primer appears to result in a coating system that allows for expedient release of inhibitor at cut edges and defects without absorbing moisture in excessive amounts.

5.4 Conclusions

A series of formulations were designed to vary the ratio of hydrophobic and hydrophilic components of an epoxy-amine polymer matrix while maintaining a comparable molecular architecture configuration throughout. Differences in network structure and connectivity were minimized through use of amine-functional polyether modifiers of similar molecular weight and length to yield systems with similar mechanical behavior while allowing for variation in water sorption and transport properties. The calculated HSP values as quantified via the Hoftyzer-van Krevelen group contribution method confirmed distinct differences in solubility that correlated the differences in bulk

water uptake profiles. DMA revealed very similar mechanical responses and T_gs in both the dry/unexposed state and during/after immersion in DI H_2O for up to 60 days. Additionally, the fully formulated coatings consisting of these matrices and identical pigment and solvent loadings exhibited very little variance in general coatings properties, including adhesion in both dry and wet conditions. However, it is still possible that differences in matrix microstructure (e.g. free volume properties) that were not detected through these methods could influence inhibitor transport behavior. Krakovsky and co-workers examined epoxy hydrogels crosslinked with polyethers (similar to those studied here) via the use of small angle neutron scattering and dielectric analysis, and determined that in the swollen state the systems were capable of phase separation in the nanoscale (0.1-1 nm) range.[27-32] A shift towards more or less organized microstructure would inherently influence diffusion properties but the mechanism and the extent of such influence is unknown. Additionally, the differences in solubility of strontium chromate (< 0.2 g/100 mL H_2O at 15 °C) and the CRI (< 0.01 g/100 mL H_2O) is likely to result in preferential incorporation of the inhibitor based upon the hydrophobic characteristic of domains, however, was not observed at the macro-level in the coatings. The data does correspond, however, to the differences in corrosion inhibition between the two systems: the lower solubility of the CRI would inevitably result in lower levels of solubilized inhibitor available to the substrate during ASTM B117 evaluation.

Although the polymer matrix acts, in general, as a barrier to the ingress of corrosive contaminants, the presence of water is necessary to allow for concerted transport and delivery of solubilized inhibitor ions to the substrate for efficient corrosion resistance. Therefore, a balance of inhibitor efficacy based on solubility and redox capacity is critical

whereby the eventual corrosion of the substrate can be prevented via delivery of appropriate amount of inhibitor ions without sacrificing barrier efficiency. This study has demonstrated the ability of minor network modifications regarding polymer network hydrophilicity to drastically impact corrosion resistance, and these results correlate with inhibitor solubilization rate differences that affect the ability of inhibitor ions to prevent corrosion at the substrate. That is to say, that modification of matrix compositional features, without substantial structural alteration, impacted transport characteristics to the extent of influencing functional additive efficacy. With increasing matrix hydrophilicity, > 50% difference in corrosion area between networks was quantified in chromated systems on steel panels. However, CRI on aluminum panels exhibited detrimental effects as solubility differences are believed to have allowed for water to accumulate in greater quantities and more localized concentration and increase the osmotic pressure at the substrate interface (beneath intact protective coating), leading to small and yet prevalent blister formation early in the testing. Given the range in solubility and surface energy values found in polymers, pigments, and substrates, it could be expected that customization may be a necessary means of providing optimized corrosion protection for each type and rate of corrosion event and each type of substrate-inhibitor-polymer matrix combination. Given the findings presented here, it is hypothesized that any (top-coated) primer containing an inhibitor with water solubility that approximates that of $SrCrO_4$ (0.2 g/100 mL H_2O) would provide optimal release and hence protection performance with water sorption quantities nearing the upper range observed for epoxy-amine networks (4-7 wt%) without detrimentally impacting other performance variables such as internal stress development and adhesion under various environmental stresses.

5.5 References

1. Mueller, B., *Coating Technology - BASF Handbook*. Mater. Corros. **2003**, 54, 812.
2. Forsgren, A., Corrosion control through organic coatings. *Corrosion* (Houston, TX, U. S.) **2007**, 63, 296.
3. CDC Health Hazards Evaluations. http://www.cdc.gov/niosh/topics/hexchrom/.
4. Sinko, J., Challenges of chromate inhibitor pigments replacement in organic coatings. *Prog. Org. Coat.* **2001**, 42, 267-282.
5. Wicks, Z. W., Jr.; Jones, F. N.; Pappas, S. P., *Organic Coatings: Science and Technology, 2nd Ed*. Federation of Societies for Coatings Technology: **1999**; Vol. 71, p 67-73.
6. van Soestbergen, M.; Baukh, V.; Erich, S. J. F.; Huinink, H. P.; Adan, O. C. G., Release of cerium dibutylphosphate corrosion inhibitors from highly filled epoxy coating systems. *Prog. Org. Coat.* **2014**, 77, 1562-1568.
7. Prosek, T.; Thierry, D., A model for the release of chromate from organic coatings. *Prog. Org. Coat.* **2004**, 49, 209-217.
8. Hughes, A. E.; Trinchi, A.; Chen, F. F.; Yang, Y. S.; Cole, I. S.; Sellaiyan, S.; Carr, J.; Lee, P. D.; Thompson, G. E.; Xiao, T. Q., The application of multiscale quasi 4D CT to the study of SrCrO4 distributions and the development of porous networks in epoxy-based primer coatings. *Prog. Org. Coat.* **2014**, 77, 1946-1956.
9. Frankel, G. S., Buchheit, R. G., Jaworowski, M., G. Swain. *Final Report: Scientific Understanding of Non-Chromated Corrosion Inhibitors Function*. Strategic Environmental Research and Development Program: Alexandria, VA, January **2013**, 2013; pp 256-370.

10. Abdelkader, A. F.; White, J. R., Water absorption in epoxy resins: The effects of the crosslinking agent and curing temperature. *J. Appl. Polym. Sci.* **2005**, 98, 2544-2549.

11. Soles, C. L.; Chang, F. T.; Gidley, D. W.; Yee, A. F., Contributions of the nanovoid structure to the kinetics of moisture transport in epoxy resins. *J. Polym. Sci., Part B: Polym. Phys.* **2000**, 38, 776-791.

12. Soles, C. L.; Yee, A. F., A discussion of the molecular mechanisms of moisture transport in epoxy resins. *J. Polym. Sci., Part B: Polym. Phys.* **2000**, 38, 792-802.

13. Bouvet, G.; Dang, N.; Cohendoz, S.; Feaugas, X.; Mallarino, S.; Touzain, S., Impact of polar groups concentration and free volume on water sorption in model epoxy free films and coatings. *Prog. Org. Coat.* **2016**, 96, 32-41.

14. Hansen, C. M.; Editor, *Hansen Solubility Parameters: A User's Handbook*. CRC Press LLC: **2007**; p 519 pp.

15. van Krevelen, D. W., *Properties of Polymers, 4th ed.*, Elsevier: Amsterdam, **2009**.

16. Mezzenga, R.; Boogh, L.; Manson, J.-A. E., Evaluation of solubility parameters during polymerisation of amine-cured epoxy resins. *J. Polym. Sci., Part B: Polym. Phys.* **2000**, 38, 1883-1892.

17. Shirangi, M. H.; Mueller, W. H.; Michel, B., Effect of nonlinear hygro-thermal and residual stresses on the interfacial fracture in plastic IC packages. IEEE Electron. Compon. Technol. Conf. **2009**, 59th, 232-238.

18. Zhou, J.; Lucas, J. P., Hygrothermal effects of epoxy resin. Part I: the nature of water in epoxy. *Polymer* **1999**, 40, 5505-5512.

19. Lin, Y. C., Investigation of the moisture-desorption characteristics of epoxy resin. *J. Polym. Res.* **2006**, 13, 369-374.

20. Bouvet, G.; Cohendoz, S.; Feaugas, X.; Touzain, S.; Mallarino, S., Microstructural reorganization in model epoxy network during cyclic hygrothermal ageing. *Polymer* **2017**, 122, 1-11.

21. Wong, T. C.; Broutman, L. J., Moisture diffusion in epoxy resins. Part I. Non-fickian sorption processes. *Polym. Eng. Sci.* **1985**, 25, 521-8.

22. Xiao, G. Z.; Shanahan, M. E. R., Water absorption and desorption in an epoxy resin with degradation. *J. Polym. Sci., Part B: Polym. Phys.* **1997**, 35, 2659-2670.

23. Pramanik, M.; Fowler, E. W.; Rawlins, J. W., Another look at epoxy thermosets correlating structure with mechanical properties. *Polym. Eng. Sci.* **2014**, 54, 1990-2004.

24. Wang, H.; Liu, Y.; Zhang, J.; Li, T.; Hu, Z.; Yu, Y., Effect of curing conversion on the water sorption, corrosion resistance and thermo-mechanical properties of epoxy resin. *RSC Adv.* **2015**, 5, 11358-11370.

25. Choi, S.; Janisse, A. P.; Liu, C.; Douglas, E. P., Effect of water addition on the cure kinetics of an epoxy-amine thermoset. *J. Polym. Sci., Part A: Polym. Chem.* **2011**, 49, 4650-4659.

26. Miwa, T.; Takeshita, Y.; Ishii, A.; Sawada, T., Simulation of water absorption and desorption behavior for anti-corrosion coatings in existing and new accelerated corrosion tests. *Prog. Org. Coat.* **2018**, 120, 71-78.

27. Krakovsky, I.; Szekely, N., Small-angle neutron scattering study of nanophase separated epoxy hydrogels. *J. Non-Cryst. Solids* **2010**, 356, 368-373.

28. Krakovsky, I.; Szekely, N. K., SANS and DSC study of water distribution in epoxy-based hydrogels. *Eur. Polym. J.* **2011**, 47, 2177-2188.

29. Krakovsky, I.; Shikata, T.; Hasegawa, R., Epoxy-based hydrogels investigated by high-frequency dielectric relaxation spectroscopy. *J. Phys. Chem. B* **2013**, 117, 14122-14128.

30. Krakovsky, I.; Cayuela, J. C.; Sabater i. Serra, R.; Salmeron-Sanchez, M.; Dodda, J. M., Epoxy networks and thermosensitive hydrogels prepared from α,ω-diamino terminated polyoxypropylene and polyoxyethylene bis(glycidyl ether). *Eur. Polym. J.* **2014**, 55, 144-152.

31. Krakovsky, I.; Martinez-Haya, R.; Ferrer, G. G.; Serra, R. S. i.; Dodda, J. M., Epoxy networks and hydrogels prepared from α,ω-diamino terminated poly(oxypropylene)-b-poly(oxyethylene)-b-poly(oxypropylene) and polyoxypropylene bis(glycidyl ether). *Eur. Polym. J.* **2015**, 62, 19-30.

32. Szekely, N.; Krakovsky, I., Dependence of nanophase separated structure of epoxy hydrogels on swelling conditions investigated by SANS. *Eur. Polym. J.* **2009**, 45, 1385-1390.

CHAPTER VI – QUANTIFYING INHIBITOR LEACHING FROM MODIFIED MATRIX COATINGS USING 2D RAMAN MAPPING

6.1 Introduction

A number of powerful analytical techniques have been implemented in the effort to elucidate the mechanism and effect of chromate dissolution and leaching from organic coatings including X-ray computed tomography[1], serial block face scanning and transmission electron microscopy[2], and inductively coupled plasma mass spectroscopy.[3-4] Raman microscopy has often been coupled with these analyses, although typically as a qualitative means of confirming the presence of corrosion inhibitors and other pigments (or lack thereof).[5-6] In these studies, coatings loaded with particularly high levels of inhibitor pigment (≥ 20 wt%), were immersed in electrolyte solution, and investigated as free films, or otherwise strayed from formulating or testing conditions that reflect real-world circumstances. Although these conditions offer a means for convenient analysis they can potentially yield results that vary from realistic performance characteristics of protective coatings. Additionally, the influence of polymer structure and composition on inhibitor release has not been thoroughly investigated in any of these investigations.

In recent years significant progress has been made in illustrating the underlying mechanisms of inhibitor dissolution and transport from within primers, primarily while utilizing chromate-type compounds in systems for study. Sellaiyan and co-workers employed a combination of PALS, SEM, and $^{51}CrO_4^{2-}$ radiotracer characterizations to evaluate a model inhibited epoxy-polyamide coating following immersion in electrolyte solution.[7] Findings indicated that dissolution of inhibitor initially occurred only at the exposed surface and subsequent ingress of electrolyte allowed for additional release of

neighboring chromate particles. This led to the development of a model wherein it was posited that closely interconnected pigment regions establish a channel or pathway for inhibitor release with only minute amounts of chromate ions diffusing into the bulk polymer matrix, as illustrated in Figure 6.01.[7] Hughes and co-workers further investigated this system using a combination of X-ray computed tomography and serial block face SEM to recreate the pigment microstructures within model primer free film sections before and after electrolyte solution immersion. It was reported that some areas of polymer between pigment clusters exhibited lower material density than the bulk epoxy-polyamide matrix, however, the results nonetheless indicated that voids left behind by dissolved chromate near the exposed surfaces acted as the primary inhibitor ion diffusion conduits.[1-2, 4]

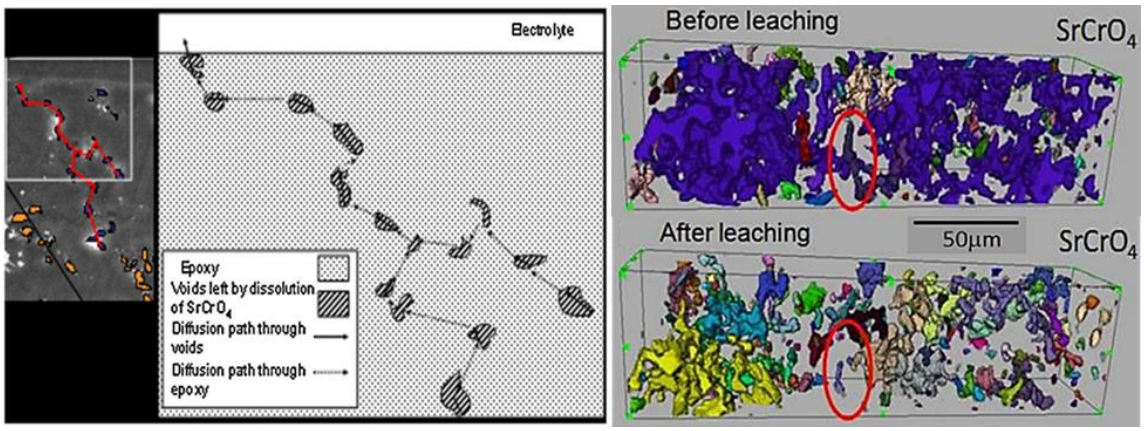

Figure 6.1 Demonstration of proposed transport paths for chromate release from within an inhibited primer and distribution of $SrCrO_4$ pigments within a primer free film before and after electrolyte solution immersion.

Current understanding of chromate leaching from within inhibited primers (left) during electrolyte immersion as depicted by Sellaiyan and co-workers[7] (left), and rendering of inhibitor pigment particles dispersed within a coating matrix before and after immersion as reported by Hughes,et al.[1-2]

Although these studies have afforded substantial insight into the processes involved in inhibitor dissolution and leaching from within polymeric coatings there remain several uncertainties. Among those is the question of whether these trends endure in substrate-bound and top-coated coating systems subjected to more realistic testing environments. To that effect, Raman spectroscopy has proven a valuable tool in similar studies which evaluated the depletion of chromate-based inhibitor from within coatings systems and deposition onto aluminum substrate intermetallic particles subjected to neutral salt spray (NSS) testing, although primarily in a qualitative role.[6, 8] Furthermore, there has been little, if any, consideration for the variability in transport and leaching properties imparted by polymeric components in these studies, and selection of coating matrix materials was of minor importance. This investigation represents an attempt to advance the understanding of processes associated with inhibitor dissolution from within primers including any influence matrix hydrophilicity imparts on the transport process via a quantitative Raman microscopy methodology.

6.2 Experimental

6.2.1 Materials

Select formulations described in Chapter V were implemented in Raman mapping studies, specifically, THF90-ED10, THF50-ED50, and THF10-ED90 modified matrices were chosen as a means of incrementally shifting binder hydrophilicity while holding all other formulation metrics (stoichiometry, PVC, solids content, etc.) and network structure features static. Coatings were prepared as previously described with approximately 80% solids by weight (1:1:1 mixture of *p*-chlorobenzotrifluoride, 2-butanol, and tripropylene glycol n-butyl ether), and pigment loadings at 7% PVC (58.25% CPVC) using a mixture

of TiO_2 (DuPont Ti-Pure™ R-902+, 17.38 wt%) and $SrCrO_4$ (3 wt%). Following the mixing and processing of modified matrices, coatings were applied to 2024T3 aluminum panels with dimensions of 120 x 75 x 0.8 mm (L x W x T) using a drawdown bar applicator at 6 wet mils. These coatings were dried overnight before curing at 60 °C for 1 hour, followed by 120 °C for 2 hours with resulting dry film thicknesses that varied between 70-100 µm. The coated panel edges were covered with a polyimide water-proofing tape and a scalpel surgical blade was used to place a small vertical scribe (≤ 50 µm width, 25 mm length) in the lower third portion of the exposed coating surface as shown in Figure 6.2.

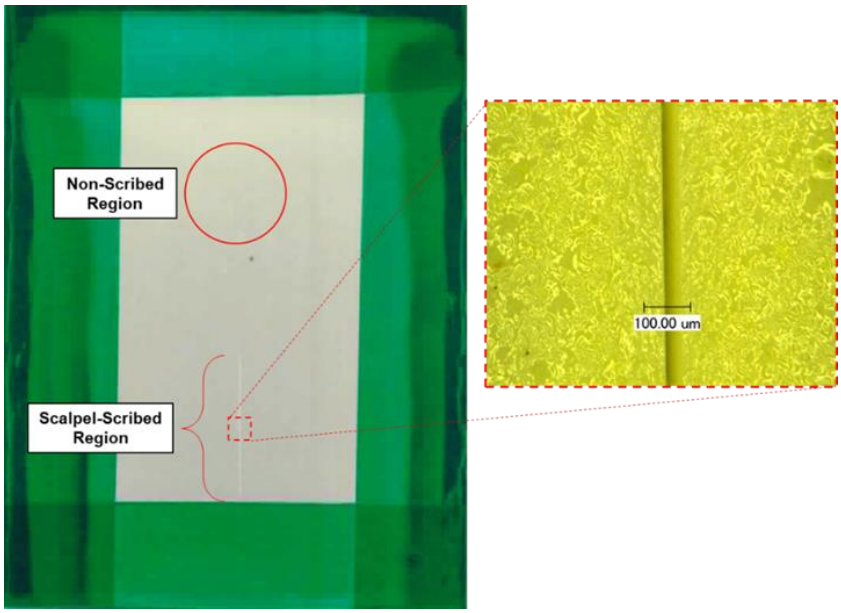

Figure 6.2 Example of coated and scribed 2024T3 aluminum panel displaying regions from which coating cross section samples were taken.

6.2.2 Accelerated Corrosion Testing and Raman Sample Preparation

Coated and scribed panels were subjected to a neutral salt spray (NSS) according to ASTM B117 salt fog cabinet (Q-FOG CCT-600, 35 °C and 20 psi) testing for 0

(dry/non-exposed), 1, 3, or 15 days before removal and drying briefly with paper towels. A table shear was used to cut the panels into small pieces no larger than 25 mm in length or width with multiple cross section samples provided from both the scribed and non-scribed regions of the panels. An embedding resin was applied to the cut edges and the pieces were allowed to dry and solidify in an oven at 35 °C for 48 hours. Fixed cross sections were then polished with 400-1200 grit silicon carbide polishing discs just prior to Raman mapping. Coated panel cross section samples were held upright using a binder clip fitted onto a steel panel which mounted to the Raman microscope automated stage.

6.2.3 Raman Spectroscopy

Raman spectroscopy was carried out using a Thermo Scientific™ DXR Raman Microscope system. Specimens were illuminated through either a 50x/0.75 or 50x/0.5 objective with a 633 nm excitation from a He-Ne laser source. The incident power source ranged from 5-7 mW and resulted in a spot size of 0.8 µm with 3-4 µm spacing intervals between each map point. Single point spectra were collected between 3350-50 cm^{-1} while mapping studies were collected between 3200-100 cm^{-1} and averaged over 64 or 32 scans, respectively, with a spectral wavelength resolution of 1 cm^{-1}. Collection times for mapping studies were approximately 30 seconds per spectrum/point and for all samples an auto-fluorescence correction factor (5th order polynomial) was applied to collected data. Maps of both scribed and non-scribed regions of coatings were collected over an area of approximately 1.0 x 10^4 μm^2, an example of which can be seen in Figure 6.4.

6.3 Results and Discussion

Single point Raman spectra of pure $SrCrO_4$ and TiO_2 pigments were collected and compared with a spectrum of a cured pigmented coating (THF10-ED90) sample, shown in Figure 6.3.

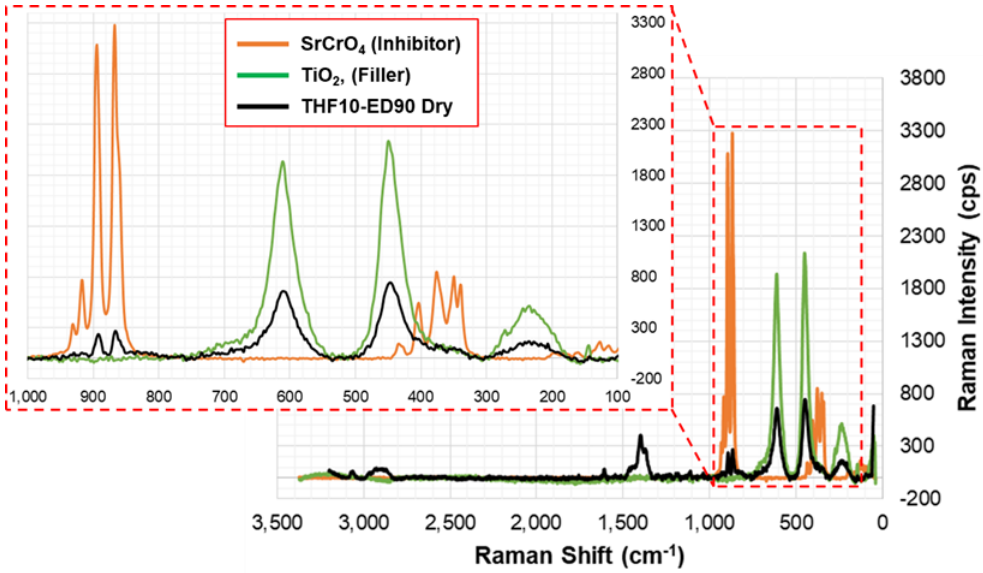

Figure 6.3 Raman spectra overlay of $SrCrO_4$, TiO_2, and a sample pigmented coating demonstrating the presence of pigment component peaks within the polymer.

Strontium chromate exhibits two groupings of peaks centered around 890 and 350 cm^{-1} with two narrow and high intensity bands that also reflect in the coating sample at 893 and 864 cm^{-1} while the titanium dioxide signal includes broad peaks of moderate intensity located at 610, 446, and 238 cm^{-1} which are also found within the dry coating sample. Following the application of an automated baseline correction and background subtraction, spectral 2D maps were constructed either by detailing the intensity of a single wavelength over the cross-sectional area or through a correlation feature whereby the spectrum at each point within the map was compared to the spectrum of pure

pigment. Cross-sectional areas were chosen to include regions of coating that displayed no signs of delamination (an effect of shearing the panel) and were free of coating defects. Scribed coating region cross-sections were framed as to include both coating edges.

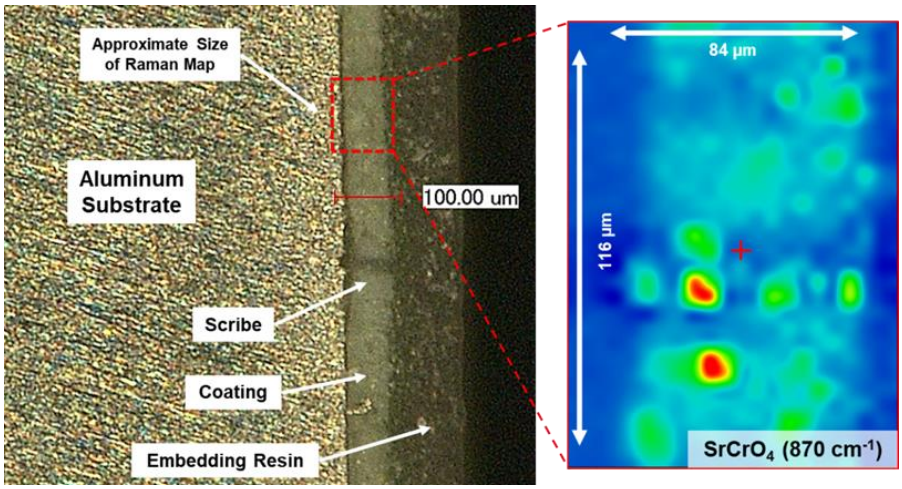

Figure 6.4 Optical microscopy image of aluminum substrate-bound inhibited coating cross-section (left) and example Raman map of the coating cross-section demonstrating the spatial distribution of signal intensity associated with the chromate inhibitor peak (~870 cm^{-1}).

As TiO_2 is insoluble in water the Raman maps detailing the wavelengths specific to this pigment serve as a means of ensuring the fidelity of coating cross section $SrCrO_4$ spectral data; chromate-specific maps of the same area can be normalized to those detailing the TiO2 signal to determine if abnormal shifts in spatial distributions or absences of $SrCrO_4$ signals are due to inhibitor dissolution and leaching or coating mass loss caused by degradation during testing or processing. Examples of Raman map overlays of scribed and non-scribed coating regions are revealed in Figures 6.4-6.6. As anticipated from the formulated pigment loading the $SrCrO_4$ and TiO_2 map overlays of these coating cross sections reveal a significant disparity in signal intensity and hence

concentration in addition to spatial distribution. The chromate inhibitor, loaded to approximately 3 wt% by solids content, exhibits very low signal intensity throughout the analyzed regions with a few high intensity circular areas less than 20 µm in diameter whereas the Raman scattering signal corresponding to titanium dioxide (~17.4 wt% by solids content) reveals a broad, uniform distribution of moderately high intensity throughout the entirety of both scribed and non-scribed dry coating cross sections at all exposure time points and coating formulations.

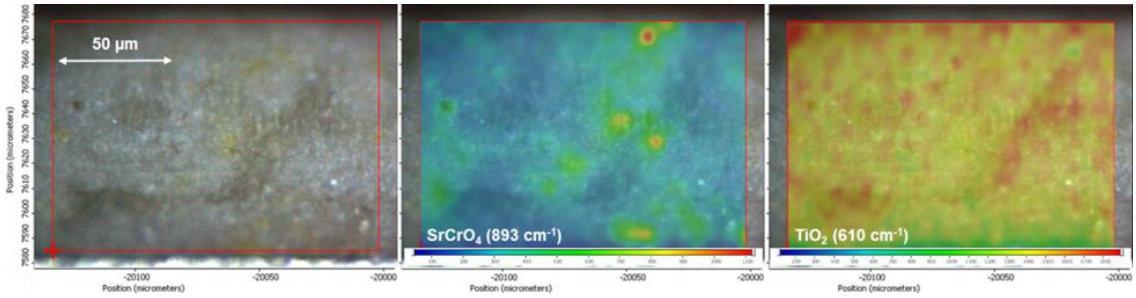

Figure 6.5 Raman microscope image of dry/unexposed substrate-bound coating THF90-ED10 cross section (left) and overlaid Raman maps of the same area correlating with strontium chromate (middle) and titanium oxide (right) content.

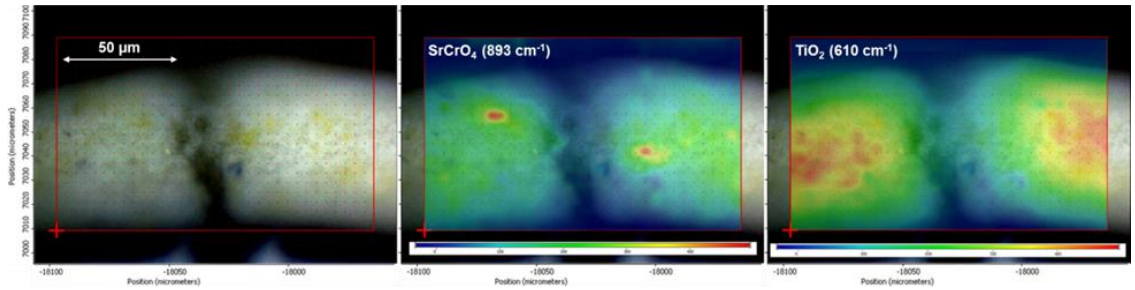

Figure 6.6 Raman microscope image of the scribed area of dry/unexposed coating THF10-ED90 cross section (left) and overlaid Raman maps of the same area correlating with strontium chromate (middle) and titanium dioxide (right) content.

As seen in Figure 6.7 the overall general trend in chromate pigment feature concentration and distribution is a decrease in number and size from the dry/unexposed state to 15 days of NSS exposure time when comparing non-scribed regions of coating THF50-ED50. This development was also observed in the coatings which included THF90-ED10 or THF10-ED90 modified matrices. Throughout the exposure no definitive anisotropic dissolution profiles appear to develop within the undisturbed coating regions; although fewer and smaller features or less intense signals are found, the distribution of remaining pigment bodies within the cross section does not reveal any distinguishing spatial patterns. Given the permeable nature of epoxy networks towards moisture it could be estimated that water penetrates through the bare primer to the aluminum substrate well before the 15 day time point. Nevertheless, a discernable outline of an inhibitor dissolution front is not found to manifest in any specific dimension.

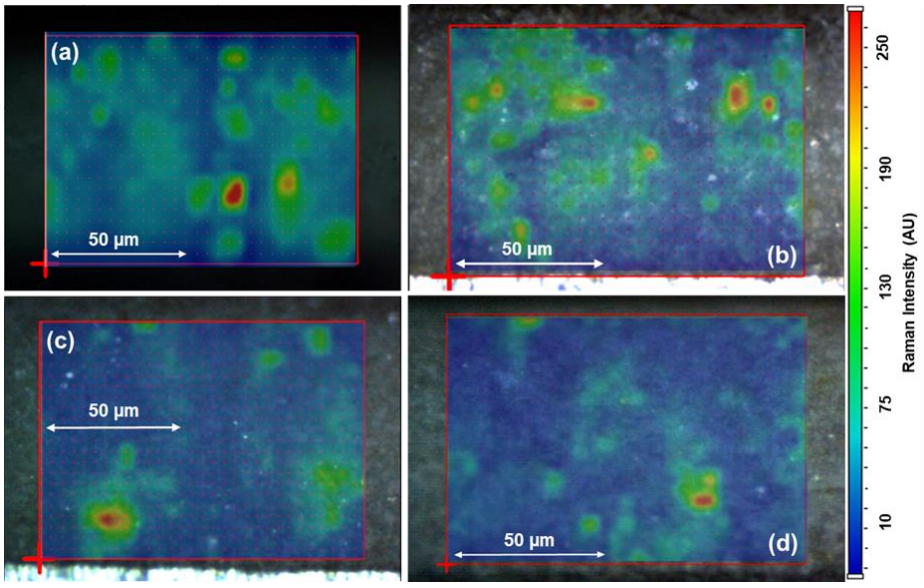

Figure 6.7 Raman microscope images and overlaid Raman maps of THF50-ED50 coatings illustrating the spatial distribution of $SrCrO_4$ within non-scribed cross section regions following (a) 0, (b) 1, (c) 3, and (d) 15 days in NSS testing.

Comparison of the Raman maps detailing the cut edges of coatings within the scribed regions reveals a somewhat dissimilar trend. In examining the $SrCrO_4$ map overlays of THF10-ED90 coatings it is apparent the specified wavelength signal intensity recedes away from the cut edge as exposure time increases. Initially the inhibitor is detected within the unexposed coating up to edge of the scribe, as exhibited in Figure 6.8 (coatings are outlined in white). As salt fog exposure time proceeds the distance between the scribed coatings physical margin and the appearance of detected $SrCrO_4$ signal increases, with as much as a 25 µm separation between the interior inhibitor front and primer cut edge after 15 days of NSS testing. Of particular interest is the manner with which the inhibitor pigment signal depletes: dissolution at both the air and substrate interfaces directly adjacent to the cut edge exhibit the first indications of leaching $SrCrO_4$ followed by the interior region nearest the scribe mark, resulting in an elliptical shape of residual chromate content after 15 days of accelerated corrosion testing.

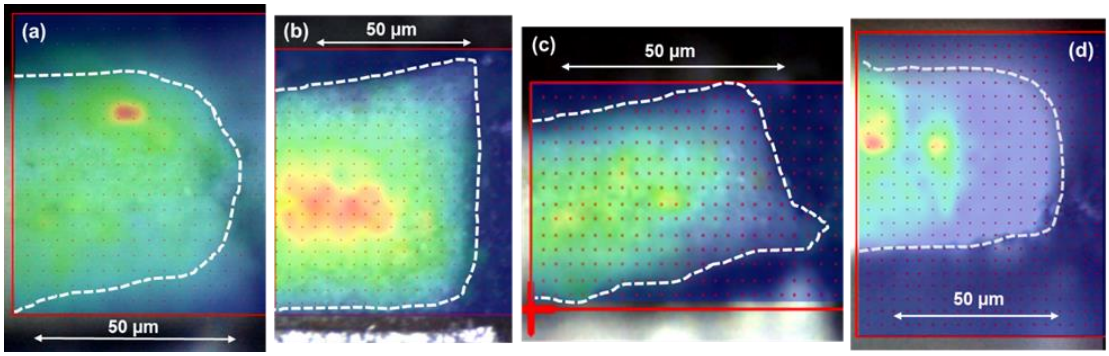

Figure 6.8 Microscope images and overlaid Raman maps of scribed edges of THF10-ED90 cross sections detailing the spatial distribution of $SrCrO_4$ within the coatings after (a) 0, (b) 1, (c) 3, and (d) 15 days in NSS testing.

Each of the scribed coating samples was assessed to measure the rate of leaching as evidenced by the receding strontium chromate signal front from the coating cut edge. As demonstrated in Figure 6.9 both the cut coating boundaries and outer extents of the detected $SrCrO_4$ signal were delineated and the horizontal distance between the two boundaries was calculated with the average distances of both scribe/inhibitor limits compared.

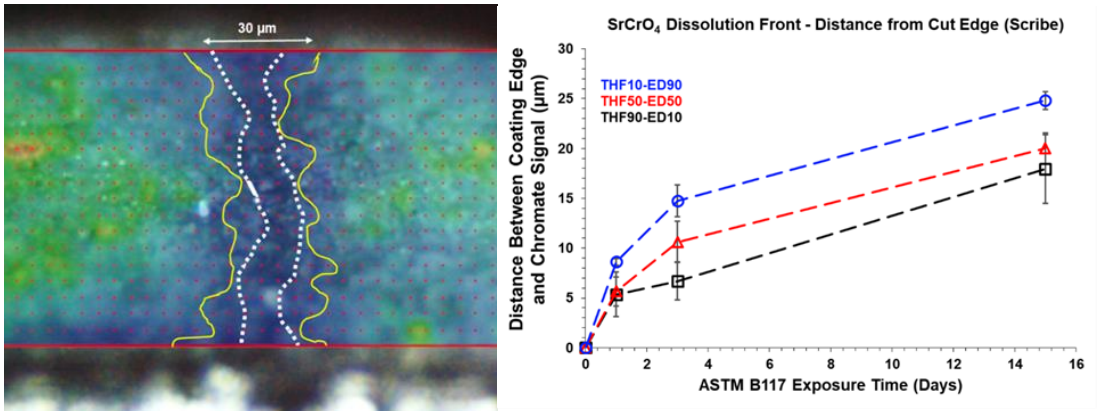

Figure 6.9 Raman mapping analysis illustrating the separation of the coating scribed edge, outlined in white, and the extent of strontium chromate signal, outlined in yellow, of THF90-ED10 following NSS exposure after 1 day (left), and the comparison of dissolution fronts of the various formulations (right).

It is evident from the plot in Figure 6.9 that throughout the duration of the salt fog exposure timeline the coatings did not exhibit a specific point at which cessation of inhibitor leaching occurred. The most dramatic increase in $SrCrO_4$ release, as interpreted from the increase in separation between coating physical boundary and detected inhibitor front, occurred at the initial stages between 0 and 3 days while at later stages the coatings exhibit similar rates of dissolution front procession. At all time points following the start of the NSS exposure the relative distances between coating scribe and $SrCrO_4$ front limits increase with matrix hydrophilicity (THF10-ED90 > THF50-ED50 > THF90-ED10),

indicating that rates of inhibitor dissolution and release are at primarily dependent upon amount of water content available within the coating.

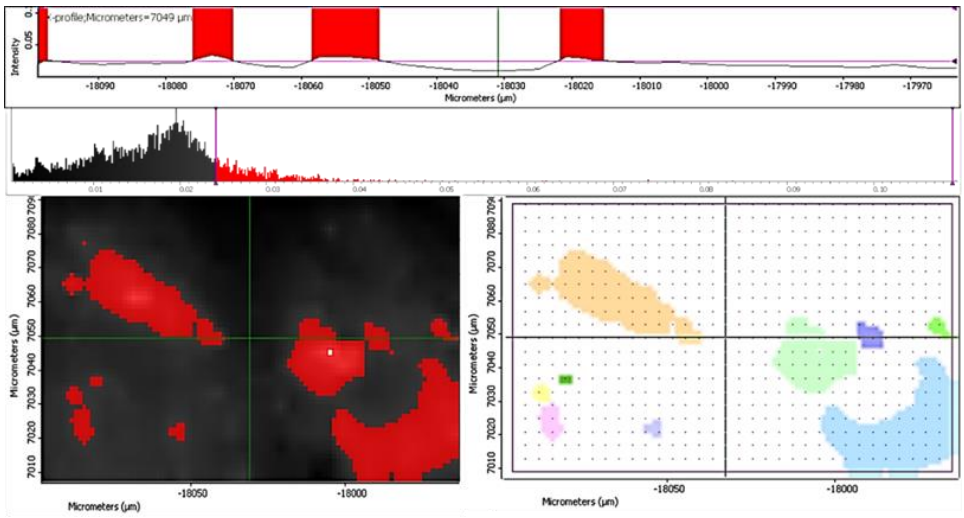

Figure 6.10 Demonstration of Raman mapping image analysis for quantification of inhibitor feature spatial distribution, concentration, and area of THF10-ED90 (1 Day NSS exposure) non-scribed coating cross section.

For a more detailed quantitative examination of the inhibitor dissolution and leaching rates the Thermo Scientific™ Atlµs software for Raman mapping image analysis was used to determine concentrations and spatial distributions of $SrCrO_4$ within both the scribed and non-scribed coating cross sections across all time points of exposure. Figure 6.10 offers an example of the resulting analytics corresponding to pigment feature number, size (area/perimeter), orientation, and histogram distribution of figures correlating to a given $SrCrO_4$ signal intensity threshold. Three signal intensity ranges were extrapolated from each map: those associated with low (blue-green), mid (yellow-orange), or high (red) inhibitor concentration regions. The corresponding pigment feature statistics associated with each range was collected and tabulated while a calibration curve to determine actual pigment concentration was created.

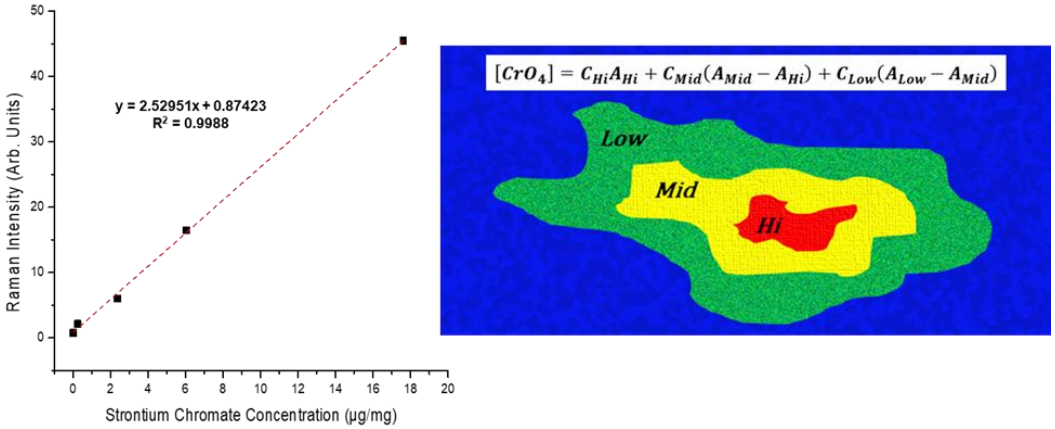

Figure 6.11 Calibration curve used to determine $SrCrO_4$ concentration of pigment regions (left) and demonstration of pigment region allocation used to calculate concentration per pigment feature and per coating area (right).

A strontium chromate concentration calibration curve was prepared by combining various quantities of $SrCrO_4$ pigment with PKHB-80 powder (a DGEBA phenoxy resin-type linear polymer with M_w = 32,000 g/mol), milling until thoroughly incorporated and blended, and obtaining single point spectra of each mixture within the series under the same Raman microscope conditions used for mapping studies. The resulting calibration curve, exhibited in Figure 6.11, was then applied to each extrapolated inhibitor intensity signature map and the overall chromate inhibitor content per coating cross section area was determined according to:

$$[CrO_4]\ per\ Coating\ Area = \frac{C_{Hi}A_{Hi} + C_{Mid}(A_{Mid} - A_{Hi}) + C_{Low}(A_{Low} - A_{Mid})}{A_{TC}}$$

whereby *C* and *A* correspond to concentration and area while the subscripts denote regions of high, medium, or low $SrCrO_4$ signal intensity and total coating cross section area, A_{TC}. The resulting inhibitor quantities are expressed as a function of exposure time as seen in Figure 6.12 wherein both scribed and non-scribed coating formulations are

compared with all values expressed as fractions of the concentrations per coating area ($\mu g \cdot mg^{-1} \cdot \mu m^{-2}$) measured for each respective formulation in the dry/unexposed state (baseline). It is evident upon comparison of the scribed and non-scribed regions that a stark difference in $SrCrO_4$ dissolution and leaching rate trends exists between the two coating regions. After 15 days of salt fog exposure the inhibitor in the non-scribed coating regions exhibits a remainder of approximately 75-95% of the original or baseline strontium chromate signal per coating area while the scribed coatings reveal only 10-50% of their unexposed reference. Additionally, the trends in inhibitor release behaviors of the modified matrices vary between the scribed and intact states. Within the non-scribed coatings a slight increase in the rate and amount of inhibitor loss throughout the salt fog exposure appears as matrix hydrophilicity declines, with THF90-ED10 exhibiting a greater loss in $SrCrO_4$ concentration per coating area (~24%) as compared to the dry state, while THF10-ED90 only reveals a loss of approximately 8% after 15 days of ASTM B117 exposure.

In contrast, the inhibitor dissolution and leaching developments found within the scribed coatings yield a semi-exponential decline that scales with hydrophilicity with THF90-ED10 revealing 50% of the original inhibitor pigment signal per coating area and THF10-ED90 exhibiting only 10% at the end of accelerated corrosion testing. However, the tendency for the greatest loss in $SrCrO_4$ signal to occur during early stages of exposure is found in both coating regions. Throughout the first 72 hours of salt fog testing each inhibited primer displays its greatest rate of decrease in concentration per coating area although the scribed areas demonstrate significantly more extensive leaching

at later stages in NSS exposure whereas the non-scribed coatings appear to near an equilibrium state.

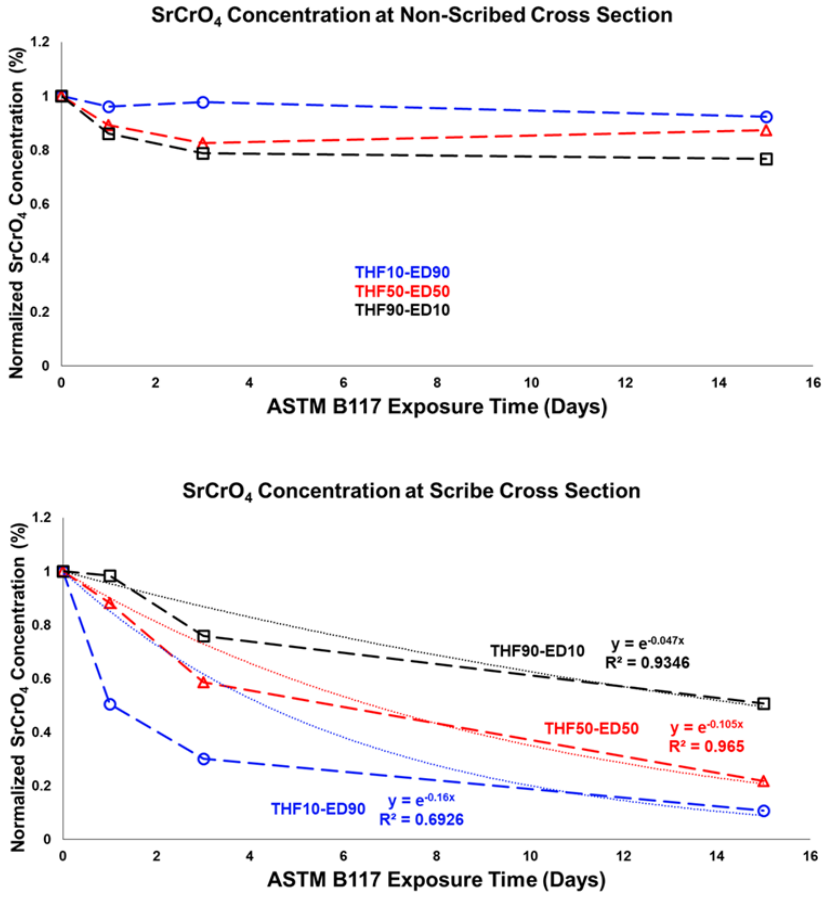

Figure 6.12 Concentrations of chromate inhibitor across un-scribed (top) and scribed (bottom) coating cross sections as a function of accelerated corrosion testing exposure time.

Dotted lines are added as visual guides.

Besides detailing the calculated concentration per coating area, the average pigment feature sizes (area in μm^2) were tabulated, normalized to the unexposed state, and plotted as a function of NSS exposure time, as seen in Figure 6.13. Detected inhibitor particles are found to exhibit a wide distribution of sizes ranging between 10

and 500 μm^2 within each map when including a minimal $SrCrO_4$ Raman scattering signal threshold. The most hydrophilic (THF10-ED90) unperturbed coating cross sections depict a steady increase in the average pigment body area across the entire testing period while the less (THF50-ED50) and least (THF90-ED10) hydrophilic coatings reveal either slight increases or decreases, respectively, as compared to the dry/unexposed conditions. As it is improbable that pigments or inhibitor bodies collectively increase in volume during the leaching process, the shift in detected area is likely due to a combination of traits characteristic of specific matrix water sorption behaviors and pigment features. Following sorption of water, the dissolution and transport of smaller inhibitor pigments and ions into the surrounding environment would inherently result in larger overall size of remaining strontium chromate features. However, if transport proceeded via a mechanism as described by Hughes, Sellaiyan, and others[1,7] whereby leaching occurs through local transport of water through closest neighboring pigment bodies (paths of least resistance) it could be expected that larger inhibitor features would exhibit diminishing size initially given that bigger pigments are more likely to present shorter path lengths between neighboring features than smaller bodies, assuming the same loading and distribution. These competing mechanisms are reflected in the trends of shifting average pigment size: the more hydrophilic matrix allows for faster ingress and a greater quantity of moisture throughout the bulk of the coating which results in dissolution of smaller features first while the least hydrophilic system experiences an initial decrease in average pigment size as larger forms experience preferential dispersion in early stages of exposure followed by dissolution of all other sizes at similar rates once the amount of absorbed water is sufficient to reach all areas within the coating. The

THF50-ED50 system reveals a less intense increase throughout the initial testing period and it could be expected that a significantly more hydrophobic matrix would influence a more significant decrease in average pigment size throughout the accelerated corrosion process.

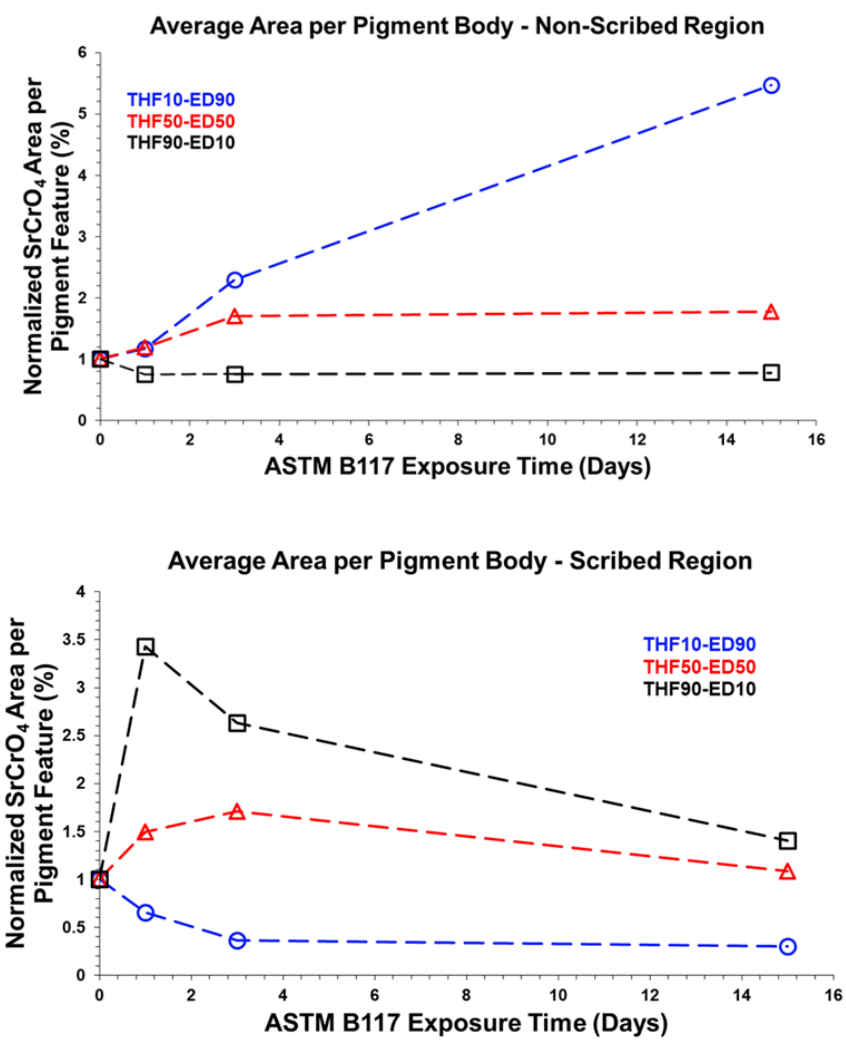

Figure 6.13 Comparison of average pigment feature size between formulations as a function of exposure time within non-scribed (top) and scribed (bottom) coating regions.

Dotted lines are added as visual guides

When considering the average pigment area shifts of scribed primers dissimilar trends are observed as the most hydrophilic coating (THF10-ED90) demonstrates a decrease in average pigment size immediately following introduction to the salt fog testing conditions while the least hydrophilic system exhibits an initial increase during the first day of exposure followed by a abrupt decline. The coating derived from the THF50-ED50 matrix also reveals an increase in average $SrCrO_4$ pigment size prior to gradually decreasing although to lesser magnitudes than what is encountered for THF90-ED10. Additionally, both THF90-ED10 and THF50-ED50-derived primers are found to yield average pigment feature sizes after 15 days of NSS testing that are 27% and 7% larger than what is measured within the unexposed cross sections, respectively. This divergence in pigment feature trends suggests a different means by which dissolution and leaching occurs as compared to the non-scribed coatings. The primary difference in water and ion transport between scribed and non-scribed conditions is the access to the metal substrate surface, coating-substrate interface, and any defects or voids within the coating bulk layer exposed upon formation of the scribe defect. Multiple researchers have determined that the kinetics of ingress and transport of these contaminants at the coating-substrate interface is significantly higher than those measured through the coating itself.[9-12] This coincides with the observation of $SrCrO_4$ depletion of scribed coating regions (Figure 6.8) where it is seen that the extent to which inhibitor has leached from areas of the coating nearest the aluminum substrate meets or exceeds those observed at the coating-air interface. Under these conditions the measured average pigment areas for each formulation suggest that increasing matrix hydrophilicity leads to more water sorption into the bulk polymer via access from interfacial regions, resulting in dissolution

and leaching of pigments of all sizes with equal access to larger features in addition to small particles.

It is likely that coating voids and defects exposed or created by applying the scribe would impact the sorption and diffusion characteristics determined, in part, by polymer solubility. The developments in average pigment feature area seen in Figure 6.13 indicates that within scribe regions increasing hydrophilicity results in faster depletion of larger inhibitor elements while increasing hydrophobicity leads to more rapid disappearance of smaller pigment bodies in early stages. These results are in direct contrast to what is found within non-scribed coating cross sections, indicating that sorption and transport within the coating matrix occurs through a modified process within defect sites. What is not monitored directly through these experiments is the variability in water transport rates at the substrate-coating interface, which is anticipated to hold significant influence over inhibitor access in damaged or scribed coatings. Given the higher diffusion coefficients exhibited by lower hydrophilicity matrices, it could be assumed that further ingress within the interfacial regions at faster rates (although at lower total quantities) allows for dissolution or depletion of smaller inhibitor pigment features along the coating edge prior sorption further into the polymer matrix.

From these results several distinct trends are noted: within scribed regions of polymer, dissolution and depletion of inhibitor along the plane of the coating occurs at faster rates in coatings consisting of matrices that exhibit greater hydrophilicity. By contrast, the intact coatings do not reveal any specific diffusion or leaching pathways despite loss of inhibitor concentration compared to the pristine or non-exposed state. The mechanisms of moisture sorption and subsequent inhibitor leaching from matrices vary

significantly between intact and scribed coating states as observed in both pigment concentration and feature size developments throughout the exposure process. This may be due to direct access to the coating-substrate interface and any matrix defects or voids that develop upon formation of the scribe in addition to pigments embedded within the coating. Central to this work is the evidence of modification to inhibitor leaching rate and mechanism by shifting polymer-water solubility or hydrophilicity through adjustment of network reactant proportion. Based on these findings a general depiction of matrix influence on pigment dissolution emerges: if considering a top-coated inhibited primer exposed to real-world (cyclical) conditions it could be expected that any leaching of $SrCrO_4$ within an intact coating would take place in a manner analogous to that as described by previous studies with dissolution of pigment nearest the surface or interface providing a pathway perpendicular to the plane of the substrate for subsequent ingress of water.32 However, at defect sites water transport within the exposed matrix and along the substrate interface results in mixed modes of inhibitor dissolution with the extent of ingress within the plane of coating, as opposed to along/within the interface, determined by matrix hydrophilicity, as depicted in Figure 6.14.

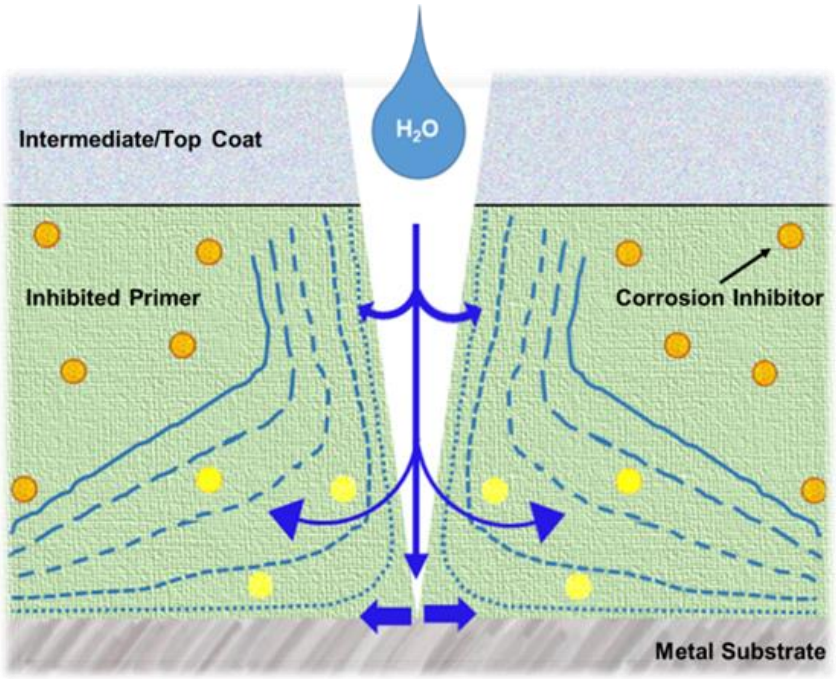

Figure 6.14 Graphic depiction of water sorption through a coating cross section at a defect or cut edge site.

The degree of matrix hydrophilicity within the inhibited (and top-coated) primer determines the extent to which water ingresses and initiates inhibitor dissolution within the coating as compared to along the coating-substrate interface.

6.4 Conclusions

When considering the general mechanism for inhibitor dissolution and leaching from within primer matrices as described by Hughes and co-workers it is necessary to recall that part of the rationale is based on free volume shifts of treated and untreated model primers. It was suggested that minimal diffusion of inhibitor ions would take place through epoxy-polyamide or epoxy-amine matrices given the proximity in size of polymer free volume pores (0.27 – 0.60 nm diameter) and chromate ions (0.32 – 0.46 nm, excluding hydration shell).[1,7] However, the method of PALS utilized by previous researchers necessitated removal of samples from the immersion solution (or other

exposure conditions) and into the instrument apparatus during which time the free volume characteristics could alter substantially as drying occurred. As demonstrated in Chapter III the introduction of moisture results in shifting and reversible measured free volume pore sizes, with some glassy epoxy-amine networks exhibiting a larger $<V_h>$ at high levels of moisture exposure (80-100% RH) than in the dry condition. This could lead to artificially low measured pore sizes when compared to the polymer as it is exposed to liquid water or humid environments, in this case an electrolyte solution. Additionally, the reported $<V_h>$ sizes represent an average value with both larger and smaller pores and voids present within the polymer.

Nevertheless, trends reported here provide support for the previously proposed mechanism, if only in specific conditions. Analysis of non-scribed or intact primers indicated that although no inhibitor dissolution channels were detected via Raman mapping, a substantially slower rate of $SrCrO_4$ leaching was found when compared to scribed counterparts. These primers displayed minor shifts in inhibitor concentration per coating area and/or average area per pigment during initial exposure stages but revealed little change after 3 days of salt fog chamber exposure (except for the most hydrophilic matrix primer, THF10-ED90). This would indicate that moisture is absorbed into the matrix through interconnected free volume pathways during initial stages of salt fog testing but only higher water-soluble networks experience further ingress within the polymer at later times. Scribed coating areas present a dissimilar process whereby access to the coating-substrate interface and exposed voids, defects, or embedded pigment allows for significantly faster depletion of inhibitor along the primer edges and indicates greater extents of moisture ingress into the polymer.

In both instances matrix hydrophilicity directly influences rates of dissolution and the extent to which water diffuses into the matrix. Contrasting modes of shifting pigment concentration per coating area and average pigment body size are observed between the three primers and as all other properties (stoichiometry, pigment loading, T_g, molecular architecture) are unchanged between the formulations the source of these differences can be traced to the polymer-water interaction variations as outlined in Chapter V. One potential implication of this study is that the rates and modes of inhibitor dissolution and leaching are more dependent upon polymer hydrophilicity, as determined by concentration of polar and hydrogen bonding functional groups, than transport kinetics. As discussed previously, the calculated diffusion coefficient (D) decreases overall while water saturation content (M_{sat}) increases spanning from THF10-ED90 (M_{sat} = 4.11 wt%, D = 6.275 x 10^{-10} cm^2/s) to THF90-ED10 (M_{sat} = 2.19 wt%, D = 4.245 x 10^{-9} cm^2/s). Given that the primary factor determining concentrations of inhibitor ions within any solution is pigment water solubility, it would reason that the total amount of absorbed water available within the coating, and not the rates at which a coating absorbs moisture, determines the leaching characteristics. These results should be considered when formulating or designing matrices for use in coatings systems that employ inhibitors of variable water solubility.

6.5 References

1. Hughes, A. E.; Trinchi, A.; Chen, F. F.; Yang, Y. S.; Sellaiyan, S.; Carr, J.; Lee, P. D.; Thompson, G. E.; Xiao, T. Q., Structure and transport in coatings from multiscale computed tomography of coatings - new perspectives for

electrochemical impedance spectroscopy modeling? *Electrochim. Acta* **2016**, 202, 243-252.

2. Hughes, A. E.; Trinchi, A.; Chen, F. F.; Yang, Y. S.; Cole, I. S.; Sellaiyan, S.; Carr, J.; Lee, P. D.; Thompson, G. E.; Xiao, T. Q., The application of multiscale quasi 4D CT to the study of SrCrO4 distributions and the development of porous networks in epoxy-based primer coatings. *Prog. Org. Coat.* **2014**, 77, 1946-1956.
3. Oltra, R.; Peltier, F., Influence of mass transport on the competition between corrosion and passivation by inhibitor release after coating breakdown. *Prog. Org. Coat.* **2016**, 92, 44-53.
4. Hughes, A. E.; Mayo, S.; Yang, Y. S.; Markley, T.; Smith, S. V.; Sellaiyan, S.; Uedono, A.; Hardin, S. G.; Muster, T. H., Using X-ray tomography, PALS and Raman spectroscopy for characterization of inhibitors in epoxy coatings. *Prog. Org. Coat.* **2012**, 74, 726-733.
5. Scholes, F. H.; Furman, S. A.; Hughes, A. E.; Nikpour, T.; Wright, N.; Curtis, P. R.; Macrae, C. M.; Intem, S.; Hill, A. J., Chromate leaching from inhibited primers. Part I. Characterization of leaching. *Prog. Org. Coat.* **2006**, 56, 23-32.
6. Furman, S. A.; Scholes, F. H.; Hughes, A. E.; Jamieson, D. N.; Macrae, C. M.; Glenn, A. M., Corrosion in artificial defects. II. Chromate reactions. *Corros. Sci.* **2006**, 48, 1827-1847.
7. Sellaiyan, S.; Hughes, A. E.; Smith, S. V.; Uedono, A.; Sullivan, J.; Buckman, S., Leaching properties of chromate-containing epoxy films using radiotracers, PALS and SEM. *Prog. Org. Coat.* **2014**, 77, 257-267.

8. Scholes, F. H.; Furman, S. A.; Hughes, A. E.; Markley, T. A., Corrosion in artificial defects. I: Development of corrosion. *Corros. Sci.* **2006**, 48, 1812-1826.

9. Sorensen, P. A.; Dam-Johansen, K.; Weinell, C. E.; Kiil, S., Cathodic delamination: Quantification of ionic transport rates along coating-steel interfaces. *Prog. Org. Coat.* **2010**, 68, 70-78.

10. Bi, H.; Sykes, J., Cathodic delamination of unpigmented and pigmented epoxy coatings from mild steel. *Prog. Org. Coat.* **2016**, 90, 114-125.

11. Pommersheim, J.; Nguyen, T.; Zhang, Z.; Lin, C., Cation diffusion at the polymer coating/metal interface. *J. Adhes. Sci. Technol.* **1995**, 9, 935-51.

12. Wapner, K.; Stratmann, M.; Grundmeier, G., In situ infrared spectroscopic and scanning Kelvin probe measurements of water and ion transport at polymer/metal interfaces. *Electrochim. Acta* **2006**, 51, 3303-3315.

.

CHAPTER VII – SUMMARY

7.1 Overview

The research findings presented within this dissertation are collectively intended to assist in both increasing the understanding of structure-property relationships of epoxy-amine thermosets related to transport phenomena and thermomechanical properties central to substrate-bound organic coatings (primers) while also aiding the formulation process of corrosion inhibitor-containing systems to maximize inhibitor release and thereby prevention of degradation due to corrosion processes. In general the results of these studies support the findings or presumptions of other researchers in that increasing amounts and rates of corrosion inhibitor release and transport resulted in less corrosion product formation, hence more efficient protection afforded by primer coatings. Thermomechanical properties were monitored following modification of network features to determine how these alterations which impact transport phenomena also influence physical traits central to coating performance. It was found that networks of a higher glassy state (higher T_g) endured more substantial shifts in physical state per water sorption percent, but enhancing rates of water sorption and permeation by increasing the matrix hydrophilicity (through both structural and compositional modification) resulted in more extensive corrosion inhibition. A substrate-bound, non-pigmented bare film composed of a low T_g/high crosslink density network that absorbed more than 5 wt% water demonstrated faster rates of magnetite-type (oxygen-starved) corrosion formations. However, apart from that exception, increasing the rates and quantities of moisture transport served to benefit substrate protection. This would suggest that any primer coating containing a corrosion inhibitor (along with other pigments), and in particular an

inhibitor of low water solubility, would benefit from an increase in matrix hydrophilicity, within reason (< 10 wt%).

7.1.1 Summary of Results

With respect to the research tasks and goals established at the beginning of this project, several general gains in understanding are noteworthy:

1) Relatively slight adjustments to epoxy-amine network structural and compositional features via judicious selection of formulation modification (stoichiometry, co-reactant nature and ratio, degree of cure, etc.) can be implemented to the effect each controllable tuning of moisture and inhibitor transport with or without concurrent shifts in physical properties in a controlled manner.
2) Increasing the amount of water sorption and transport (and similarly the rates of sorption albeit to a lesser extent) has a direct correlative relationship to amplified quantities of inhibitor dissolution from within pigmented thermoset substrate-bound films.
3) Within the range of matrix material building blocks, i.e., polymer coatings examined here a general trend emerged in which the systems which exhibited the highest moisture sorption also exhibited the least amount of corrosion product formation during each natural and accelerated weathering when the coatings were comprised of corrosion inhibitor and combined with a topcoat layer.

With regard to the specific findings described here, in Chapter III a number of epoxy-amine matrices which varied in both T_g and total water sorption amount

demonstrated distinct shifts in free volume properties as moisture ingress increased. Glassy thermosets exhibited constant decreases in free volume size from 0-75% RH due to accumulation of water molecules within free volume holes followed by an abrupt increase as large-scale swelling occurred, which was also exhibited by a fully formulated coating free film. The rubbery networks, despite absorbing very different amounts of water, exhibited similar free volume hole size with very little shift with respect to water content due most likely to heightened polymer chain dynamics. Both water vapor and oxygen transmission property trends revealed similar dependencies on moisture content to what was encountered in RH-PALS which signified the dependence of transport characteristics on the fraction of free volume available prior to hydroplasticization-induced swelling. ATR-IR spectroscopic evidence suggested that the proportion of bound and unbound water states within the polymer scaled with matrix hydrophilicity in glassy networks and reaches an equilibrium state that closely matches the rates of sorption as measured via DVS. Of particular interest is that the glassy networks exhibited an abrupt shift in free volume hole size at approximately the same moisture content environments (~75% RH) due to swelling, which may be due to the similar quantities of sorption (2-5 wt%) these networks exhibited.

In Chapter IV the series of matrices all consisting of the same network components and formulated to the extent that distinct M_c and amine ratio levels were achieved and resulted in a range of T_g, water sorption/transmission rates, and amounts. Thermomechanical evaluation of these networks under both humid and dry conditions demonstrated that increasing shifts in physical properties (ΔT_g and swelling-induced strain) resulted from matrices which expressed higher glassy states (higher T_g and

crosslink density), regardless of the quantity of moisture absorbed. Physical aging experiments using these epoxy-amine networks under both dry and wet conditions resulted in the observation of impeded aging processes when in the presence of moisture (immersed in DI H_2O), most likely due to the occupation of free volume by water molecules that would otherwise be necessary for molecular rearrangement. However, extensive hydrogen bonding between matrix functional groups and water could hinder mobility of polymer chains that would otherwise participate in aging-related reconfiguration. ATR-IR analysis of coatings formulated from select matrices (α-I, β-II, and γ-III) revealed similar findings in that a more glassy state expressed more variability in sorption properties with subsequent exposure/drying cycles while the predominant indicator of more water within a coating is a higher proportions of the S_1 (singly h-bonding) and decreasing S_2' (loosely dual h-bonding) water types. This would suggest that a network which allows for greater water ingress interacts less with that water following sorption despite possessing a higher concentration of the hydrophilic groups at the crosslink junctions. As observed in pigment-free coatings, this resulted in more water at the substrate interface and the development of oxygen-starved corrosion product formation. Pigmented versions of these same films exhibited more extensive discoloration due to leaching of inhibitor while the more glassy coatings developed blisters at a significantly faster rate.

Interestingly both bulk polymer samples and pigmented coatings developed from the 50:50 ratio of amine crosslinking agents (β column) exhibited trends that stood out from the other networks, namely, significantly less strain development due to swelling (per wt% of water absorbed) and a differential in the discoloration and blister formation

of coatings (near the scribe instead of the entire exposed surface) following exposure to corrosive conditions. This could potentially be a result of the volumetric ratio of the two reactants meeting a threshold for phase separation which might impart transport and thermomechanical traits not encountered otherwise, however, no other indications of this were detected in any other analytical technique. Finally, a means of producing topologically heterogeneous networks from one of the mixed thermosets (β-II) was developed and evaluated via thermomechanical, moisture transport, and electron microscopy analysis. These were then incorporated into pigmented coatings whereby it was observed that the more inhomogeneous coating released more inhibitor but also allowed for enhanced rates of ion ingress, which would potentially negate any benefit of increased transport rates, unless protected from corrosive contaminants by a topcoat layer.

Chapters V & VI discussed the impact that hydrophilic matrix component ratio has on water transport properties and the resulting effect on inhibitor dissolution and coating performance. Matrices which varied only slightly in composition as the ratio of hydrophilic and hydrophobic modifiers was adjusted exhibited nearly identical thermomechanical properties and only minor differences in H_2O sorption and diffusivity. Coatings formulated from these networks demonstrated similar characteristics (adhesion, hardness, etc.) but following exposure to accelerated weathering conditions a trend of increased hydrophilicity and lowered corrosion product growth was observed, both in chromate-containing systems and in CRI-containing coatings. Both steel and aluminum coated panels revealed this inclination although CRI-containing coatings on 2024T3 substrates showed a minimum at the 50:50 (hydrophilic:hydrophobic) formulation,

suggesting that for some inhibitor-substrate combinations an ideal balance of transport rates and water solubility can be determined. Further development of top-coated coatings systems confirmed this trend in both accelerated and direct weathering experiments signifying that, in general, increasing the hydrophilicity of a coating binder assists in the corrosion protection efficacy of a primer by increasing the rate of dissolution and mobility of inhibitor.

This was also observed in Raman microscopy experiments which evaluated inhibited primer cross sections as a function of exposure time. In more hydrophilic systems both the dissolution and depletion of $SrCrO_4$ occurred at faster rates although it was found that intact (non-scribed) coating regions failed to release inhibitor at appreciable rates due to limited mobility of hydrated ions through the polymer free volume network, regardless of the amount of water present. Based on the findings of Chapter III it could be suggested that increasing the extent of polymer swelling would lead to increases in free volume hole size and thus would lower the barrier to inhibitor mobility following dissolution.

These findings collectively suggest that increasing matrix hydrophilicity and lowering T_g benefits the inhibited primer by allowing for faster and more substantial dissolution and leaching of inhibitor. However, a coating system containing a primer formulated specifically for inhibitor release in such a way would necessitate at least one neighboring coating layer (intermediate or topcoat) that provides a more substantial barrier to moisture in addition to other environmental elements. Ideally an optimized system would consist of an outer coating which exhibits some degree of hydrophobicity and a substrate-bound hydrophilic layer. Although the hydrophilic elements studied here

include both crosslink junction functional groups (tertiary amines and secondary hydroxyls) and backbone segments (polyethylene oxide) no particular distinct between the two was observed in terms of water type populations and impact on inhibitor release and transport. With respect to glass transition temperature, the potential for physical property shift following exposure (including cyclic conditions) to moisture scaled with T_g which, contrary to traditional approaches, would suggest that less glassy state would provide an advantage to an inhibited primer.

7.1.2 Future Work Considerations

When reflecting on the coating aspects typically considered to be responsible for substrate protection efficacy, the dominant traits include (1) barrier and (2) adhesion properties. Within the scope of the research presented here, only specific aspects of barrier properties were investigated, primarily as related to water sorption and transport. Although a complete barrier would prevent ingress of any and all corrosive contaminants, including water, polymers are inherently relatively porous materials and as such it is considered that the organic coating acts primarily as a barrier to ions and oxygen which serve as the limiting factor in corrosion prevention. With regard to the impact of modifying matrix water transport properties on adhesion of substrate-bound films, only limited investigations were carried out here. Chapter V comparisons of networks that varied only in the concentration of hydrophilic polyethylene oxide backbone units revealed almost no impact on the resulting adhesion following immersion in DI H_2O. By contrast, the adhesion trends of Chapter IV coatings (α-I, β-II, and γ-III), which differed in multiple ways, suggests that increasing crosslink density and water sorption in addition to lower T_g results in higher adhesion both before and following exposure to water via immersion. This can be

explained by both the higher concentration of polar functional groups per substrate unit area available for interaction with metal while a less glassy state would allow for faster polymer rearrangement following swelling or application of stress to ensure coating-metal intimacy. In any case the modifications to the networks described here did not appear to alter adhesion to a detrimental extent, although much more research is necessary before any definitive conclusion regarding the impact of polymer matrix hydrophilicity on substrate adhesion can be reached.

In addition to the networks examined here, other polymers should be investigated in a similar manner including the polyurethanes, polyesters, and polyacrylics which constitute a significant portion of coatings binder materials. Most of these systems include a selection of monomers which match those found in epoxy-amine systems and as such should offer comparable potential for solubility, T_g, and topological modification.

Finally, a more extensive range of modification could be explored to determine the extent to which a matrix may be modified to the benefit of an inhibited coating. The systems implemented in this research represent a necessarily narrow range of transport properties for the purpose of precise control. As such the reasonable range of moisture sorption properties can only be estimated at this point.